Universitat Politècnica de València

Departamento de Comunicaciones

PhD Thesis

Design and development of a technological demonstrator for the study of high dynamics GNSS receivers

Carlos Alcaide Guillén

Directora

Dr. Ana Vidal Pantaleoni (Universitat Politècnica de València)

JULIO 2019

Tesis presentada al Departemento de Comunicaciones,
en el cumpliminto parcial de los requisitos para obtener:
Título de Doctor por la Universitat Politècnica de València
Fecha: 26 de julio 2019, Valencia

Agradecimientos

Agradecer a todos los que me han acompañado en este largo pero gratificante camino que supone el doctorado

Resumen

En el marco de esta tesis se van a estudiar, principalmente, los efectos del movimiento de alta dinámica en receptores de Sistemas Globales de Navegación por Satélite (GNSS). El término alta dinámica es un término utilizado para referirse al movimiento de los vehículos en los que van embarcados receptores GNSS, los cuales se mueven lo suficientemente rápido como para causar un gran desplazamiento en frecuencia de la portadora debido al efecto Doppler. Se identificarán los problemas inherentes a este tipo de entornos y se estudiarán y propondrán soluciones. Para poder efectuar el estudio de estos fenómenos, se diseñará un demostrador tecnológico (conjunto de hardware y software para prueba y prototipado de tecnologías) en el que desarrollar el estudio de los casos de interés. Con el fin de trabajar en un entorno repetible, se utilizará un generador de señal GNSS. La señal generada se traslada a un receptor de radiofrecuencia definido por software, *Software Defined Radio* (SDR). Este tipo de receptor únicamente se encarga de digitalizar la señal de entrada y de llevar las muestras digitales a un ordenador, de modo que todo el procesado de señal se implementa en dicho ordenador. Este esquema de trabajo es ideal habida cuenta de su simplicidad y flexibilidad. Dicha flexibilidad conlleva la posibilidad de sintonizar el demostrador para poder estudiar una amplia gama de arquitecturas de receptor GNSS. Una vez se haya ensamblado el demostrador, se comprobará su correcto funcionamiento en escenarios conocidos usando los algoritmos más utilizados a día de hoy en receptores GNSS. Asegurado el correcto funcionamiento, se comparará el rendimiento de algoritmos de referencia con los algoritmos a estudiar y se extraerán conclusiones.

Resum

En aquest treball s'estudiaran, principalment, els efectes del moviment d'alta dinàmica en receptors de Navegació per Satèl.lit GNSS (*Global Navigation Satellite System*). La denominació alta dinámica, s'utilitza per a descriure el moviment dels vehicles dins dels quals hi han receptors GNSS. El moviment d'aquests vehicles és suficientment ràpid com per a causar un gran desplaçament en freqüència de la freqüència portadora. Aquest desplaçament és consqüència de l'efecte Doppler. S'identificaran els problemes inherents d'aquest tipus de entorns GNSS i es propsararàn solucions. Per a estudiar l'efecte de l'alta dinàmica, es dissenyarà un demostrador tecnològic (conjunt de maquinari i software per a proves i prototipat de tecnologies) en que es pot desenvolupar l'estudi dels casos d'interès. Amb l'objectiu d'aconseguir treballar en un entorn repetible s'utilitzarà un generador de senyal GNSS. El senyal es processarà mitjançant un receptor SDR (*Software Defined Radio*). Aquest tipus de receptor s'encarrega del processat que fa un receptor GNSS en un PC. Aquesta filosofia de treball és idónia per la seua flexibilitat i simplicitat. Quan s'haja ensamblat el demostrador, és comprovarà el seu correct funcionament en escenaris de prova utilitzant els algoritmes implementats en receptors GNSS comercials. En aquest moment, el demostrador estarà preparat per a estudiar el casos d'alta dinàmica, que és l'objectiu fonamental d'aquest treball.

Abstract

The study of the effects of the high dynamics on Global Navigation Satellite System (GNSS) receivers, constitutes the main matter of study in this work. The term high dynamics refers to the movement of vehicles that carry GNSS embedded receivers, which move fast enough to generate a large carrier frequency drift caused by the Doppler effect. The problems linked to these environments will be characterized and solutions to counteract possible signal impairments will be discussed. In order to correctly characterize these problems, a technological demonstrator (set of hardware components interacting with software tools enabling fast prototyping) will be designed and constructed. Using this technological demonstrator, the different case studies will be developed. With the aim of achieving experimental repeatability, a GNSS signal generator will be used. The generated GNSS signal is fed to a Software Defined Radio (SDR) GNSS receiver. This receiver type is in charge of digitizing the analog RF signal and carrying the resulting samples to a computer in which signal processing tasks implementing the functions of GNSS receivers, take place. The main advantage linked to the usage of this work scheme is that by changing the software part, different receiver architectures can be implemented in a simple manner. Furthermore, by taking advantage of the flexible architecture it is possible to tune the detector in such a manner that it is possible to implement many different architecture types. Once the technological demonstrator is assembled, tests to assure its correct operation will be conducted by performing comparisons with the behaviour of well-known GNSS receivers in known scenarios. Later on, comparative tests using signals from high dynamics scenarios will take place. Insight and analysis of comparative performance will be given.

Contents

Chapter 1

Introduction

Over the last 40 years, research in Global Navigation Satellite System (GNSS) has drawn increasing attention as new global navigation systems and mass-market services have appeared (take into consideration that Global Positioning System (GPS) and GLONASS (*GLObalnaya Nav-igasionnay Sputnikovaya Sistema*) were developed late in the 70s [1]). GNSS and GLONASS have evolved and a new global navigation satellite system such as Galileo (European Union) is now in service. China foresees to expand its regional Beidou navigation system into the Compass global navigation system by 2021. Moreover, regional GNSS augmentation systems such as Indian Regional Navigation Satellite System (IRNSS), European Geostationary Navigation Overlay Service (EGNOS) or the Japanese Quasi-Zenith Satellite System (QZSS) have been deployed. The fact a large number of space segment satellites and different augmentation systems are now available, implies that a new range of possibilities for GNSS receiver enhancement are a reality now.

A major milestone in the evolution of GNSS regarding user applications happened when the Selective Availability (SA) feature was disabled, forced by the demands of the 911 service [2]. This fact, along with circuit technology miniaturization have helped in the emergence of a wide range of new GNSS applications. Among others, GNSS uses span from precise time stamping for synchronization of commercial transactions [3] to positioning in phones [4], vehicles [5], missile guidance or even in-flight satellite orbit determination [6]. More specifically, according to [7], the main applications of GNSS (taking into consideration the different market segments) are:

1. Location-based services used in many mobile phone apps.

2. GNSS for autonomous driving. Governments are promoting the usage of GNSS for autonomous driving and the main car manufacturers foresee the use of GNSS systems in that area.

3. Aviation market. Planes rely on GNSS to work together with aviation legacy systems such as Distance Measuring Equipment (DME).

4. GNSS solutions for railway networks now offer enhanced safety at a lower cost.

5. Maritime GNSS. GNSS receivers are now the primary means of obtaining positioning information at sea.

6. Agriculture GNSS applications. Agriculture now relies heavily on the usage of drones. This usage accounts for over half of drone market share. Moreover, many tractors are equipped with high-end GNSS receivers.

7. GNSS in surveying and mapping. The usage of GNSS in surveying and mapping has become increasingly available and its uses in surveying and mapping is now generalized.

8. GNSS timing. GNSS time stamping is the backbone of many applications in sectors such as energy, finance among others.

It is clear that GNSS is becoming increasingly important in many of the above-mentioned applications, hence many applications depend on GNSS and the impact of GNSS services have a high economic importance. According to [8], GPS technology will generate circa 122.4 billion dollar benefits per year and will involve more than 5.8 million jobs when market penetration reaches 100 percent. In [8], a survey from the European Commission in which it is estimated that the value of the resources depending on GNSS are in the vicinity of 800 billion euros, is cited.

Nevertheless, despite the wide range of applications in which GNSSs have proved to be useful, there are some situations in which the performance of these systems is seriously hampered. Many works dealing with the situation in which GNSS receiver performance is challenged have been conducted. For example, for severe signal attenuation scenarios (indoor positioning or urban canyons) one can resort to the usage of high-sensitivity GNSS receivers [2,9–12]. However, the implementation of high-sensitivity GNSS receivers for severe signal attenuation scenarios leads to a huge increase in computational cost. This increase in computational cost can make real-time operation unfeasible, hence the need to reduce computational cost appears and research on computational cost reduction must be conducted. Moreover, GNSS signals are very vulnerable to RF interference. A

large amount of different RF interference types affect severely the performance of GNSS receivers (even self interference of strong GNSS signals masking weak GNSS signals [13]), therefore many different approaches to tackle the RF interference scenario problem have been presented too. In [14, 15] the focus is set on detecting and characterizing jamming sources. In other works, subspace projection methods are used to eliminate RF interference [16–19], whereas in others antenna array processing is used to eliminate or alleviate the effect of RF interference [3] or the effect of multipath and RF interference at the same time [20–22]. The ionospheric scintillation scenario (rapid temporal fluctuations in both amplitude and phase of GNSS signals passing through the ionosphere) constitutes another case study that has drawn attention in GNSS research roadmaps [23–27]. Last but not least, cases in which GNSS receivers are embedded in objects travelling at high speed or subject to abrupt accelerations must be considered [28]. These are the GNSS scenarios regarded as high dynamics scenarios. In these cases, the performance of GNSS receivers is greatly affected because the receiver dynamics generate fast GNSS signal variations and whenever the receiver is not appropriately designed, it will be unable to cope with the signal rapid changes. For example, the GNSS signal impinging a Low Earth Orbit (LEO) satellite embedded GNSS receiver is an example of a high dynamics scenario [6, 28–30]. The LEO scenario can be considered as a baseline scenario to settle the basement for the study of more complex scenarios such as space station automated GPS rendezvous [31].

From the above discussion it follows that, in order to guarantee the receiver performance, specific receiver architectures dealing with each specific scenario must be used. Many efforts in these areas have been conducted as such scenarios are challenging and as a result of ongoing GNSS research and modernization, significant improvement in GNSS receiver performance has been achieved. The results of GNSS receiver research and modernization can be translated to the Low Earth Orbit (LEO) GNSS scenario by adapting GNSS receivers for high-sensitivity scenarios to the needs of the LEO scenario.

In this thesis, insight as to why the high dynamics scenario is challenging will be given and algorithms to deal with the high computational cost in a LEO scenario will be tested. Furthermore, the problem to be studied needs to be placed in the frame of a technological demonstrator as this is the only way to implement and test how well the different receivers perform in the cases under study. Accordingly, a GNSS technological demonstrator is implemented and its capabilities will be tested by contrasting Monte-Carlo simulation results and theoretical predictions.

In addition, the receiver performance depends on a number of factors which are inherent to each specific receiver. The fact a GNSS technological demonstrator is constructed implies these factors can be controlled and their effect can be considered when comparing receiver/detector architectures or different receiver efficient implementations.

These factors are [2]:

1. Front-end filtering.
2. Sampling rate.
3. Oscillator stability.
4. Quantization levels.

1.1 Thesis objectives

In this thesis, the focus is set on the development of GNSS receiver algorithms. In order to understand the scope of the work performed, first, a brief description of a GNSS receiver must be provided. According to [5], the block diagram of a GNSS receiver comprises up to eight different blocks. Nevertheless, the last blocks can be merged into a more generic block that includes the so-called navigation processing block. The proposed GNSS receiver block diagram is shown in Fig.1.1.

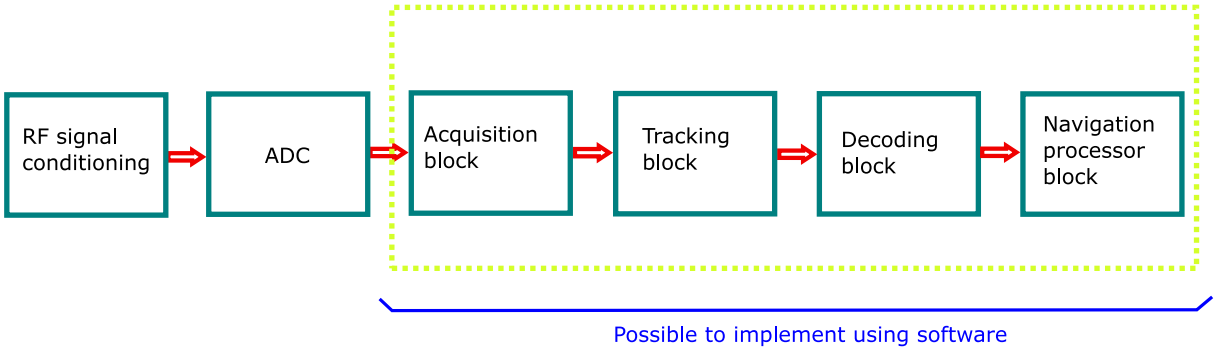

Figure 1.1: GNSS receiver block diagram.

The GNSS signal is received using an antenna. Considering that the signal's received power is well below the noise floor [5, 32], the first task of a GNSS receiver is to perform signal conditioning using a Low Noise Amplifier (LNA) cascaded block to amplify the signal. Afterwards, the signal is digitized using an Analog to Digital Converter (ADC). From this point onwards, the GNSS receiver can be implemented using software resources. Once the signal is digitized, the signal enters the acquisition block. The acquistion process is in charge of the detection of the signals transmitted by the satellites in view (recall that each space segment vehicle emits a different signal). Moreover, the acquistion block also deals with the estimation of the required signal parameters. The tracking block is in charge of updating the parameters estimated in the acquisition process (the signal

parameters change because of the relative movement between the space segment vehicle and the receiver). GNSS is a ranging and a communication system at the same time, hence GNSS satellites transmit useful information that has to be decoded. An ad-hoc block (decoding block) is in charge of the demodulation or decoding process.

Using the ranges (distance between the satellite and the receiver) and the information that has been decoded (navigation data), the last GNSS receiver block which is the navigation processor block is able to calculate the user position.

By the end of 2013, the need to test algorithms for high dynamics scenarios in the "Laboratorio de Guiado y Control" at Instituto Nacional de Técnica Aeroespacial (INTA) (Spain), appeared. Hence, it was decided to implement a SDR based technological demonstrator. However, we must point out that SDR receivers such as GNSS-SDR [33] or commercial platforms such as GMV's SRX10 [34], Deimos' GRANADA [35, 36], Namuru [37, 38], or the Phoenix receiver [39, 40] (based on the Namuru receiver) can also be used for algorithm modelling purposes. However, the technological demonstrator to carry out the study for GNSS algorithms in a high dynamics scenario was necessary at the time being. The lessons learnt in the SDR technological demonstrator construction process are very valuable and are the basis of the knowledge acquired to tackle the GNSS high dynamics problem. This justifies the need to construct a SDR technological demonstrator from scratch.

The most important item in the frame of this work is to study, compare and establish receiver architectures and algorithms for GNSS receivers in high dynamic scenarios. Nevertheless, this cannot be achieved by using commercial GNSS receivers, as they cannot be used for high dynamic platforms because of the restrictions in the Coordinating Committee for Multilateral Export Controls (CoCom). Following the restrictions dictated by the CoCom, GPS receivers disable the tracking capability for devices moving faster than 1900 km/h or devices at an altitude exceeding 18000 m. Furthermore, it is not possible to use commercial GNSS hardware receivers to implement software defined receivers as for the implementation of GNSS software receivers, access to the raw digitized GNSS signal is compulsory. Hence, in order to fulfill the goals of this work, a Software Defined Radio (SDR) [41] based technological demonstrator must be implemented first.

When working with GNSS receivers embedded in objects under high dynamic movement, it is necessary to study algorithms to deal with the special needs arising in such scenarios. In order to deal with the generic GNSS high dynamics problem, the first step in the long-term strategy to be conducted is to concentrate on a specific problem at the beginning of the study. More specifically, in this work, we will focus on alleviating the high computational cost of receivers embedded in LEO satellites. In view of the above-mentioned points we can summarize the main objectives of this work in the following

list:

1. To perform a state-of-the-art study of the different algorithms dealing with the high dynamics scenario.
2. To construct a technological demonstrator for a high dynamics scenario. This is accomplished by simulating the signals for a specific scenario. Then, the RF signal is digitized and the samples are processed using baseline GNSS algorithms.
3. To validate how well the technological demonstrator performs in measuring signal effects.
4. To be able to study a dynamic mission worst case scenario via technological demonstrator simulation. Performance metrics for the case study will be designed ad-hoc.
5. To perform a quantitative study of how some different Galileo and GPS signals perform in specific high dynamic scenarios (LEO scenario).
6. To implement software receivers and architectures to tackle the problem of the high computational burden associated to GNSS high dynamic scenarios (LEO scenario).

1.2 Thesis outline

The main goal of this work is to study GNSS receiver architectures using a technological demonstrator. The work methodology is based on the SDR philosophy. The idea behind SDR is to implement functions which are traditionally implemented using specific embedded systems based on Field Programmable Gate Array (FPGA) or Application-Specific Integrated Circuit (ASIC) using a personal computer. The SDR based technological demonstrator that has been configured is composed of three main blocks, i.e. signal generator, RF front-end and PC software tools. The first element is the GNSS signal generator. In this work, a Spirent GSS7700 and a Rohde & Schwarz SMBV100A signal generators are used to simulate a GNSS signal which resembles very closely the signal just as it is received by the receiver front-end. The Spirent GSS7700 simulator is capable of simulating high dynamic scenarios, ionospheric and tropospheric effects, jamming or multipath and fading scenarios. The Spirent GSS7700 simulator is used for the generation of GPS signals for the LEO scenario. For simulations of Galileo LEO scenarios, a Rohde & Schwarz SVB100 signal generator will be used.

The second block is the Radio-frequency front-end, which is in charge of receiving and digitizing the RF signal. We will use both a USB-dongle based on the RT820 tuner and the RTL2832 demodulation chip (like in [42]) which is controlled using the RTL-SDR

driver and a high-end RF front-end (with increased frequency stability, dedicated synchronization tools and improved RF figures of merit) such as the USRPX310 (which will be used too via USRP Hardware Driver (UHD) driver. The last block in the GNSS SDR philosophy is the software part. Once the I/Q samples are fed to a PC, software programming tools shall be used to process them. Matlab or GNU Radio codes to implement different GNSS receiver architectures can be implemented.

The reasons behind the choice of using a SDR philosophy can be summarized in the following manner according to the points stated in [41]:

1. The usage of the SDR methodology results in a very flexible environment (one can use many software solutions to implement the GNSS receiver i.e. Matlab, Scilab, C/C++, GNU Radio, GNSS-SDR, which is based on GNU Radio but allows to tune some receiver parameters...).

2. Depending on the application, one can use a very low-cost dongle, a high-end Universal Software Radio Peripheral (USRP) or any other solution that allows feeding a PC with I/Q samples.

3. The fact the samples are available enables the possibility to design at will each and every block comprising a GNSS signal processing chain, which is a necessary feature for receiver implementation and testing.

4. By using a GNSS signal generator, it is possible to control the signal parameters and the signal generation experiments are repeatable. This is not the case when working with real case scenarios, where the signal parameters are not identical from experiment to experiment. This is a big advantage as uncertainty is greatly reduced.

5. Once the receiver is embedded for a specific application, it is possible to upgrade or update the receiver architecture by changing the software. For example, one can modify the receiver architecture in a software GNSS embedded receiver by sending appropriate information from a ground station.

6. Matlab and GNU radio are able to parallelize algorithms automatically if a Graphics Processor Unit (GPU) is detected. This extended feature is interesting when trying to find out if the usage of Graphics Processor Unit (GPU) is actually cost-effective. Furthermore, the usage of software that include this functionality and allows to use the Graphics Processor Unit (GPU) functionality without actually having to increase the programmer effort, is readily available.

Fig 1.2, shows some different options for the implementation of each block.

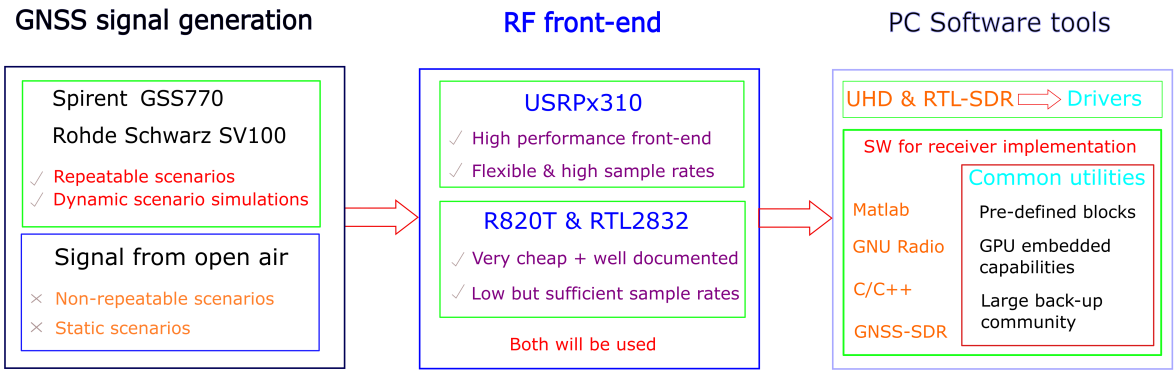

Figure 1.2: Block diagram.

Recalling the above-mentioned advantages many GNSS researches are conducted using [41] the SDR philosophy.

Within the GNSS receiver, the acquisition stage is also referred to as the detector [9, 10], acquisition scheme [3] or integration techniques [2]. Moreover, different implementations of these detectors exist. Hence, the acquisition signal techniques can be classified attending to different criteria.

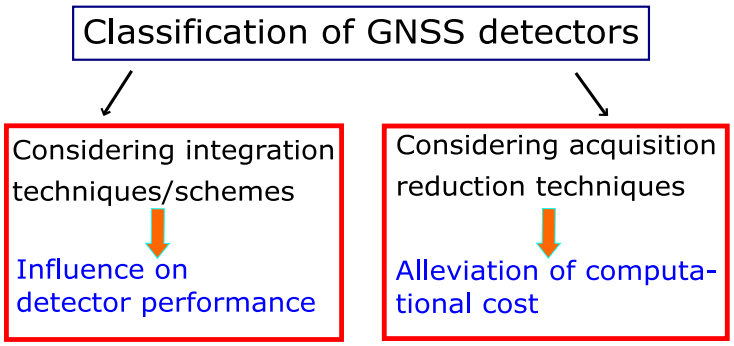

Figure 1.3: Detector classification.

Attending to Fig 1.3, the detector schemes can be divided depending on two independent classification criteria. The way in which the detector forms the decision statistic determines the receiver detector performance. The optimal detector is the coherent or maximum likelihood detector [3, 9, 10], however this detector suffers when dealing with data bit reversal and lack of synchronization. The non-coherent detector succeeds in dealing with the data bit reversal, but it is not optimal sensitivity wise as the coherent detector is. The differentially-coherent detector family constitutes an attempt to integrate the data bit reversal immunity (when compared to the coherent detector) and the optimal detection of the coherent detector, as the differentially-coherent detector reduces the noise

power at the decision statistic output in some scenarios [43]. Finally, the pre-correlation detector is immune to receiver dynamics and data reversal at the cost of an important sensitivity loss. Each detector scheme can be implemented in slightly different ways and some of the different implementations for each detector scheme will be studied. In order to understand the organization of the work performed, it is necessary to understand that different implementations and receiver schemes exist. Ongoing research on GNSS detectors has yielded new detector strategies and efficient implementations. Another important aspect to bear in mind is that as the GNSS signals have been modernized, new detection schemes that take advantage of the new signals have been designed and implemented. Modernized GNSS signals include pilot and data channel. The pilot channel can be used exclusively for signal detection because the pilot channel does not include data modulated signals. In this way the coherent integration time can be increased without having to face the bit reversal problem. However, the correlations of the data and pilot channels can also be combined to enhance receiver performance [44, 45].

In view of the points presented in this section, the thesis outline is as follows:

1. In first place, the different GNSS systems are presented, with special focus on Galileo and GPS.

2. The high dynamics scenario and the processes in which the GNSS receiver design is accommodated to the receiver dynamics are explained.

3. In order to give context to the research, an introduction to GNSS statistical receiver theory is provided. Once the statistical theory is presented, the different detector architectures are presented. Advantages and disadvantages linked to the usage of the different architecture types in the frame of the LEO GNSS scenario will be identified, analyzed and discussed.

4. A study considering the different signals for the high dynamic scenario is carried out. Moreover, different receiver implementations that increase the acquisition efficiency are presented.

5. The pre-correlation differential detector is fully characterized in a statistical fashion. A proof of concept study to consider the usage of this detector for a LEO-embedded receiver is performed.

6. A study considering a modification of the Doble Block Zero Padding (DBZP) algorithm for a LEO embedded GNSS receiver is carried out.

1.3 Thesis contributions

The work included in this PhD thesis has contributed in the following points:

1. Improve the understanding of the different GNSS signal's performance in specific high dynamic scenarios by providing a theoretical performance study for different well-known detection algorithms and GPS and Galileo signals.

2. New experimental procedures for the validation of a SDR technological demonstrator are described and validated.

3. A characterization of the standard so-called pre-correlation differential detector (and some slightly different implementations) and its application to the LEO GNSS scenario. The receiver feasibility for the LEO scenario is demonstrated empirically.

4. A complete discussion on the usage of the modified DBZP algorithm in LEO scenarios is provided. Experiments that demonstrate that the theoretical sensibility and speed-up match are performed.

A journal publication in Navigation, journal of the institute of navigation "A Proof of Concept Study for a Fast Acquisition in a LEO Satellite GPS Receiver, which can be accessed at https://doi.org/10.1002/navi.224" has been produced in the frame of this work, in order to publish the results included in chapter 5 of this work.

A conference publication "A Performance Comparison Study for GNSS Receivers in High Dynamics Context" has been produced to sum-up and publish the research results of chapter 6 of this work.

Chapter 2

GNSS basics

The aim of this section is to present the conceptual working principle of all GNSSs. Afterwards we will move forward to present the features of the Galileo and GPS available signals. By knowing the features of the GNSS signals, the suitability of these signals for a high dynamics scenario can be assessed. The proposed workflow is as follows:

Figure 2.1: Workflow.

2.1 GNSS conceptual framework

All of the GNSSs share a specific structural framework [46]. A GNSS infrastructure comprises three different segments dealing with different aspects which are necessary in the deployment of GNSSs. These three segments are:

1. Space segment.
2. Control segment.
3. User segment.

The space segment comprises satellites distributed in a number of orbital planes. These satellites, transmit the RF signal to users (GNSS receivers) continuously. For GPS, the space segments are placed in a Medium Earth Orbit (MEO) at an altitude of 20200 km and the 31 (as of May 2018) space segment satellites are placed on six orbital planes each of which are inclined 55°. This configuration aims to make 24 satellites available 95% of the time. The core constellation includes just 24 GPS satellites, however extra satellites are added to increase GPS performance but these satellites are not part of the core constellation. As of May 2018, the core constellation is complemented by 7 spare satellites operating in different orbital planes. The satellites have a specific lifespan and the constellation must be replenished at regular intervals. Therefore, different satellites from different generations co-exist. As of May 2018, 1 satellite from the so-called IIA block (generation), 11 from the IIR block, 7 from the IIR-M block and 12 from the II-F block are in operation. Each subsequent generation includes improvements in specific areas. For example, the next satellite generation (GPS III) foresees to include a new civil signal and increased signal accuracy and reliability. The Galileo space segment will be composed of a constellation of 30 satellites with three orbital planes at an altitude of 23222 km. The full GLONASS constellation consists of 24 satellites. GLONASS satellites orbit the Earth with space segment satellites distributed in three different orbital planes which are evenly spaced by 120°. GLONASS satellites target inclination is of 64.8°, which is actually quite higher than the target inclination of GPS satellites. The different GNSS segments are illustrated in Fig. 2.2.

The control segment of any GNSS is formed by a global network of ground stations in charge of tracking the state of some specific parameters of the signal transmitted by space segment satellites. Moreover, the ground stations send commands and data to the constellation to make the navigation data sent by the space segment satellite more accurate.

In order to illustrate the conceptual framework of a GNSS control segment, the control segment of GPS will be briefly depicted.

Three different functional elements compose the current control segment: a master control station (for redundancy considerations, an alternate master control station does also exist), monitor stations and ground antennas. The master control station is in charge of controlling the whole constellation. To do so, it must perform the following tasks:

1. Compute the precise location of space segment satellites to obtain information to broadcast orbit correction messages.

2. Transmit navigation data to satellites.

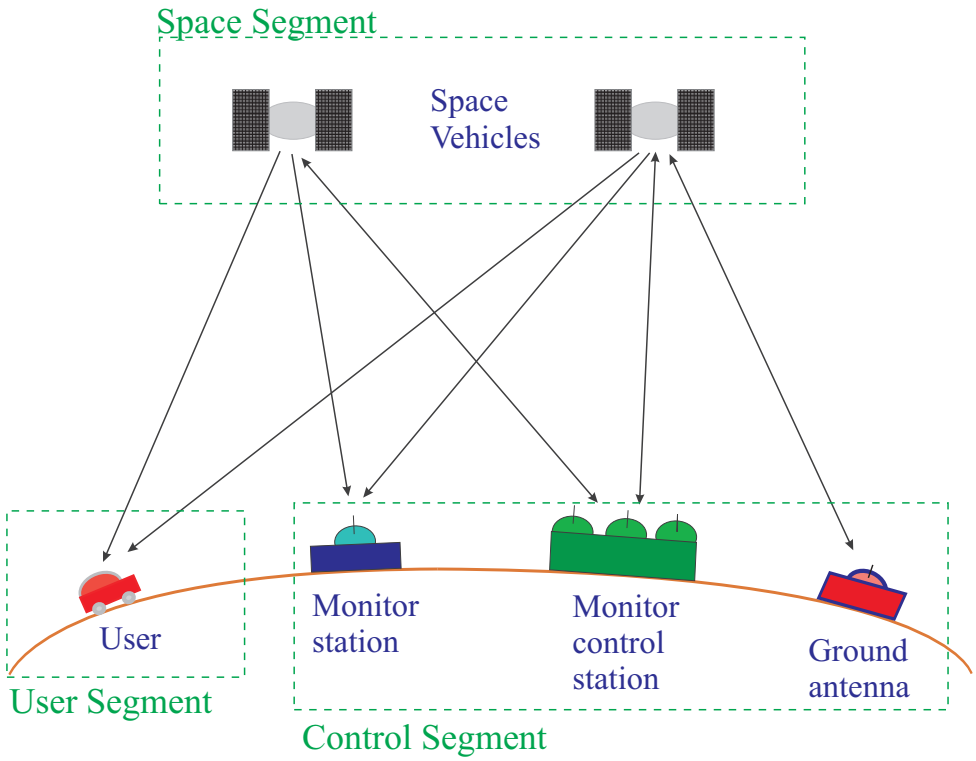

Figure 2.2: GNSS segments.

3. Management of control strategies for satellite repositioning for constellation optimization purposes.

Up to 16 monitor stations are in charge of tracking the navigation message of the satellites. These monitor stations use high-end GPS receivers (the precision required to perform these tasks can be only achieved by using high-end receivers) to perform range and carrier measurements and collect atmospheric data. The data collected is passed for processing to the master control station. The 11 ground antennas collect telemetry and upload navigation data. The communication is performed using the S frequency band, and a ranging procedure must take place in order to monitor the space segment satellite orbits.

Finally, the user segment is composed by the GNSS receiver. At this point it is clear that a receiver is a vital part for GNSS to work as positioning is not possible without a receiver. Accordingly, the user segment is the last segment of the structural framework.

2.2 Working principle

The concept in which all of the GNSS rely on, is the trilateration principle. The trilateration principle states that in order to find out the position of a specific point in space, it is necessary to calculate the distance between three reference points (whose positions are known) and the point whose position is an unknown. When the distance between a reference point and the point whose position is an unknown is measured, we calculate the range between the two points. By finding the range, we can place the unknown point anywhere on the surface of a sphere, whose radius is the range and whose center is the reference point. Once the first measurement is performed, if we repeat this measurement operation two times, using two different reference points, then we are able to find the unknown position relative to the three reference points. We know that the unknown point must be placed on the intersection of the three ranging spheres and having access to the value of the three ranges, it possible to determine the unknown point. A 2-D representation of the positioning principle is shown in Fig. 2.3. A GNSS receiver placed on the earth surface uses the signals coming from the satellites to obtain distances R_1 and R_2. Knowing these two distances and the satellites position, the user position can be obtained by solving the simultaneous equation resulting from the circle equations whose centers are the position of both satellites and with radii are R_1 and R_2.

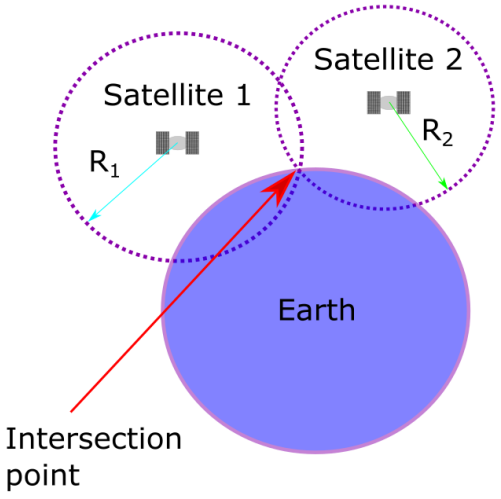

Figure 2.3: Positioning principle.

GNSS systems use space segment satellites as reference points, by taking advantage of the precision of the atomic clocks employed.

The conceptual workflow of GNSS positioning is explained in Fig.2.4.

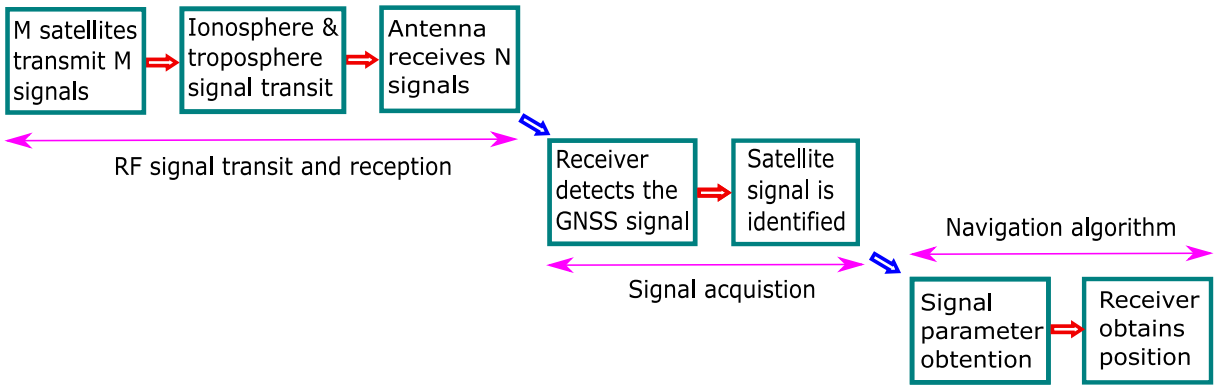

Figure 2.4: GNSS flowgraph.

Each of the M space segment satellites transmits a different signal. In this way, each satellite has its own specific signal signature. The signal passes through space and passes through the ionosphere and the troposphere (these layers act as lenses and as a consequence the GNSS signal does not propagate following a straight line [47]). Each signal arrives at the receiver antenna with a different delay. For each temporal snapshot, the receiver antenna receives N (where N<M) GNSS signals. The number of signals impinging the receiver antenna is variable and depends on the time of the day. Taking into consideration that many GNSS signals are received at the same time, the receiver must have a means of distinguishing the identity of each of the received signals i.e. which satellite signal is being received. Therefore, the transmitted signal is designed in such a why that the receiver is able to detect the signal. The signal identification can be achieved via two different channel access techniques can be employed. The most common technique is the Code Division Multiplexing Access (CDMA) technique. In order to implement a CDMA channel access, each satellite transmits a specific code. The receiver knows which code corresponds to each satellite. The satellite identification is implemented using the correlation concept. Generally, a GNSS receiver calculates M correlations in parallel (one per satellite) [32]. In every channel the input signal is correlated with one of the M possible codes. If a correlation peak appears in channel i (with i<=M), then a signal is detected and knowing that each satellite transmits a specific code, then if the correlation peak appears in channel i, then the detected signal comes from satellite i. The CDMA technology is used for all GPS and Galileo signals. The other channel access technology, is Frequency Division Multiplexing Access (FDMA). In FDMA each satellite signal transmits a different frequency and if the receiver knows which satellite transmits a specific frequency, then it is possible to identify the satellite signal by finding out the received frequency. Some GLONASS signals use FDMA [48].

The GNSS signal design enables to distinguish the signal transmitted by every different satellite, however in order to implement the trilateration process a ranging mechanism must be provided. GNSS implement the ranging mechanism by using two different layers. Lets recall here a simplistic GNSS signal model in order to illustrate the way in which the two layers are used in the ranging process.

$$S = \sqrt{P(t)}C(t)D(t)\cos(2\pi f_{L1}t) \tag{2.1}$$

$C(t)$ is the so-called ranging signal and $D(t)$ is the data signal. $P(t)$ is the power of the transmitted signal. The ranging signal is a pseudo-noise random signal with the appearance of rectangular pulses that can take one or minus one as values. These rectangular pulses are known as chips. GPS and Galileo operate using a Direct Sequence Spread Spectrum Code Division Multiplexing or DSSS-CDMA. This means that the data signal is modulated by a ranging signal whose bandwidth is much larger than the bandwidth of the data signal [32]. Therefore, the narrowband data information is spread across the frequency band, keeping the signal well below the noise power level [5, 9, 49]. To better understand the context of the C/A signal, lets state that the code for the GPS L1 band has a duration of 1 ms and 1023 chips. The data signal has a bandwidth of 50 Hz. At the end of each chip the pulse value can change from chip to chip (hence the chip concept refers to the time instant at which the code value can change). As stated, each satellite transmits a different ranging signal. The ranging signals are designed in such a way they have very small cross-correlation between them and a very high auto-correlation [50]. Hence, it is possible to detect a specific incoming signal via correlation. The different positions in which the correlation peak can appear corresponds to different propagation times. The propagation time is obtained by recalling the following expression:

$$t = t_0 + nt_{chip} \tag{2.2}$$

Where t_0 is the integer number of periods during the signal transit time, t_{chip} is $1/1023 = 977.5$ μs and n is the number of chips to complete the propagation time. Using the propagation time, it is possible to find out the distance between the satellite and the receiver. However, the measured propagation time is affected by a series of perturbations. Therefore, when multiplying the measured propagation time with the speed of light, the result is not the actual distance between the transmitting satellite and the receiver. The result of this multiplication is called pseudorange. In order to obtain an accurate estimation of the distance, one has to consider the following factors affecting the measured pseudodistance. These are among others:

1. Transmitting satellite clock bias.
2. Error in the satellite orbital position.
3. Ionospheric delay.
4. Tropospheric delay.
5. Relativistic effects.
6. Receiver clock bias.

In order to mitigate these effects (at receiver level), the data signal transmits contains information which is necessary for the positioning process. This functionality is included by adding second layer in the GNSS. The second necessary layer in GNSS signals is the data message information $D(t)$. The data message contains information concerning satellite clock bias correction, satellite orbit information and ionospheric correction parameters.

In high dynamics scenarios, one has to recall the fact that when the relative motion between the satellite and the receiver appears, a corresponding Doppler effect appears. This Doppler effect causes a variation in the received frequency (known as frequency drift) and causes a widening or tightening of the ranging code pulses (which is in fact a change in the code chip frequency [5]). Moreover, the cross-correlation of the ranging code can be degraded in the high dynamics context [50]

2.3 GNSS signals for high dynamics scenarios

The main objective of this work is to study GNSS receivers in high dynamics scenarios. Hence, finding out which of the GNSS signals cope the best with the inherent constraints of this scenario is an issue of paramount importance. The first step in the evaluation of the different GNSS signals in high dynamics scenarios is to present the available signals provided by different navigation systems.Therefore, the different signals and bands of Galileo and GPS considering the signals that may be usable for the LEO high dynamics scenario are presented.

In this work we will just consider GPS and Galileo signals for the LEO satellite GNSS application, as GLONASS and Beidou are not part of the case study in this work. The different Galileo and GPS signals are presented, in order to point out in a reasoned manner the usage of which signals is feasible in the LEO scenario.

In first place we must take into consideration both GPS and Galileo operate in 3 different frequency bands at the same time. For GPS, the three bands are named L1, L2

and L5. For Galileo the three bands are named E1, E5 and E6. In Table 2.1, the central frequency of each band is shown.

Table 2.1: Central frequency of GPS and Galileo

GNSS band	Central frequency
Galileo E1	1.575420 GHz
Galileo E5	1.191795 GHz
Galileo E6	1.278750 GHz
GPS L1	1.575420 GHz
GPS L2	1.227600 GHz
GPS L5	1.176450 GHz

GNSSs transmit different signals in each band. GPS transmits military (with restricted access) and civil open service signals. Galileo transmits Open Service (OS), Commercial and Public Regulated Service (PRS) signals. The modernized signals transmit both data and pilot signals. The pilot signals only contain ranging code information in order to avoid the data transition problem during the acquisition stage allowing longer integration times which translates into an increased detector sensitivity. Accordingly, the pilot channel is used for the acquisition process (satellite detection and identification) and for the tracking process (signal parameters fine estimation and updating) [51]. Nevertheless, the pilot signals must be transmitted at the same time (bear in mind the data transmitted by the GNSS satellites is necessary for navigation) as the data signals and a multiplexing mechanism must be implemented. Quadrature-In phase representation of signals (I-Q representation) is used as a means of signal multiplexing. The following equation shows the analytic expression of the so-called I-Q representation, being S the transmitted signal.

$$s(t) = \sqrt{P(t)}I(t)\cos(2\pi f_{L1}t) - \sqrt{P(t)}Q(t)\sin(2\pi f_{L1}t) \tag{2.3}$$

The expression in Eq.2.3 comes from the result of the expression $\Re(S_{bb}\exp j2\pi f_{L1})$ [52], where S_{bb} is the baseband equivalent signal. It can be noted that I(t) and Q(t) are different and can contain different information, hence a means of multiplexing signals using the same frequency band has been provided.

The signals for each GPS and Galileo frequency band are described in the upcoming

section.

2.3.1 GPS L1 signals

As of May 2018 three GPS L1 different signals are being transmitted. These are:

1. C/A code signal.
2. P(Y) code signal.
3. M code signal.

When the new GPS III generation satellites are launched a fourth L1 signal will be available. This signal is known as the L1C signal.

The C/A code signal and the military P(Y) signal are the legacy signals which are multiplexed using the I/Q representation in the following way:

$$S_{L1} = \sqrt{P(t)}P(Y)\cos(2\pi f_{L1}t) - \sqrt{P(t)}C/A\sin(2\pi f_{L1}t) \tag{2.4}$$

By comparing 2.3 and 2.4, it is possible to notice that the C/A code signal is transmitted using the quadrature component and the military signal is transmitted using the in-phase component.

The L1 C/A signal repetition period is 1 ms and its baseband bandwidth is 1.023 MHz. Therefore, recalling the Nyquist theorem, a 2.046 Msps sampling frequency is enough to reconstruct the information (note here that this sampling frequency ensures working with a minimum bandwidth and is linked to a minimization of the acquisition process computational cost). However, the small chipping frequency is not beneficial when considering multipath protection [49], as the larger the chipping frequency, the narrower the code chip. The narrower the code chip, the more limited the range of the multipath delays affecting the receiver [53]. The data signal modulating the C/A ranging code operates with a data rate of 50 Hz. This modulation scheme is known as Binary Phase Shift Keying (BPSK) or BPSK-R1 which stands for BPSK with a code rate of 1.023 MHz (n.b. BPSK(1) stands for BPSK with a code rate of 1.023 MHz and BPSK(5) with a code rate of 5*1.023 MHz). In this modulation scheme, the information is represented using phase shifts at the beginning of the modulation pulses.

For the acquisition of a C/A code, just 2046 samples are necessary, and the fact just 2046 samples are needed, implies the computational cost is low in accordance with the needs in a LEO embedded receiver. At first glance, it appears that the L1 C/A signal is a good candidate for the LEO GNSS scenario. The In-phase signal is the military P(Y)

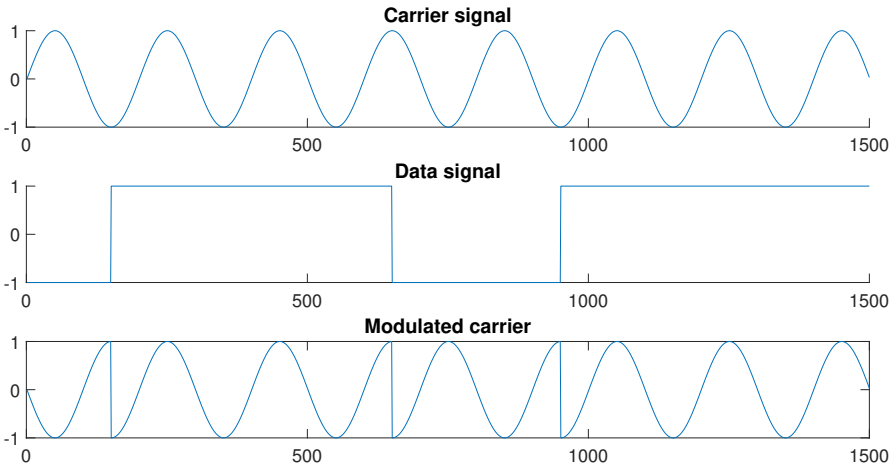

Figure 2.5: BPSK modulation.

precision signal, using a BPSK-R10 modulation. Considering the signal is a military signal, it is clear that the 10.23 MHz chipping rate is adequate to improve multipath protection and precision because of the narrower chip [53]. The P-code is a Pseudorandom noise (PRN) code with a repetition period of one week. The P-code is encrypted via a modulation using the so-called W code. Recalling the large P-code repetition period and the fact the fact the code is encrypted, the P-code will be considered no more in this work.

The C/A and P-code are the legacy signals. In the IIR-M block generation, a new military signal was introduced. This signal is named the M-code (Military code) signal. This signal has been designed to further improve jamming immunity and secure access of the military GPS signals. Furthermore, the M-code is transmitted simultaneously on the L1 and L2 bands to ensure further jamming immunity. The M-code is transmitted in the In-phase component, hence in order to ensure compatibility with the legacy P(Y) code the energy must be placed in a higher spectral band. This is done by using the so-called Binary Offset Carrier (BOC)(10,5) modulation. The BOC(10,5) modulation applies a sub-carrier modulation to produce a 10 MHz frequency displacement on the BPSK-R5 modulated signal. This is achieved by multiplying the PRN code by the sign of a sine wave. For example, the a BPSK(5) modulation is transformed into a BOC(10,5) modulation by multiplying the original PRN used in the BPSK(5) signal by the sign of a 10 MHz sine wave.

Another interesting feature of the M-code is the use of directional antennas allowing a 20 dB additional gain in specific regions. However, considering the fact the military code is encrypted this signal will be considered no more in this work.

In the upcoming GPS III generation, a new civil signal is included, the so-called L1C. This signal transmits a pilot and a data component. The data component is transmitted in the In-phase component and the pilot component is transmitted using the Quadrature component. To guarantee backward compatibility with the original L1 C/A signal, the data component uses a Time Multiplexed Binary Offset Carrier (TMBOC) modulation. The TMBOC modulation is a time-multiplexed combination of a BOC(1,1) modulation and the BOC(6,1) modulation.

It is necessary to consider that as the PRN repetition period increases, so does the correlation isolation properties. Unfortunately, as the PRN repetition period increases, so does the computational cost associated to the implementation of the acquisition scheme. For the pilot component, the modulation bandwidth is 14.322 MHz and for the data component the modulation bandwidth is 4.092 MHz, therefore a minimum sampling of 28.644 Msps and 8.184 Msps respectively must be utilized. These sample rates along with the 10 ms code repetition period translate into a code period with sample lengths of 143220 and 40920 samples respectively. If one compares the sample length of one C/A code period with the sample code length of the L1C data component, a $\frac{40920}{2046} = 20$ times increase in the sample length is observed. If computational cost considerations are put forward into first place, then the use of the L1C signal should be discarded in the high dynamics scenario. Nevertheless, the fact the code length is ten times the C/A code length implies that the times ten increase in the correlation length can be partly compensated by the fact a finer frequency domain resolution with no extra computational cost is achieved. The compensation is not complete because the computational cost of 10 FFT operations of N points is smaller than the computational cost of one $10N$ points FFT operation, as the cost in operations of an N point FFT is $Nlog_2(N)$ [54]. To answer which signal is linked to a smaller computational cost, a quantitative study comparing the L1 C/A and the L1C codes, is performed in section 3.5.1. However, the computational cost consideration can only hold if the the focus is just set on computational cost considerations because the usage of the L1C signal implies significant improvements as listed below.

1. Longer codes imply better cross-correlation properties.
2. Data and pilot components broaden the plethora of processing possibilities, enhancing the overall performance.
3. Modernized CBOC modulation enables improved performance.
4. Improved data transmission via Cyclic Redundancy Check (CRC) and Viterbi algorithms.

For the C/A code, the minimum earth received power is -128.5 dBm, the L1C and the M-code minimum earth received power is -127 dBm [55]. Finally, the P(Y) code minimum earth received power is -131.5 dBm

2.3.2 GPS L2 signals

The L2 civil signals are only available for Block IIR-M and subsequent satellite vehicles. The baseband expression for the L2 signal is:

$$S_{L2} = e_{L2I} + je_{L2Q} \tag{2.5}$$

The in-phase e_{L2I} component is exactly the same as in the GPS L1 signal, carrying the precision code signal (to ensure redundancy for military applications).

The quadrature component e_{L2Q} transmits the so-called L2 Civil Moderate (L2 CM) code and the L2 Civil Long (L2 CL) code.

The L2 CM code uses a ranging code, which has a time duration of 20 milliseconds and uses a chipping rate of 511.5 kbps, resulting in a 10230 chip length code. The CM code is used to transmit the navigation data and hence is referred to as the L2C data component.

The L2 CM is modulated with the so-called CNAV navigation data message. The CNAV message is transmitted at a 25 bps rate, but it is coded using a Forward Error Correction (FEC) with a convolutional encoder which finally outputs symbols at a rate of 50 sps. When the FEC is used, redundant bits are transmitted following a known method. In this way it is possible to detect and correct the errors that may be introduced by noise, interference, or fading [49]. Furthermore, the block II-F satellites are capable of using either the legacy navigation message used for the L1 CA code or the modernized CNAV.

The L2 CL code uses a chip rate of 511.5 kbps and a length of 767250 chips which translates into a period of 1.5 s. No data information is injected, hence the L2 CL component is referred to as the pilot component.

These two signals are time multiplexed in order to obtain a resulting chipping rate which is twice the chipping rate of each individual signal. The chipping rate of the L2 CM and L2 CL signals is of 511.5 kbps individually. However, after the time multiplexing, the composite signal results in a stream of 1.023 Mbps. Hence, the minimum sampling frequency is 2.046 Msps. Consequently, for the L2 CM signal, the minimum number of samples per code is $20 \times 2046 = 40920$ samples. For the acquisition of the L2 CL code, at least $1500 \times 2046 = 3069000$ samples are necessary. If computational cost is than the L1 C/A signal. Nevertheless, the fact the L2 frequency is smaller than the L1 frequency

implies the L2 signals are less affected by the Doppler frequency. The Doppler search space is accordingly $\frac{L2}{L1}$ times smaller than the search space for the L1 frequency. The same reasoning can be used to study the Code Doppler.

The minimum received power for the L2 GPS signals spans from -134.5 to -128.5 dBm [55], depending on the generation of the space vehicle transmitting the signal.

2.3.3 GPS L5 signals

The GPS L5 band also uses the in-phase quadrature representation, the L5 data channel corresponds to the in-phase component and the L5 pilot channel corresponds to the quadrature component. Quadrature Phase Shift Keying (QPSK) is used to combine an in-phase signal component and a quadrature signal component, which are modulated using a independent BPSK(10) modulated signal. Therefore, it is possible to process the in-phase or quadrature channels independently. The PRN codes for the L5 GPS have a repetition period of 1 ms and considering a BPSK(10) modulation is employed, a sampling frequency of 20.46 MHz is required. Therefore the length in samples of a sampled L5 code is 20460 samples which is comparatively much higher than the minimum sampling frequency for the L1 C/A signals, which makes the use of this signals less advisable in a high dynamics scenario.

The in-phase component is the data component which is modulated by a 50 bps navigation data, which translates into a 100 baud symbol rate after a convolutional FEC encoding. Furthermore, Neuman-Hofman (NH) synchronization codes are modulated on the I-Q components at a 1 kbaud rate. Every 1 ms, the NH code is modulo-2 added with the PRN code chip. For the in-phase component, the PRN code repeats 10 times each 10 ms interval. The start of the in-phase NH code is aligned with the start of each 10 ms data symbol produced by the FEC encoding. The quadrature NH code is synchronized with the 20 ms data bits.

The minimum received power for the L5 GPS signals spans from -127.9 to -127 dBm [56], depending on the generation of the space vehicle transmitting the signal.

2.3.4 Galileo E1 signals

The Galileo E1 band uses the In-phase, Quadrature representation mechanism. The in-phase component transmits the OS signal. The E1 OS signal transmits two equal power data and pilot components. Moreover, the E1 OS signal uses a Composite Binary Offset Carrier (CBOC) modulation. The CBOC modulation combines a BOC(1,1) modulation and a BOC(6,1) modulation.

More specifically, the E1 Open Service Data channel $S_{E1}(t)$ follows the mathematical

expression in Eq. 2.6.

$$S_{E1}(t) = \frac{[e_{E1-B}(t)(\alpha S_{C_{E1-B\alpha}}(t) + \beta S_{C_{E1-B\beta}}(t)) - e_{E1-C}(t)(\alpha S_{C_{E1-C\alpha}}(t) - \beta S_{C_{E1-C\beta}}(t))]}{\sqrt{2}} \tag{2.6}$$

A diagram showing how the expression in 2.6 is implemented, is shown in Fig. 2.6:

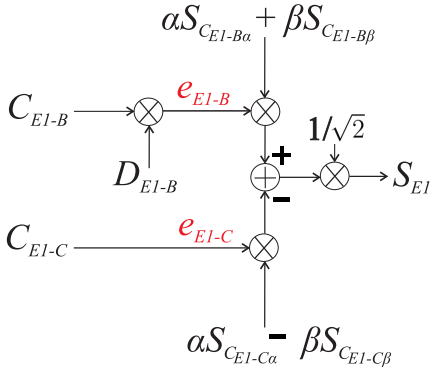

Figure 2.6: E1 diagram.

The value for α is $\sqrt{\frac{10}{11}}$ and β is $\sqrt{\frac{1}{11}}$. From the above equation it follows that the BOC(1,1) component takes $\frac{10}{11}$ of the power and the BOC(6,1) component takes $\frac{1}{11}$ of the power. Taking into consideration that the BOC(6,1) just uses $\frac{1}{11}$ of the power, it is possible to just process the E1 OS signal using the BOC(1,1) ignoring the other signal component. The $e_{E1-B}(t)$ is generated by a modulo-2 addition (respectively product if we consider the physical bipolar representation of the signal [57]) of the navigation message $D_{E1-B(t)}$ and the $C_{E1-B\alpha}$ ranging code. This modulation scheme used by both the the pilot and data component is the so-called CBOC(6,1,$\frac{1}{11}$) modulation. The $D_{E1-B(t)}$ navigation message has a symbol rate of 250 symbols/s. The C_{E1-B} and C_{E1-C} are pseudorandom memory codes with a chip rate of 1.023 Mchips/s. C_{E1-B} has a duration of 4092 chips and C_{E1-C} has a duration of 25×4092 chips. The $S_{C_{E1-B\alpha}}(t)$, $S_{C_{E1-B\beta}}(t)$, $S_{C_{E1-C\alpha}}(t)$ and $S_{C_{E1-C\beta}}(t)$ are sub-carrier signals in charge of implementing the BOC modulation with the expression described in Eq.2.7.

$$S_{cx} = \text{sgn}(\sin(2\pi R_X t)) \tag{2.7}$$

Where sgn represents the sign operator and R_x represents the variable data rate of the code. In Table 2.2, the different sub-carrier rates are shown in Table 2.2.

If one wants to process the full CBOC(6,1,11) signal, it is necessary to employ a

Table 2.2: Sub-carrier rates.

Signal	Sub-carrier frequency
$S_{C_{E1-B\alpha}}$	1.023 MHz
$S_{C_{E1-B\beta}}$	6.138 MHz
$S_{C_{E1-C\alpha}}$	1.023 MHz
$S_{C_{E1-C\beta}}$	6.138 MHz

14.322 Msps sampling rate. Nevertheless if just the BOC(1,1) component is used, one only incurs in a 0.41 dB power loss [1]. Accordingly, a minimum 4.092 Msps sampling rate will be considered in this case. This sampling rate implies that for the E1 in-phase component, the minimum number of samples per code period is $4092 \times 4 = 16368$ samples. The same calculation for the pilot component yields $4092 \times 4 \times 25 = 409200$ samples The E1 PRS channel is transmitted using the E1 quadrature component, using a BOC(15,2.5) modulation. The PRS signal is classified and hence this signal will be considered no further in this work.

The minimum received power for the E1 Galileo signals is -127 dBm. Note here that for the E1 OS signal this power is shared equally between the pilot and data components. This fact translates in that the data component minimum received power is -130 dBm. The same applies to the E1 OS pilot component.

2.3.5 Galileo E6 signals

The Galileo E6 bands transmits the PRS signal (the same PRS signal as the PRS signal transmitted in the E1 band) using the Quadrature component and a commercial signal transmitted using the in-phase component. The expression for the E6 In-phase signal, is provided below in equation 2.8:

$$S_{E6}(t) = \frac{e_{E6-B}(t) - e_{E6-C}(t)}{\sqrt{2}} \tag{2.8}$$

The implementation of this mathematical expression is shown below in figure 2.7

The $e_{E6-B}(t)$ signal is a data modulated signal which results of the modulo-2 addition between the encrypted navigation data D_{E6-B} and the ranging code C_{E6-B}. The $e_{E6-B}(t)$ signal is a pilot signal, which is in fact the pilot ranging code C_{E6-C}. Both pilot and data ranging codes have a chip rate of 5.115 Mchips/s. The data signal rate

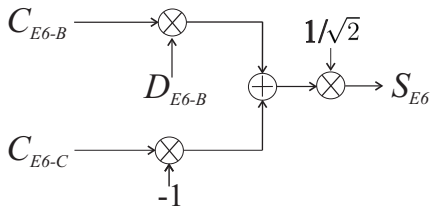

Figure 2.7: E6 diagram.

has a symbol rate of 100 sps. The fact the C_{E6-B} is encrypted implies this signal will be consider no further in this work.

The minimum received power for the E6 Galileo signals is -125 dBm.

2.3.6 Galileo E5 signals

The Galileo E5 band transmits three different signals intended for different uses, these signals are:

1. OS Open Service signal.
2. CS Commercial signal.
3. SoL Safety of Life signal.

In-phase and quadrature components are used generating a constant envelope signal. The in-phase component transmits the data component, whereas the quadrature component transmits the pilot component.

The Galileo E5 band contains four different signals. Two different components (a and b) with in-phase and quadrature components are part of the E5 Galileo band. These signals are:

1. E5a data channel (e_{E5a-I}): The signal transmitted through this channel is the result of the modulo-two addition of the E5a navigation data stream (F/NAV) D_{E5a-I} with the unencrypted ranging code C_{E5a_I}.
2. E5a (e_{E5a-Q}) pilot channel containing the unencrypted ranging code C_{E5a_Q}.
3. E5b data channel (e_{E5b-I}): The signal transmitted through this channel is the result of the modulo-two addition of the E5a navigation data stream (I/NAV), D_{E5b-I}, with the unencrypted ranging code C_{E5b_I}.
4. E5b (e_{E5b-Q}) pilot channel containing the unencrypted ranging code C_{E5b_Q}.

The ranging code chip rate for C_{E5a_Q}, C_{E5a_I}, C_{E5b_Q} and C_{E5b_I} is 10.23 Mchips/s. The F/NAV navigation message has a symbol rate of 50 symbols/s and the I/NAV has a symbol rate of 250 symbols/s.

The four signal components are processed to generate a signal with the so-called Alternative Binary Offset Carrier (AltBOC) modulation. The AltBOC modulation uses a subcarrier rate of 15.345 MHz R_{E5} ($T_{E5} = \frac{1}{R_{E5}}$). Spectrally, the AltBOC(15.345,10) modulation is analogous to two BPSK(10) signals shifted by 15.345 MHz to the left and right of the central carrier frequency [57].

The mathematical expression of the $S_{E5}(t)$ signal is:

$$\begin{aligned} S_{E5}(t) = & \frac{1}{2\sqrt{2}}[(e_{E5a-I}(t) + je_{E5a-Q}(t))[sc_{E5-S}(t) - jsc_{E5-S}(t - \frac{T_{E5}}{4})]]+ \\ & \frac{1}{2\sqrt{2}}[(e_{E5b-I}(t) + je_{E5b-Q}(t))[sc_{E5-S}(t) + jsc_{E5-S}(t - \frac{T_{E5}}{4})]]+ \\ & \frac{1}{2\sqrt{2}}[(\overline{e}_{E5b-I}(t) + j\overline{e}_{E5b-Q}(t))[sc_{E5-P}(t) - jsc_{E5-P}(t - \frac{T_{E5}}{4})]]+ \\ & \frac{1}{2\sqrt{2}}[(\overline{e}_{E5b-I}(t) + j\overline{e}_{E5b-Q}(t))[sc_{E5-P}(t) + jsc_{E5-P}(t - \frac{T_{E5}}{4})]]. \end{aligned} \tag{2.9}$$

Where $sc_{E5-P}(t)$ is the sub-carrier function for the product signals and $sc_{E5-S}(t)$ is the sub-carrier function for the single signals. In this equation, the first two terms are the single signal terms and the third and fourth terms are the product terms.

$$\overline{e}_{E5a-I}(t) = e_{E5a-Q}e_{E5b-I}e_{E5b-Q} \tag{2.10}$$

$$\overline{e}_{E5b-I}(t) = e_{E5a-I}e_{E5b-I}e_{E5b-Q} \tag{2.11}$$

$$\overline{e}_{E5a-Q}(t) = e_{E5b-Q}e_{E5a-I}e_{E5a-Q} \tag{2.12}$$

$$\overline{e}_{E5b-Q}(t) = e_{E5b-I}e_{E5a-I}e_{E5a-Q} \tag{2.13}$$

The first two terms can be processed independently as two separate QPSK signals with a carrier frequency of 1.17645 GHz and 1.20714 GHz respectively [58], but the complex $S_{E5}(t)$ signal prior to passband conversion can be described as an 8-Phase Shift

Keying (PSK) modulated signal accounting for its 8 different phase states. The AltBOC modulation helps in the mitigation of multipath and limits the impact of the ionospheric dispersion [59].

When processing the E5 signal it is necessary to use at least a 20.46 Msps if the signals are going to be processed independently or 51.15 Msps if the complete AltBOC signal is going to be processed. Considering that the code period is 1 ms, the code length in samples is 20460 if the components are processed independently or 51150 samples if the full AltBOC signal is processed.

Recall here, that the minimum received power for the combined E5 Galileo signals is -125 dBm, hence the minimum received power for both E5a and E5b components is -128 dBm.

2.4 GPS and Galileo signals under study

Once the different GPS and Galileo signals have been presented and explored, it is possible to move forward and determine which signals can be used. The available signals are shown in Table 2.3. Information on the minimum number of samples and the chip rate are included as this information is necessary in the discussion included in the following chapter. One of the factors under study in the next chapter is the computational cost associated to the processing in the acquisition stage and the sample code length is a limiting factor. Other effects under study are the influence of the Doppler effect or the minimum received power.

The GPS M,P and the Galileo E6 and PRS signals cannot be considered for the study, because the ranging codes are not publicly available. In view of the above-mentioned points the signals under study will be:

1. L1 C/A
2. L1C
3. L2C
4. L5
5. E1 OS
6. E5 OS

Table 2.3: Considered signals

Signal	Code length (samples)	Chip rate (Mcps)	Under study
L1 C/A	2046	1.023	Yes
L1C	40920	1.023	Yes
M	N/A	N/A	No
P	N/A	N/A	No
L2C	40920	1.023	Yes
L5	20460	2.046	Yes
PRS	N/A	N/A	No
E1 OS	4092	1.023	Yes
E6	N/A	5.115	No
E5 OS	20460	2.046	Yes

Using the information provided in this chapter along with the detector mechanisms presented in the next chapter, the pros and cons in using the available GPS and Galileo signals will be discussed [60].

Chapter 3

Receiver theory

In this chapter insight on the following aspects will be provided:

1. Describe a generic GNSS receiver and the tasks it performs.
2. Present the LEO signal scenario.
3. Present the GNSS signal statistical framework.
4. Present and analyze some different receiver types.
5. Discuss the limitations linked to the signal impairments that occur in the LEO signal scenario.
6. Compare the different available GNSS signals within the frame of the LEO scenario.

3.1 Introduction

The purpose of a GNSS receiver signal-processing chain is to obtain the necessary information for positioning. To accomplish this goal, the receiver must be able to detect if the signal is present and must provide a first coarse estimate of the signal code phase and Doppler frequency. This first step in the GNSS signal processing sequence is known as signal acquisition. In order to estimate the two parameters, the receiver needs to explore different possible combinations of code phase and Doppler frequency.

A GNSS receiver can be seen a series of blocks that perform specific tasks. The receiver antenna receives a composite signal formed by a sum of GNSS signals impinging

from different satellites of the space segment. Every satellite signal arrives with a different phase and a different delay. The carrier frequency of the received signal is actually different to the nominal carrier frequency due to the relative movement between the space vehicle and the receiver (Doppler effect).

Accordingly, the GNSS receiver must be able to:

1. Identify which satellite is emitting the signal that is received at every time epoch under analysis.
2. Estimate the signal transit time i.e. the time the signal needs to transit from the satellite vehicle to the receiver.
3. Estimate the Doppler frequency shift.
4. Track the detected signal, as the code phase and Doppler frequency change with time.
5. Use the parameters to find the receiver position.

Point 5 can only be achieved if the information which is transmitted by every satellite (satellite parameters which contain space vehicle ephemeris, clock bias, the time instant at which the signal was transmitted, ionospheric corrections...) is correctly decoded. Therefore, the GNSS receiver must devote resources to a decoding block.

The detailed block diagram shown in Fig. 3.1, describes the tasks a GNSS receiver must perform (bearing in mind that different receiver implementations exist). A complete GNSS receiver block diagram is shown in Fig. 3.1 a), in order to understand the context by which the acquisition process is surrounded. Moreover in Fig. 3.1 a), the GNSS block diagram highlights the GNSS receiver functions that can be implemented employing a SDR philosophy.

In this work, the focus is set on the acquisition block and this is why only details on this process are given. In order to identify the signal, the acquisition block performs a 2-D search. In this way the input signal Doppler frequency and the code phase are searched. This search can be computationally very demanding and the different search types can yield different algorithm execution speed. For example, a correlation operation implemented using the FFT correlation implementation is more computationally efficient [61, 62]. Depending on how the detector decides if the signal is present or not, different detector architectures can be implemented. Interestingly, these different architectures perform in a different manner depending on the signal context (for example some detectors are not sensitive to receiver dynamics but suffer when dealing with low power

level incoming signals [63]). Fig. 3.1 b), gives a general overview of the different acquisition process implementation options. In the top part of Fig. 3.1 b), a simple three step block diagram for the acquisition process is presented. Different possible conceptual implementations are named and presented in order to give an overview of the whole process.

Depending on how the acquisition process is implemented, different receiver classifications can be performed. According to [2], depending on how the integration and detection statistics are formed, one can classify GNSS in four different detector families (i.e. coherent, non-coherent, differentially-coherent and Modified General Differential Combination (MGDC)). [9,10], classify the detector families into coherent, non-coherent, differentially-coherent and pre-correlation families. The other main classification criterion, is the one which classifies taking into consideration the different acquisition complexity techniques. The so-called Multiple-dwell strategy can reduce computational cost by performing partial correlations to perform a coarse detection. However, this approach can only deal with high-incoming power signals and the selection of an appropriate partial correlation time is not easy [2]. The so-called hybrid-search strategies, perform the searching procedure by testing many hypotheses at the same time. This is achieved by implementing the correlation process via the FFT. Moreover, addtional reduction in computational cost can be obtained by combining the use of partial correlations and frequency domain shifting (Doble Block Zero Padding (DBZP) [1]) or by using 2-D FFT techniques [64]. The assisted-acquisition techniques rely on an external link that provides external information that can be used to reduce the search space (e.g. Mobile networks assistance [4]). Other methods reduce computational cost by performing a multisatellite search, but this detection type may lead to degraded output Signal to Noise Ratio (SNR) or may require fine frequency search correction which leads to a high computational cost [2]. Folding techniques reduce the computational cost by mapping several code chips into one ate the expense of a degraded output SNR [65]. Similarly, the so-called compressed sensing techniques take profit of the sparsity of the incoming signal to represent the incoming signal in such a way only the useful information is kept, whereas the redundant information is discarded [66]. Finally, the pre-correlation detector type reduces the computational cost by eliminating the input signal dependence with the Doppler frequency [63]. The DBZP and the pre-correlation detector reduce the frequency search space and hence their usage in wide Doppler search scenarios is appealing.

The different detector architectures are presented, highlighting the main pros and cons of each architecture.

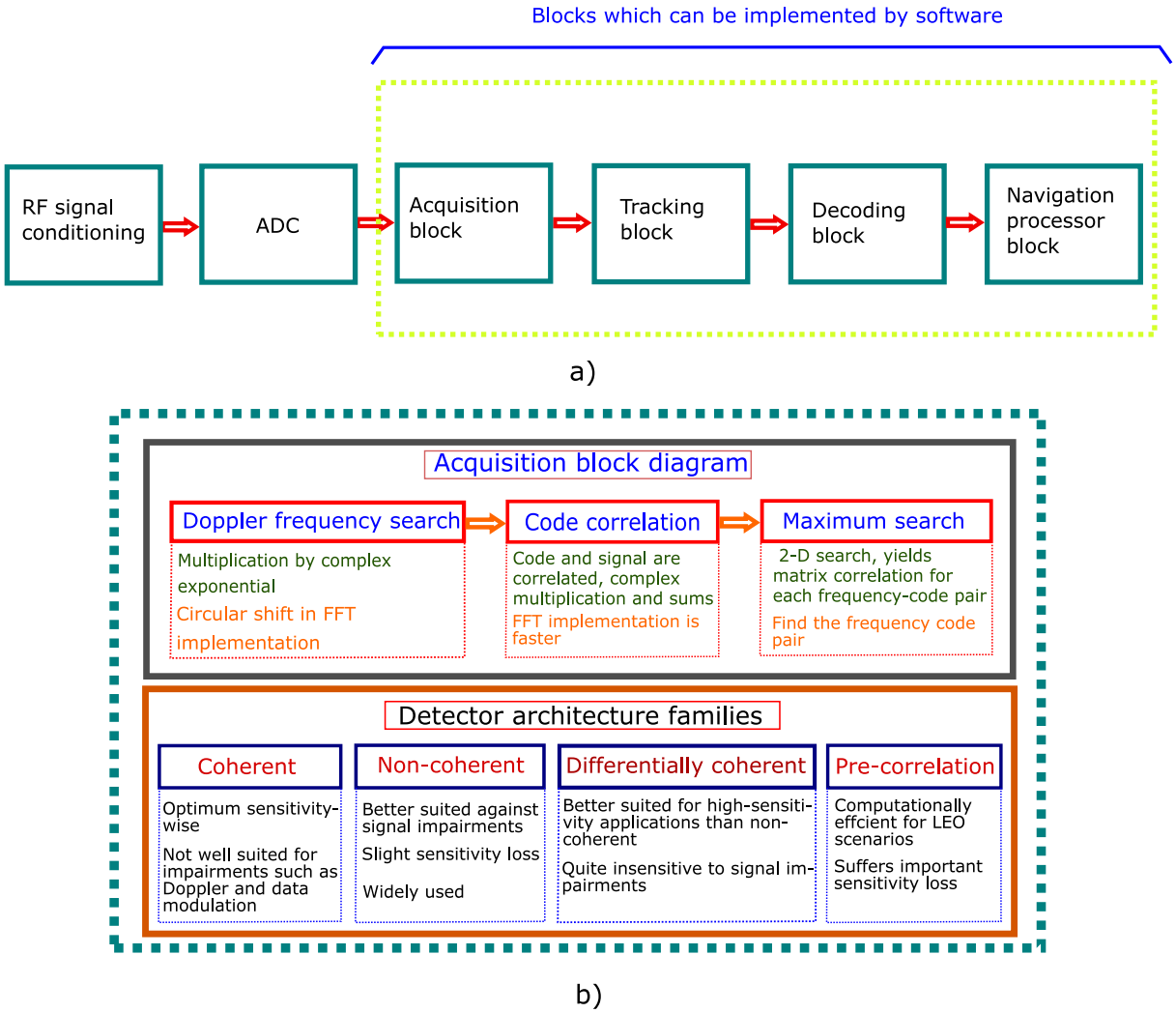

Figure 3.1: a) Acquisition within GNSS receiver b) detailed acquisition block diagram.

In a generic GNSS receiver, the RF signal passes from the antenna cable to the RF front-end. The RF front-end will take care of adapting the signal level in order to prepare the signal for the digitizing process. The RF front-end performs the following tasks:

1. Out-of-band interference mitigation.
2. Input signal amplification.
3. Signal frequency down-conversion to an intermediate frequency.
4. Signal sampling and quantization.

Once the RF front-end digitizes the signal, the samples are passed to the acquisition block, which is in charge of estimating the signal Doppler frequency and phase. The estimated parameters are then used by the tracking block to perform a finer parameter estimation and a signal parameter update (to account for the signal changing conditions). The precise and up to date parameters are then used to feed the navigation processor, which uses the estimated parameters and the decoded satellite information to calculate the user position.

In a high dynamics scenario, the acquisition process is critical because it is difficult to use Assisted Global Positioning System (AGPS) [4]. Furthermore, the receiver dynamics makes the acquisition process more costly and the specifications are more demanding because of the wide the Doppler search width. and the fast signal changing conditions. Therefore, a customized receiver design [30, 67] is required.

In this chapter, we will focus on how to deal with this demanding specifications. Moreover, we will review how the acquisition process can be adapted to cope with the high-dynamics scenario.

The acquisition block lies between the RF front-end and the tracking block. The acquisition block is a pure signal processing block because for parameter estimation, the information provided by the correlation operation result is compulsory. Therefore, taking into consideration the correlation is a signal processing operation it is clear that the acquisition process can be implemented via software.

3.2 High dynamics case studies

High dynamics scenarios are defined as cases in which receivers are embedded in vehicles subject to big accelerations or travelling at very high speeds. In these environments, the Doppler effect is important enough to have an impact on the tracking and acquisition processes. In order to use a GNSS receiver in these scenarios, the receiver must be customized in order to make operation possible.

Many different high dynamics scenarios can be considered. Some classic high dynamic scenarios are:

1. LEO satellite precise orbit determination.
2. Missile guidance.
3. Warplane guidance.

   In the upcoming section (3.2.1), the LEO scenario will be described and the reasons behind the choice of the LEO scenario case study are provided.

3.2.1 High dynamics LEO scenario

The high dynamics scenario under study is the case in which a GNSS receiver is embedded in a LEO satellite. The reasons explaining the high dynamics study case selected are presented. Moreover, a detailed study of the GNSS Doppler frequency will be provided.

At this point, it is important to state that the receiver dynamics affect severely the oscillator performance [68]. Accordingly, the LEO scenario the receiver is affected by the effect of the dynamics on the oscillator. However, this is not studied in this work. Actually, the empirical tests dealing with the study of this effect can be cumbersome and costly (as it is not easy to simulate the dynamics stress condition the receiver can suffer in space scenarios). The requirements for a LEO GNSS application are described. More specifically, the reasons to select this scenario are summarized in the following list:

1. Despite the fact the speed of a LEO satellite is very high and this implies the acquisition is more challenging for this scenario, the orbit is quite stable and predictable. Hence, it is appealing to use this scenario to extract conclusions easily.

2. Precise orbit determination for LEO satellites is a topic which is attracting great interest and GNSS receivers play a major role in this, as positioning is necessary for image retrieving, for instance. Therefore, any improvement in this field is of great interest.

3. The requirements for a LEO embedded GNSS receiver are different from the requirements for a ground application, due to the fast LEO satellite movement and to the different environmental conditions.

Before starting the study of receiver architectures for the LEO scenario, first, the defining characteristics defining the GNSS scenario must be highlighted. The defining requirements in a LEO GNSS application are described below:

1. In many LEO scenarios, the signal level is higher than the nominal signal level [30, 69, 70]. Moreover, signal distance travel is reduced, no tropospheric effects are present and the ionospheric effect is typically smaller [71] (except for low elevation satellites). In this scenario there is no need to use sensitivity enhancing algorithms [1,9,10,64,72], so it is interesting to test methods that work well only for high signal levels.

2. For LEO scenarios, the Doppler search span value is 100 kHz, instead of 10 kHz, which is the typical search span value for a static ground user [5]. The increased Doppler search translates into a bigger computational cost. The Doppler rate takes

values in the interval that spans from 50 Hz/s to 75 Hz/s [30, 70, 73]. These features represent the two main challenges in the LEO scenario.

3. In many LEO satellites power is limited and the receiver is turned on and off in many occasions [69]. Therefore, it is necessary to consider using computationally efficient algorithms

4. For LEO scenarios, the satellite passes can vary from 20 to 50 minutes [30]. This fact implies it is necessary to perform a fast acquisition.

In light of the points presented, when designing a GPS receiver for LEO space applications, the Doppler frequency search space must be adapted to be able to detect the satellite signal.

The Doppler dilation or contraction, arising from the relative motion between the GPS satellite and the receiver, which manifests as a time-varying carrier and code Doppler shift, must be considered when designing GPS detectors. To give some context on a realistic case study, some calculations to determine the theoretical maximum Doppler frequency shift are performed. In order to illustrate the points in this discussion, the values for the vastly used C/A GPS signal will be used.

The L1 frequency value in the case Doppler effect exists is named f'_{L1}, and can be expressed in the following form, [5, 74].

$$f'_{L1} = \frac{c + V_L}{c - V_S} f_{L1} \tag{3.1}$$

- c: Stands for the speed of light in free space.
- f'_{L1}: Doppler shifted L1 frequency.
- f_{L1}: L1 frequency.
- V_L: LEO satellite velocity component.
- V_S: GPS satellite velocity component.

For a 1000 km LEO, the values for V_L and V_S that maximize equation Eq. 3.1 are approximately 7.060 km/s and 1.014 km/s, respectively. If we define the Doppler frequency deviation f_d, as the difference between the nominal L1 frequency and the actual frequency received, then it follows that:

$$f_d = f'_{L1} - f_{L1}. \tag{3.2}$$

The substitution of these values into equation (1), yields the following result:

$$f'_{L1} = 1.57542 \cdot 10^9 \cdot \frac{3 \cdot 10^8 + 7.060 \cdot 10^3}{3 \cdot 10^8 - 1.014 \cdot 10^3} = 1.575462 \cdot 10^9. \tag{3.3}$$

Hence,

$$f_d = f'_{L1} - f_{L1} = 42.4 \quad \text{kHz}. \tag{3.4}$$

For the L2 frequency, Eq. 3.3 transforms into:

$$f'_{L1} = 1.2276 \cdot 10^9 \cdot \frac{3 \cdot 10^8 + 7.060 \cdot 10^3}{3 \cdot 10^8 - 1.014 \cdot 10^3} = 1.575462 \cdot 10^9. \tag{3.5}$$

Hence,

$$f_{dL2} = f'_{L2} - f_{L2} = 33 \quad \text{kHz} \tag{3.6}$$

The ratio between the nominal L1 frequency and the C/A code chip frequency is 1540, so the Doppler shift translates into a code Doppler shift of $f_d/1540$ Hz . Therefore, every chip drifts:

$$\frac{f_d}{1540 \cdot 1.023 \cdot 10^6} \quad \text{chips} \tag{3.7}$$

Hence, in 1 ms the code will drift

$$\frac{f_d \cdot 1023}{1540 \cdot 1.023 \cdot 10^6} \quad \text{chips} \tag{3.8}$$

If $f_d = 42.4z$ kHz, in 1 ms, the code drifts 0.0275 chips. For a 0.5 chip drift to occur, a 18.16 ms integration time must be used. It is worth mentioning that the code Doppler effect is much more harmful for wider band GNSS signals than for the C/A L1 signal. For a 200 km LEO orbit the maximum f_d value is 45 kHz, so accounting for the worst-case LEO scenario, the Doppler search space spans from -45 kHz to 45 kHz. In [30], a search space from -42 kHz to 42 kHz is used for a 300 km altitude LEO case study. At this point, it is wise to widen the frequency search space to gain some margin by adding 5 kHz to the search space, especially considering the receiver's clock drift must be considered too. Taking these points into consideration, the span of the search space for the LEO GNSS receiver is 100 kHz.

Using the above expressions, a graph showing the maximum Doppler frequency as a function of the LEO (orbit heights spanning from 200 km to 2000 km) satellite orbit height is presented in Fig. 3.2:

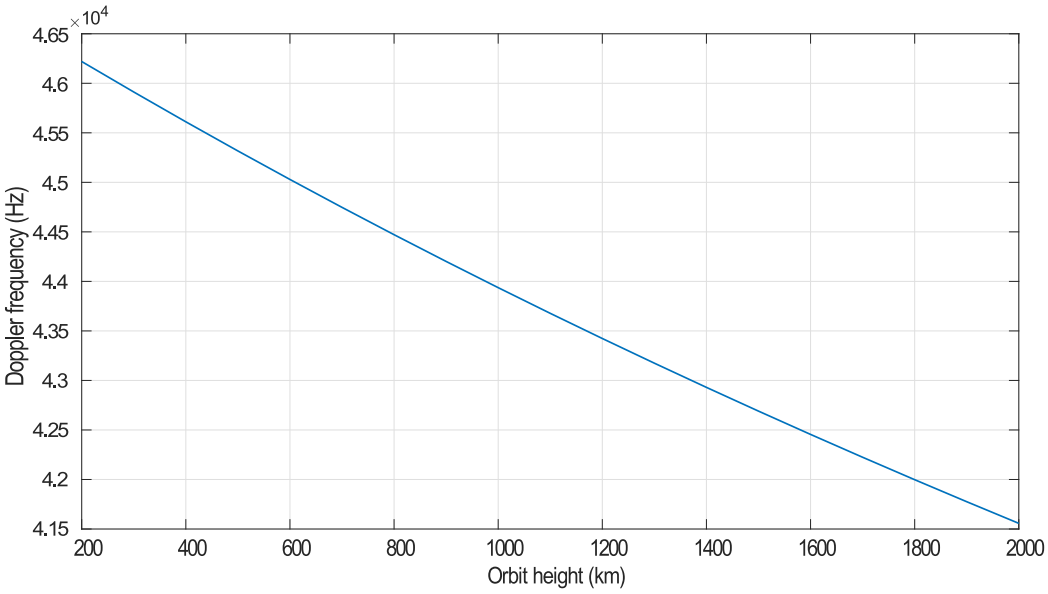

Figure 3.2: Maximum Doppler frequency vs orbit height.

The maximum Doppler frequency increases as the orbit height decreases, however for the LEO satellite orbit height range (200 to 2000 km) the change in the maximum Doppler frequency is not too significant (from 47 kHz to 42 kHz) and accounting for the receiver clock bias, the span of the frequency search range span is still 100 kHz.

When working with the GPS L1 C/A legacy signal, it is necessary to explore the 1023 possible code phase values. The width of the Doppler frequency search range depends on the relative velocity between the GPS satellite and the receiver. According to [5] and [4,49], the search space width for an earth-based receiver must be 10 kHz, accounting for a search range starting at -5 kHz and ending at 5 kHz. Considering the search space width is multiplied by a factor of ten, when comparing the earth-based static receiver with the LEO orbit satellite embedded receiver, it is appealing to study a method, which need not search in the two search dimensions i.e. the Pre-correlation detector. Moreover, in chapter 5, a performance study for this detector architecture within the LEO, is performed. However, first, some other detector architectures are studied to obtain information to compare the performance of the pre-correlation detector with the performance of the rest architectures under study.

3.3 Receiver statistical framework

In this section, the theoretical statistical framework describing the receiver synchronization process is presented. The synchronization process consists in the estimation of some of the received signal parameters. In order to present the statistical framework, a generic signal model for the received and sampled signal is presented below:

$$s(nTs) = \sqrt{P(nTs)}C(nT_s - \zeta T_{chip})D(nT_s - \zeta T_{chip})e^{j((w_d+w_L)nT_s+\theta_k)} + n_w \tag{3.9}$$

T_s: Sampling period.
n: Number of signal sample.
D: Data signal.
P: Signal power.
C: PRN ranging code.
T_{chip}: Chip period.
w_d: Signal Doppler angular frequency.
w_L: Carrier angular frequency.
$f_d = \frac{w_d}{2\pi}$: Signal Doppler frequency.
θ_k: Signal carrier random phase.
ζ: Percentage code chip phase offset.
n_w: Function modeling the channel's additive Gaussian noise.

According to [9] and [6], $n_w(nT_s)$ can be described using a complex normal distribution, composed of a real and an imaginary part, which are jointly normal and independent. By changing the code characteristics (length and correlation characteristics) and the data bit length, different GNSS signals are configured. Moreover, modernized signals use the so-called data and pilot components to improve performance. For a pilot GNSS signal, no data signal is transmitted and the data term in Eq. 3.9 should be dropped.

The signal synchronization process must estimate the following unknowns [9, 70]:

1. Signal power $P(nT_s)$.
2. Satellite identity.
3. Code phase offset ζT_{chip}.
4. Doppler frequency.
5. Data bit.

6. Signal carrier phase θ_k.

Taking into consideration that the synchronization process implies parameter estimation, it follows that the synchronization process is an estimation process. However, not all satellite signals are present at all times and the presence or absence of the signal must be determined in order to discard the presence of false peaks caused by noise random variations. This means that the estimation problem becomes a detection/estimation problem because first the satellite signal must be detected and once the signal is detected, the signal parameters must be estimated.

Speaking in practical terms, just two out of the six synchronization parameters are needed. Only the Doppler frequency f_d and the phase offset ζT_{chip} must be estimated. This estimation process is known as signal acquisition. These two parameters must be estimated, because their estimated values must be passed to the tracking block in charge of performing a fine estimation which is necessary to demodulate the data information transmitted by the space vehicles. The problem statement can be formulated as follows:

The input to the acquisition process is a vector of N received samples, which can be described as: $\mathbf{s}$=$[s(nT_s), s(2nT_s), s(3nT_s)...s(NnT_s)]$. Using this information, a vector of parameters $[f_d, \zeta]$ must be estimated. The estimated vector is $[\hat{f}_d, \hat{\zeta}]$. The question now is how to use the input data to obtain the best estimate of $[f_d, \zeta]$. To answer this question, first, the framework of statistical binary hypothesis testing must be established.

In a detection problem, two hypotheses must be tested. The H_0 hypothesis corresponding to the situation in which no signal is present and the H_1 hypothesis corresponding to the situation in which the signal is present. The mathematical formulation of this statement for a deterministic signal under Additive White Gaussian Noise (AWGN) can be expressed as:

$$H_0 : n_w(nT_s) \tag{3.10}$$

$$H_1 : s(nT_s) + n_w(nT_s) \tag{3.11}$$

The concept of conditional Probability Density Function (PDF) is necessary in order to describe non-deterministic signals involving white Gaussian noise. The PDF describes how probable is that the data vector takes a certain value i.e. a probability is assigned to each possible value. In the case of GNSS acquisition we work with conditional PDF because the probability distributions change depending if we are working with the H_0 or the H_1 hypothesis. For the H_0 hypothesis, we will work with the $P(s|H_0)$ distribution and for the H_1 hypothesis we work with the $P(s|H_1)$ distribution. These distributions

have variances σ_{H_0} and σ_{H_1}, respectively. The following notation is used when describing a binary hypothesis test:

- H_0: Stands for the hypothesis no signal is present.
- H_1: Stands for the hypothesis the signal is present.
- D_0: It is decided that the signal is not present.
- D_1: It is decided that the signal is present.

Four different situations can occur after a decision is made:

1. Decide D_0 given H_0 is true $\iff$ Correct rejection.
2. Decide D_0 given H_1 is true $\iff$ Incorrect rejection.
3. Decide D_1 given H_1 is true $\iff$ Correct detection.
4. Decide D_1 given H_0 is true $\iff$ Incorrect detection.

Using the PDF, four different probabilities can be defined:

1. $P_r \equiv$Probability of correct rejection. When decision D_0 is taken and H_0 is true.
2. $P_m \equiv$Probability of missed detection. When decision D_0 is taken and H_1 is true.
3. $PD \equiv$Probability of correct detection. When decision D_1 is taken and H_1 is true.
4. $PFA \equiv$Probability of false alarm. When decision D_1 is taken and H_0 is true.

From a detection framework point of view, it is well known that the optimal detector for deterministic signals under white noise is the so-called Neyman-Pearson (NP) detector [3, 10]. In the detection of deterministic signals under white noise, the H_1 rarely occurs. Accordingly, the NP criterion maximizes the detection probability for a fixed probability of false alarm. In order to take an optimal decision, different criteria can be utilized. The maximization of these criteria (Uniform Most Powerful (UMP) and NP), yields the so-called Likelihood Ratio Test (LRT) [3]. The test function for the LRT is:

$$\Lambda = \frac{P(s|H_1, \sigma^2_{H_1})}{P(s|H_0, \sigma^2_{H_0})}. \tag{3.12}$$

Λ is just the ratio between the PDFs. The ratio Λ must be compared with a predefined threshold th. This threshold can be obtained by fixing the PFA and using the PDF for the H_0 hypothesis to find the threshold th which yields the required PFA. Once the likelihood ratio and the th are computed, the following comparison takes place. If Λ is bigger than a predefined threshold th, then decision D_1 is chosen, elsewhere if Λ is smaller or equal to th, then decision D_0 is chosen.

Assuming that the LRT parameters are known and that the PDFs of the observations under both hypotheses are known and follow normal distributions, then it can be shown [3, 9, 10] that the test function Λ can be obtained by implementing a replica-correlator. The replica-correlator constructs a decision statistic by correlating the input signal with a signal which tries to imitate the input signal as accurately as possible. An expression for the replica signal r is:

$$r = C(nT_s - \zeta T_{chip})e^{jw_d nT_s} \tag{3.13}$$

Nevertheless, the variances for the PDFs of the H_0, H_1 hypotheses are actually unknown and the LRT ratio makes use of the variances, as the variances must be known in order to obtain the PDFs. To circumvent this problem, the so-called Generalized Likelihood Ratio Test (GLRT) is used instead. The usage of the GLRT implies that the best estimate for $[f_d, \zeta]$ is

$$[f_d, \zeta] = \text{argmax}|R_{sr}(f_d, \zeta)|^2 \tag{3.14}$$

Where $R_{sr}(f_d, \zeta)$ is the cross-correlation between the incoming signal and the signal replica for some specific f_d values

Therefore, the acquistion process can be summarized in the following manner:

1. First the detection metric based on the replica-correlator in Eq. 3.25 for all θ=[f_d,ζ] is calculated. [f_d,ζ] maximizing the decision statistic are chosen as the MLE.
2. The decision statistic is compared with th.

The calculation of th is performed using the Neyman-Pearson criterion which maximizes the detection probability for a fixed probability of false alarm [3]. An example of the cross-correlation function is presented in Fig. 3.3.

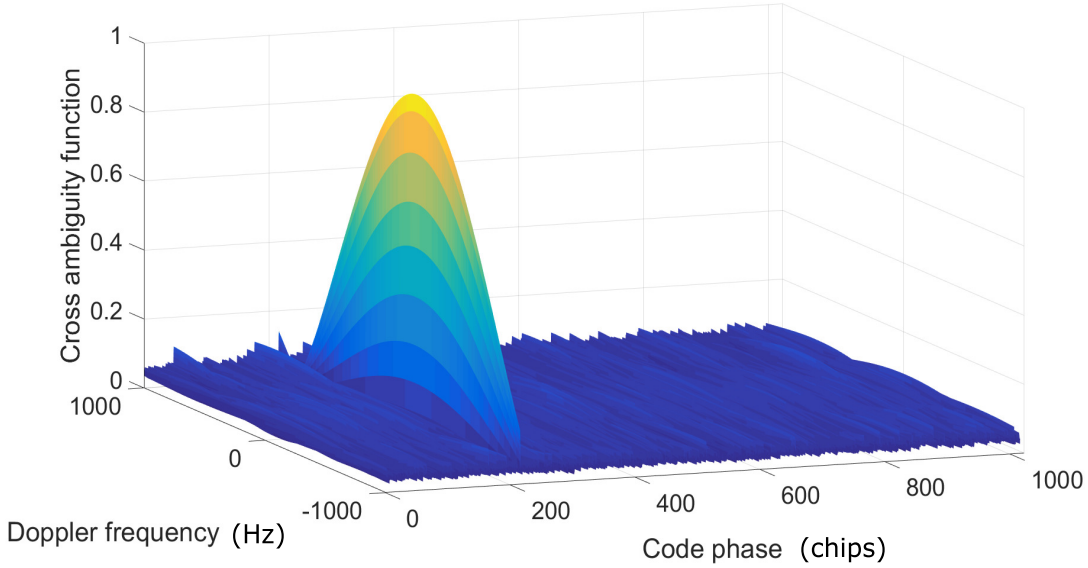

Figure 3.3: Cross-correlation representation.

3.4 Receiver types

3.4.1 Introduction

Depending on how the decision statistic is formed, different detector receiver architectures can be constructed. The objective of this chapter is to provide insight on the behaviour of the different receiver architectures regarding the GNSS LEO scenario. The baseline detector upon which others are constructed by applying some modifications in the decision statistic is the GLRT. However, a classification and discussion of the main detector architectures is shown in upcoming sections.

3.4.2 Coherent detector

3.4.2.1 Coherent detector basics

The coherent [9, 44] or MLE [9, 10] detector is the result of the direct application of the replica-correlator concept. As stated in [70], the coherent detector is not totally coherent because the phase of the input signal is unknown and a phase removal mechanism must be implemented before the detection test is carried out, otherwise the signal cannot be detected. The block diagram representing a possible implementation of this receiver is shown in Fig. 3.4.

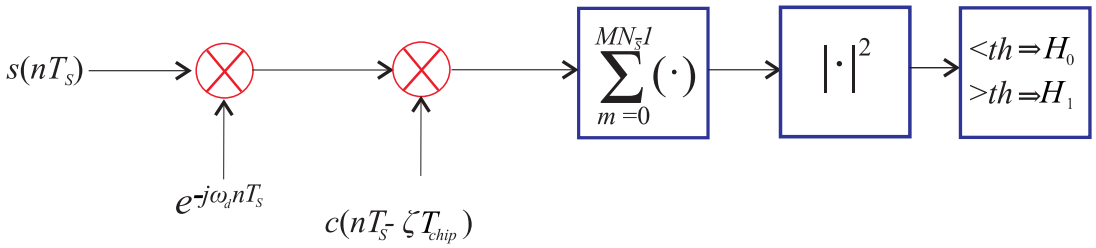

Figure 3.4: Coherent detector.

Note that th is the threshold defined in section 3.3. When considering the C/A L1 signal for an input signal of MN_s samples (being M the number of C/A codes being processed and N_s the number of samples per C/A block), the blocks of the coherent detector implement the following tasks:

1. Multiplication of the incoming signal by the Doppler frequency estimation (the more frequency search bins, the more multiplications).
2. Multiply by each possible code shift and accumulate (in fact this is a correlation).
3. Square the correlation result obtaining a matrix $R_{sr}(f_d, \zeta)$ with the correlation value for every $[f_d,\zeta]$ pair.
4. Determine if the maximum correlation result (decision statistic) exceeds a pre-defined threshold. If so, it is possible to conclude that the signal is present and the phase and Doppler of the input signal are the phase and Doppler that maximize the cross-correlation function.

For a specific noise level and pre-defined threshold (whose level is fixed by the Probability of False Alarm (PFA)), the maximization of the correlation maximizes the Probability of Detection (PD). Therefore, in order to study the receiver performance and appropriateness in a specific scenario, first, the degradation sources affecting the receiver performance must be identified and the degradation effect on the correlation must be quantified. Once the possible impairment sources are characterized, the way in which the receiver dynamics affect the received signal must be correctly modelled. The diagram in Fig. 3.5 illustrates this working scheme.

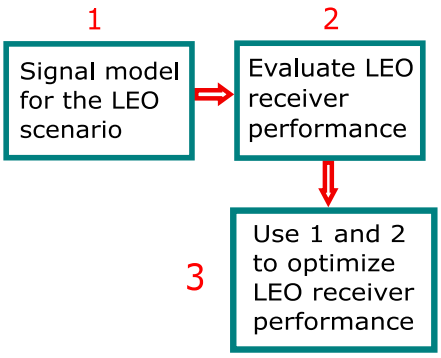

Figure 3.5: Work scheme

3.4.2.2 Coherent detector performance

Taking into consideration that the received signal is composed of the sum of a deterministic signal and a non-deterministic signal, the receiver must be must be characterized under both perspectives. Under the H_0 hypothesis, the decision statistic follows a central chi-squared distribution [9,75] (bear in mind the decision statistic is formed by adding the squares of two Gaussian distributions [76], which results in a chi-squared distribution). Under the H_1 hypothesis, the decision statistic follows a non-central chi-squared distribution whose mean depends on the receiver impairments. The magnitude of the effects are quantified by analyzing just the deterministic part of the detector. First, the effects affecting the deterministic signal component are analyzed. These effects are:

1. Doppler frequency.
2. Code phase estimation error.
3. Data modulation.

3.4.2.3 Doppler frequency attenuation

In order to study the effect of the Doppler frequency, it is necessary to compute the so-called cross-ambiguity function [44, 77] (in the absence of noise, data modulation and neglecting the carrier phase) which is described in Eq. 3.15.

$$M_{xcorr}(f_d, \zeta T_{chip}) = \left(\frac{1}{MN_s}\right) \cdot \sum_{n=0}^{MN_s-1} s(nT_s)\dot{C}(nT_s - \hat{\zeta}T_{chip})e^{-j2\pi\hat{f}_d nT_s}, \tag{3.15}$$

Which can be computed as (assuming the code phase estimate is correct [50]),

$$M_{xcorr}(f_d, \zeta T_{chip}) = \sqrt{P(nTs)} \cdot \sum_{n=0}^{MN_s-1} C(nT_s - \zeta T_{chip}) C(nT_s - \hat{\zeta} T_{chip}) \cdot \\ \cdot \left(\frac{1}{MN_s}\right) \cdot \sum_{n=0}^{MN_s-1} e^{j2\pi \Delta f_d n T_s}, \tag{3.16}$$

being $\Delta f_d = f_d - \hat{f}_d$ the Doppler frequency estimation error. The first sum is in fact the correlation between the received signal code and the replica code (which will be referred to as R) and $\Delta\tau = \zeta T_{chip} - \hat{\zeta} T_{chip}$ is the code estimation error.

$$\nu = \sqrt{P(nTs)} R(\Delta\tau) \tag{3.17}$$

$$M_{xcorr}(f_d, \zeta T_{chip}) = \nu \cdot \left(\frac{1}{MN_s}\right) \cdot \sum_{n=0}^{MN_s-1} e^{j2\pi \Delta f_d n T_s} = \nu \cdot \left(\frac{1}{MN_s}\right) \cdot \frac{1 - e^{j2\pi \Delta f_d T_s MN_s}}{1 - e^{j2\pi \Delta f_d T_s}}, \tag{3.18}$$

which can be rearranged as,

$$M_{xcorr}(f_d, \zeta T_{chip}) = \nu \cdot \left(\frac{1}{MN_s}\right) \cdot \\ \cdot \frac{e^{j\pi \Delta f_d T_s MN_s} e^{-j\pi \Delta f_d T_s MN_s} - e^{j\pi \Delta f_d T_s MN_s} e^{j\pi \Delta f_d T_s MN_s}}{e^{j\pi \Delta f_d T_s} e^{-j\pi \Delta f_d T_s} - e^{j\pi \Delta f_d T_s} e^{j\pi \Delta f_d T_s}}. \tag{3.19}$$

Further rearranging to express the numerator and denominator in terms of a sin function as shown in Eq. 3.20,

$$M_{xcorr}(f_d, \zeta T_{chip}) = \nu \cdot \left(\frac{1}{MN_s}\right) \cdot e^{j\pi \Delta f_d T_s (MN_s - 1)} \cdot \frac{\frac{e^{j\pi \Delta f_d T_s MN_s} - e^{-j\pi \Delta f_d T_s MN_s}}{2j}}{\frac{e^{j\pi \Delta f_d T_s} - e^{-j\pi \Delta f_d T_s}}{2j}}. \tag{3.20}$$

Finally, we obtain that the expression for the signal before entering the modulus operation

can be expressed as:

$$M_{xcorr}(f_d, \zeta T_{chip}) = \sqrt{P(nT_s)} \cdot R(\Delta\tau) \cdot e^{j\pi\Delta f_d T_s(MN_s-1)}. \\ \cdot \left(\frac{1}{MN_s}\right) \cdot \frac{\sin(\pi MN_s\Delta f_d T_s)}{\sin(\pi\Delta f_d T_s)}. \tag{3.21}$$

Now the value for $\pi\Delta f_d$ must be examined in order to further simplify Eq. 3.21. A typical value for Δf_d is 500 Hz. In this case $\pi\Delta f_d T_s = 0.007692$ and $\sin(\pi\Delta f_d T_s) = 0.0076961$. Then it follows that $\sin(\pi\Delta f_d T_s)$ can be approximated by $\pi\Delta f_d T_s$. Accordingly,

$$M_{xcorr}(f_d, \zeta T_{chip}) = \sqrt{P(nT_s)} \cdot R(\Delta\tau) \cdot e^{j\pi\Delta f_d T_s MN_s-1} \cdot \frac{\sin(\pi MN_s\Delta f_d T_s)}{MN_s\pi\Delta f_d T_s} \tag{3.22}$$

$$M_{xcorr}(f_d, \zeta T_{chip}) = \sqrt{P(nT_s)} \cdot R(\Delta\tau) \cdot e^{j\pi\Delta f_d T_s MN_s-1} \cdot \mathrm{sinc}(\pi MN_s\Delta f_d T_s) \tag{3.23}$$

the above expression after the square modulus operation yields the result shown in Eq 3.12. Bear in mind here, that the modulus operation acts as a phase removal mechanism and this is why this detector is not a pure coherent detector. Here the sinc function is defined as: $\mathrm{sinc} = \frac{\sin(x)}{x}$.

$$M_{xcorr}(f_d, \zeta T_{chip}) = P(nT_s)R(\Delta\tau)^2\mathrm{sinc}^2(\pi MN_s\Delta f_d T_s) \tag{3.24}$$

$$At_{doppler}(f_d) = \mathrm{sinc}^2(\pi MN_s\Delta f_d T_s) \tag{3.25}$$

For the case in which $N_s = 2041$ and $T_s = \frac{1}{2.041\times10^6}$ s and the Doppler search space spans from -50 kHz to 50 kHz (Doppler frequency search space for GNSS LEO scenarios if no frequency compensation is applied) the expression in Eq. 3.25 is plotted in Fig. 3.6 considering different coherent integration times (if M=2 a 2 ms coherent integration time is considered, if M=10 a 10 ms coherent integration time is considered). The graph highlights that frequency compensation is compulsory as the attenuation is larger than 13 dB for any coherent integration time if absolute frequency error is larger than 1 kHz.

If the error is bounded to frequency errors spanning from -2 kHz to 2 kHz, the Doppler attenuation graph is as shown in Fig. 3.7.

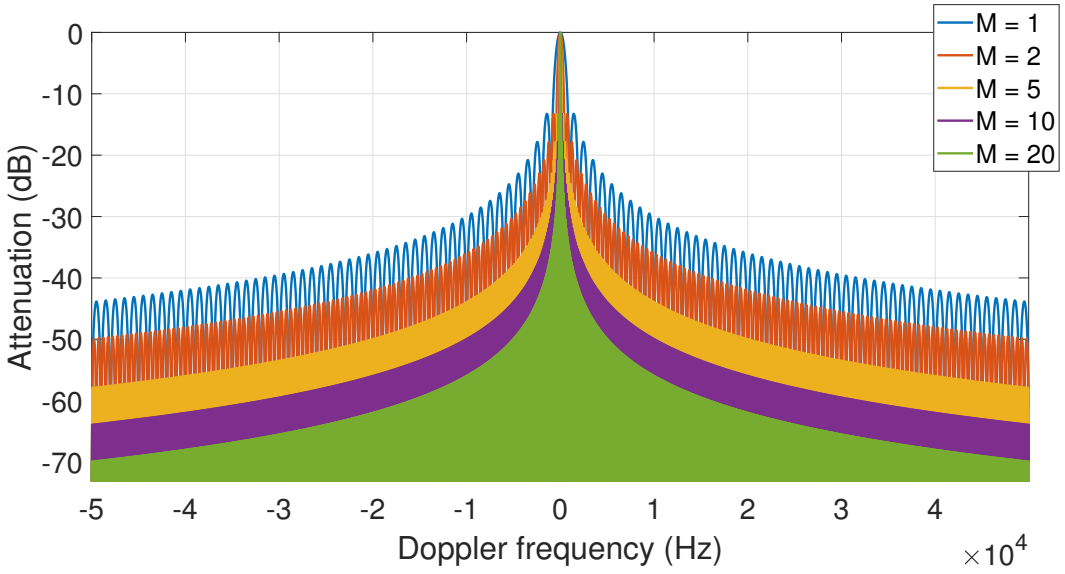

Figure 3.6: Attenuation in full Doppler domain.

From Fig. 3.6, it is possible to infer that as the coherent integration time increases so does the sensitivity to the Doppler frequency estimation error. This means that in order to a keep constant attenuation factor, the Doppler error estimation must decrease as the integration time increases. For instance, in order to obtain an attenuation factor of 0.4, the Doppler estimation error must be 500 Hz. However if $M = 2$, the Doppler estimation error must be 300 Hz instead of 500 Hz. Hence, as the coherent integration time increases, so does the computational cost because the Doppler estimation error is reduced by performing a finer Doppler search which has to be implemented by using a smaller Doppler frequency bin. For example, if the GNSS LEO scenario Doppler frequency search space is considered and $M = 2$, in order to limit the attenuation to 0.8751, the Doppler estimation error must be 100 Hz. Therefore, the Doppler search bin must be 200 Hz. Accordingly, $\frac{100000}{200} = 5000$ frequency bins must be searched. If $M = 10$, then the sensitivity to the Doppler frequency increases even more and a Doppler search bin of 20 Hz is necessary to limit the attenuation to 0.8751. Therefore, 10 times more bins will be needed with respect to the case in which $M = 2$.

In Fig. 3.8, the relation between the number of frequency of bins to be explored and M for different attenuation factors (0.9, 0.7,0.5 and 0.25), is shown. A different plot for each attenuation factor under study is provided.

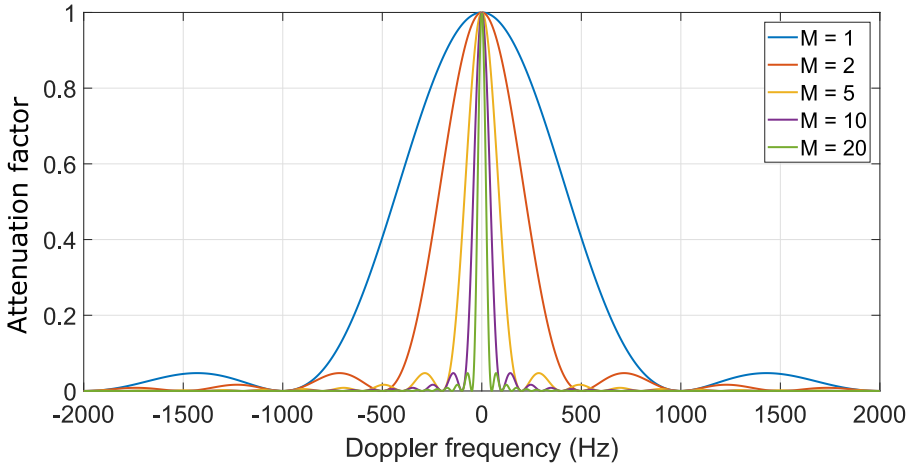

Figure 3.7: Attenuation in reduced Doppler domain.

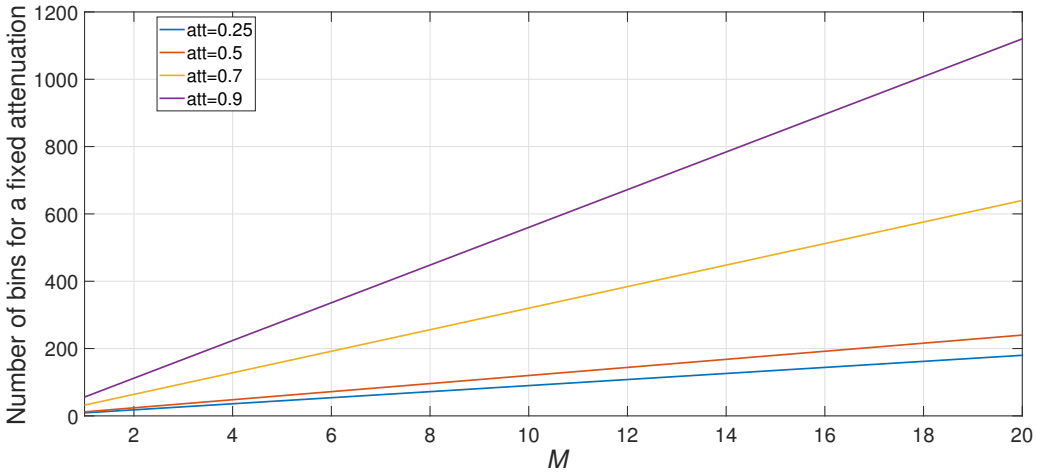

Figure 3.8: Doppler frequency bins to be explored vs M.

The graph in Fig. 3.8 can be used to aid the receiver design process, because for a target attenuation level, the number of frequency bins and the value for M can be obtained. For instance, to obtain an attenuation factor of 0.9, $M = 10$ and circa 600 bins must be explored, whereas for $M = 1$, less than 100 bins must be searched to yield a 0.9 attenuation factor. Therefore, it is clear that as M increases, so does the number of bins to limit the attenuation. Therefore, the increase in computational cost when increasing M is two-fold because to keep the attenuation level it is necessary to increase the number of bins searched. Hence, the increase in computational cost linked to the increase leads to an additional computational cost increase caused by the additional Doppler attenuation which has to be accounted for by increasing the number of searched bins.

A final remark is that the Doppler rate may have an impact on some receiver algorithms (see from Fig 3.7, that for a coherent integration time of 20 ms, a 25 Hz error in the Doppler estimation leads to a 0.4 attenuation factor). However, for the LEO case-study the maximum code rate is 75 Hz/s [70] and the maximum integration time considered in this work is 20 ms. Accordingly, the maximum Doppler frequency drift within an integration interval is 1.5 Hz. Therefore, for this case-study, the effect could be considered to be negligible.

3.4.2.4 Code phase estimation error

The correlation between the replica and the incoming code is the process in which the code replica is circularly shifted in order to replicate as accurately as possible the incoming code. Furthermore, both the input code and the replica code are sampled versions of these codes. Accordingly, if each code chip is not represented by a high number of samples, it is not possible to synchronize the code and the code replica exactly. In [9] this effect is named residual code phase offset or residual code phase error in [10]. This error is a residual error as it occurs when the maximum autocorrelation occurs, despite the fact a code shift between the replica and original code exists. The maximum code phase error is bounded by the number of samples per code period.

For example, if the code is sampled with two samples per code, then the maximum residual code phase error is 0.5 chips because the maximum code and code replica misalignment for this case is 0.5 chips.

$$\Delta\tau_{max} = \frac{L}{N_s}. \tag{3.26}$$

With L being the number of code chips and N_s the number of samples per code period. The correlation dependence with the code phase error is shown in Eq. 3.27.

$$R(\Delta\tau) = MN_s(1 - |\Delta\tau|). \tag{3.27}$$

Therefore the attenuation factor function modelling the code phase error attenuation can be expressed as shown in Eq. 3.28.

$$At_{codephase}(\Delta\tau) = (1 - |\Delta\tau|)^2. \tag{3.28}$$

Accordingly, the attenuation for different typical L1 C/A sampling frequencies can be obtained.

Table 3.1: Maximum code error attenuation

N_s	α_{code}
2046	0.250
4092	0.572
8192	0.766
16386	0.879
32772	0.9385

The results shown in Table 3.1 show that the error dependence with the sampling frequency is high. In view of the fact the maximum attenuation factor for $N_s = 32772$ is close to 0.94 it might advisable not to use sampling frequencies resulting in $N_s > 32772$ considering that if N_s is high then the computational cost in the signal processing is also high.

The theory above applies when no Doppler frequency error exists. Going back to Eq. 3.9, the incoming signal (in the absence of noise) is more correctly represented by the expression in Eq. 3.29 because the Doppler effect affects the code chip frequency and the received code chip frequency is not the same as the nominal chipping frequency. Nevertheless, the signal model does not take into account the noise and the data signal.

$$s(nTs) = \sqrt{P(nTs)}C((1+\eta)nT_s - \zeta T_{chip})e^{j(w_{L1}(1+\eta)nT_s+\theta_k)}, \tag{3.29}$$

with $w_{L1} = 2\pi \times f_{L1}$ and $\eta = \frac{f_d}{f_{L1}}$ (f_{L1} is the GPS L1 frequency) and $\eta = \frac{f_d}{f_{L1}}$.

η is the dilation coefficient modelling the relativistic time dilation coefficient.

After baseband conversion to a zero Intermediate Frequency (IF) expression in Eq. 3.30 is:

$$s(nTs) = \sqrt{P(nTs)}C((1+\eta)nT_s - \zeta T_{chip})e^{j(w_d nT_s+\theta_k)}. \tag{3.30}$$

Depending on the sign of the dilation coefficient, the received code chipping frequency might increase or decrease. Depending on the magnitude of this coefficient the chipping frequency will change more or less in a fixed time. Accordingly, the code phase changes with time and is a function of the dilation coefficient. In order to describe the code phase variation with time, an expression will be deduced. The initial phase is ζ_0 and recalling that the Doppler frequency is f_d.

The Doppler frequency drift affecting the code chipping frequency f_{dchip} is as shown

in Eq. 3.31,

$$f_{dchip} = f_{chip}\frac{f_d}{f_{L1}}. \tag{3.31}$$

The ratio between the carrier L1 frequency f_{L1} and the Doppler frequency f_d, is $\frac{f_d}{f_{L1}}$, so the Doppler drift affecting the chipping code must be the actual Doppler frequency f_d scaled by the above-mentioned scaling factor. The new chipping frequency $f_{chip'}$ is shown in Eq. 3.32,

$$f_{chip'} = f_{chip} + f_{dchip} = f_{chip} + f_{chip}\frac{f_d}{f_{L1}} = f_{chip}(1+\eta). \tag{3.32}$$

Now the question to answer is: How much does the code drift in a code chip period? In one code chip period, the phase drift will be $\frac{f_{dchip}}{f_{chip}}$, which is η. Therefore, η is actually the percentage drift between the nominal code and the Doppler affected code, i.e. the phase drift per code chip period.

Two considerations must be made before deducing the final expression.

1. In one chip the drift is η, in one second the drift is $\eta \times f_{chip}$ (f_{chip} chips in one second) which is $\frac{\eta}{T_{chip}}$.
2. If η<0, the drifted code phase increases with respect to the nominal code phase. Whereas if η>0, the drifted code phase decreases with respect to the nominal code phase.

Finally, the phase variation with time can be expressed as:

$$\zeta = \zeta_o - \eta\frac{t}{T_{chip}}. \tag{3.33}$$

Which is exactly the same expression as the one presented in [1, 9]. Using the expression in Eq. 3.33 one can calculate the phase drift in a coherent integration period as shown in Eq. 3.34:

$$\Delta\zeta = \zeta(LMT_{chip}) - \zeta(0) = -\eta ML. \tag{3.34}$$

If the replica code is generated taking into consideration the code drift and a code drift compensation mechanism is implemented via code chipping frequency correction (i.e.

generate the code using a corrected chipping frequency $C((1+\hat{\eta})nT_s - \hat{\zeta}T_{chip}))$, then the code phase drift can be expressed as in Eq. 3.35.

$$(\eta - \hat{\eta})ML \tag{3.35}$$

For a worst case Doppler frequency of 50 kHz and considering a 20 ms coherent integration time ($M = 20$ for the L1 C/A signal), then the maximum drift in chips is $\frac{LM\eta}{2}$=0.324675 chips.

In view of the above arguments an important point to take into consideration is that the code drift increases as the coherent integration time increases because the drift accumulates. This effect is shown in Fig. 3.9, for a C/A code represented with 20000 samples and a code drift corresponding to a 50 kHz Doppler. The top graph in Fig. 3.9 shows the first 400 samples in which the original and drifted codes appear to be identical. However, for the last 400 samples the effect of the drift is not negligible as represented in the bottom graph in Fig. 3.9.

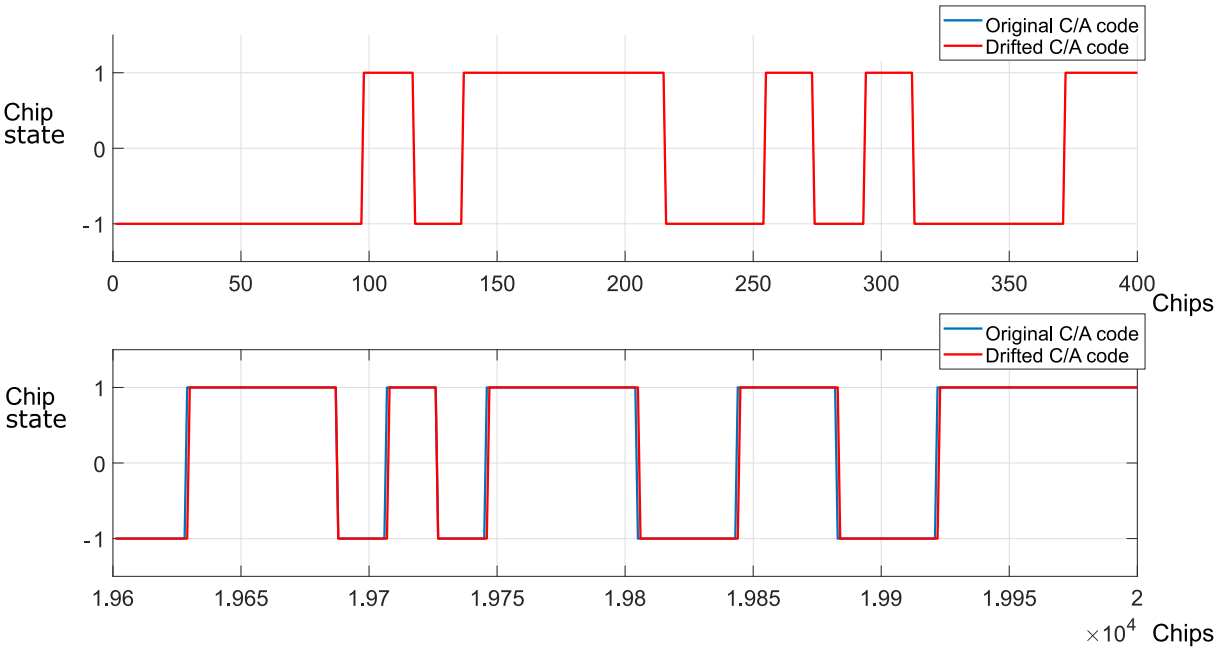

Figure 3.9: Code drift at the beginning and end of a C/A code.

Following the reasoning made by [9], when the integration time is small, a midpoint approximation can be used to describe the attenuation factor caused by the code drift. The equation should not work when dealing with long integration times. The midpoint

approximation can be expressed as in Eq. 3.36,

$$At_{cdmidpoint} = 1 - \left|(\zeta_0 - \hat{\zeta_0}) - \frac{\Delta\zeta}{2}\right|^2, \tag{3.36}$$

where $\hat{\zeta_0}$ is the estimate of the initial phase offset.

When taking into consideration a signal slice containing MN_s samples, the code drift increases linearly from the first sample ($n = 0$) to the last sample ($n = MN_s$), hence the code misalignment increases as the sample number under analysis increases. Accordingly, if $\Delta\zeta = \eta LM$ is the drift in chips after M code periods, then the expression describing the misalignment for sample n is shown in Eq. 3.37.

$$\text{Codedrift(n)} = \frac{\Delta\zeta}{MN_s} n \text{ chips.} \tag{3.37}$$

In order to deduce an expression to describe the attenuation caused by the code misalignment, it is necessary to take into consideration that the probability of chip transition is $P_{ct} = \frac{1}{2}$. Therefore, at the output of the correlator can be described as in Eq. 3.38,

$$\begin{aligned} Y_{corr} &= MN_s - \sum_{n=0}^{MN_s-1} P_{ct}\frac{\Delta\zeta}{MN_s} n = \\ &MN_s - \frac{P_{ct}}{MN_s} \cdot \frac{(MN_s)\cdot(MN_s-1)}{2} \approx \\ &MN_s\left(1 - \frac{|\Delta\zeta|}{4}\right). \end{aligned} \tag{3.38}$$

In Eq. 3.38, the approximation $MN_s - 1 \approx MN_s$ has taken place. The output of the decision statistic is described in Eq. 3.39,

$$\left(1 - \frac{|\Delta\zeta|}{4}\right)^2 (MN_s)^2. \tag{3.39}$$

In the case in which no Doppler or phase error happen, the output of the decision statistic is MN_s. Hence, by comparing MN_s with Eq. 3.39 it is possible to infer that the expression for the maximum attenuation caused by the code drift within a coherent integration

interval is provided in Eq. 3.40,

$$AtMax_{cd} = \left(1 - \frac{|\Delta\zeta|}{4}\right)^2. \tag{3.40}$$

A similar formula which takes into consideration the residual code drift along with the code drift caused by the Doppler effect is provided in [9] and reproduced in Eq. 3.41.

$$\alpha_{cd} = \begin{cases} \left(1 - \frac{|\Delta\zeta|}{4}\right)^2 \left(1 - \frac{|(\zeta_0 - \hat{\zeta_0}) + \frac{\Delta\zeta}{2}|}{1 + \frac{|\Delta\zeta|}{2}}\right)^2 & |(\zeta_0 - \hat{\zeta_0}) + \frac{\Delta\zeta}{2}| \leq 1 + \frac{\Delta\zeta}{2} \\ 0 & \text{otherwise} \end{cases} \tag{3.41}$$

Assuming the initial residual phase is zero ($\zeta_0 - \hat{\zeta_0} = 0$), the comparison etween Eq. 3.36 and Eq. 3.41 is shown in Fig. 3.10

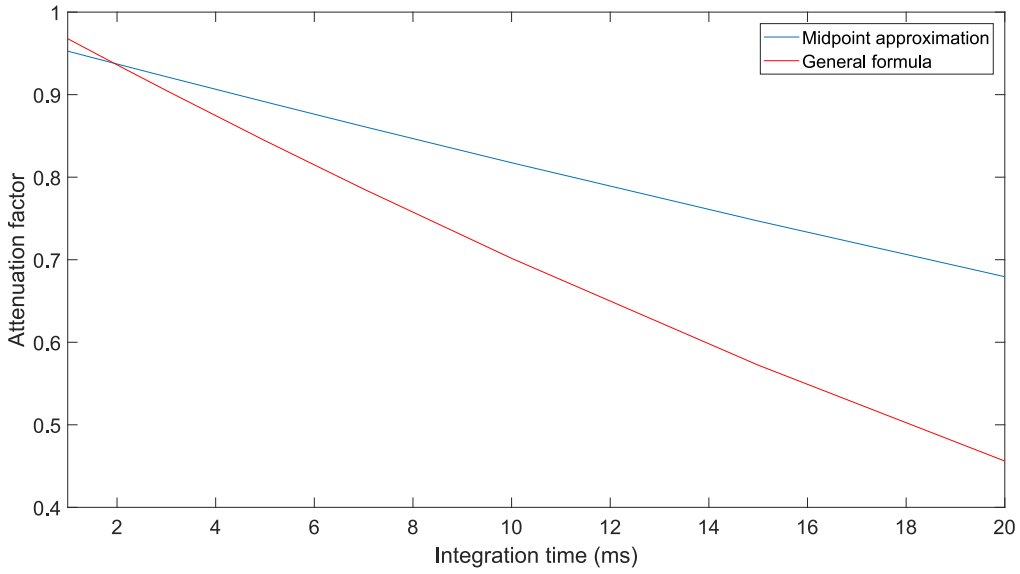

Figure 3.10: Comparison between Eq. 3.36 and Eq. 3.41 for a 50 kHz Doppler.

The two approaches described in Eq. 3.36 and Eq. 3.41 are now compared with Matlab simulations. Original C/A codes and drifted C/A codes are generated. Then the correlation between two original C/A codes and an original and a drifted C/A code are calculated. Finally, both correlation results are compared finding the correlation peak attenuation and drift. In this way the accuracy of Eq. 3.36 and Eq. 3.41 can be assessed. The results of the comparison are shown in Table 3.2.

Table 3.2: Attenuation formula comparison

M	Simulation	Eq. 3.36	Eq.3.41
1	0.9791	0.9838	0.9678
2	0.9594	0.9678	0.9361
5	0.9206	0.9205	0.8444
10	0.8436	0.8443	0.701
15	0.7705	0.7713	0.5722
20	0.7014	0.7017	0.4560

From Table 3.2, it can be inferred that the midpoint approximation tends to overestimate the attenuation caused by the code Doppler. Hence, this formula can be used to establish a conservative bound. Nevertheless, the simulation and Eq. 3.36 agree, so the latter equation will be used. Moreover, the theoretical and the measured code drift are compared in Table 3.3.

Table 3.3: Drift comparison

M	Theoretical drift (chips)	Measured drift (chips)
1	0.0162	0.0256
5	0.0812	0.0797
10	0.1623	0.1595
15	0.2435	0.2458
20	0.3247	0.3225

The simulated and theoretical drifts agree and the very slight differences observed can be explained by the fact the chip drifts have been calculated using an integer number of samples. Accordingly it is not possible to represent each and every possible phase value.

Moreover, different tests with synthetic and real data are performed in order to measure how well formulas Eq. 3.36 and Eq. 3.41 agree in measuring the attenuation caused by the Doppler code drift. First, using data from a LEO scenario using a GSS7700 Spirent signal simulator and sampled at a sampling frequency of 40 Msps, using an USRPX310 device. The attenuation is measured by comparing the correlation results with and without using Doppler code correction. Four different data types are analyzed. Two data sets coming from the Spirent simulators with -9 kHz and -30 kHz and two data sets consisting on synthetic Matlab C/A codes affected by a -9 kHz and a -30 kHz Doppler frequency, respectively. The results are displayed in Table 3.4 and Table 3.5.

The results show that the tests and the theoretical attenuation results predicted by Eq. 3.36 and Eq. 3.41 agree.

Table 3.4: Coherent detector attenuation for different M and -9 kHz Doppler.

M	Theoretical attenuation	Test data attenuation	Synthetic data attenuation
1	0.9971	1	0.9988
10	0.9713	0.9688	0.9710
20	0.9430	0.9547	0.9417

Table 3.5: Coherent detector attenuation for different M and -30 kHz Doppler.

M	Theoretical attenuation	Test data attenuation	Synthetic data attenuation
1	0.9902	1	0.9804
10	0.9045	0.9059	0.8985
20	0.8139	0.7888	0.8024

3.4.2.5 Data modulation

The data modulation effect makes reference to the possible data transition within an integration interval. Assuming the integration interval comprises MN_s samples, it follows that if a data transition occurs within the integration interval, the samples after the data transition will have a different sign than the data after the data transition. Therefore, depending on the point where the data transition sign happens, the magnitude of the data modulation attenuation is bigger or smaller. The situation is illustrated in Fig. 3.11. Depending on the value t (percentage of samples before the bit transition), the attenuation changes.

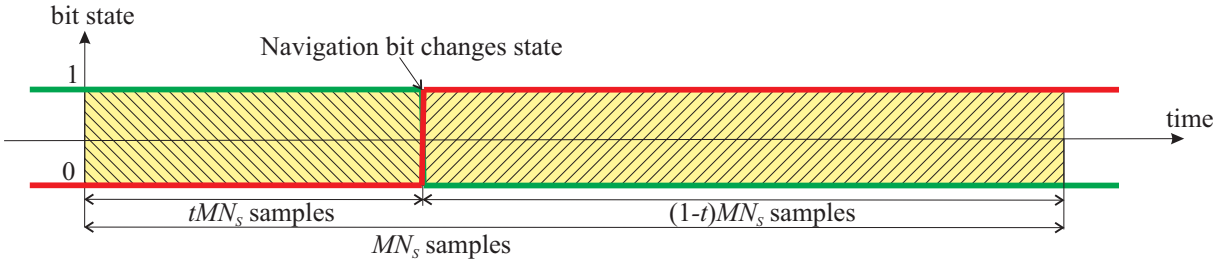

Figure 3.11: Transition within integration time.

When the Doppler frequency is correctly estimated ($w_d - \hat{w}_d = 0$) (where $\hat{w}_d$ is the Doppler angular frequency estimation), analyzing the case in which the value of t is 0.5, then the correlation result is zero. Analytically, the absolute value of the correlator result (if a data change happens) can be expressed as:

$$\left| \sqrt{P(nTs)} e^{j\theta_k} \left(\pm \sum_{n=0}^{tMN_s} 1 \mp \sum_{n=0}^{(1-t)MN_s} 1 \right) \right| = MN_s P(nTs)(1-2t). \tag{3.42}$$

Hence, the expression for the attenuation caused by the data modulation can be expressed as:

$$At_{dm} = (1 - 2t)^2. \tag{3.43}$$

The mean attenuation factor for the case in which a navigation bit change appears (assuming t follows a uniform distribution) can be described as shown in Eq. 3.44,

$$\overline{\alpha_{dm}} = \int_0^1 (1 - 2t)^2 dt = \frac{1}{3}. \tag{3.44}$$

However, when analyzing a time interval, the occurrence of a data bit change is unknown. Therefore, the mean attenuation factor must also include the weighted probability of the navigation data bit not changing. This behaviour is modelled in Eq. 3.45.

$$\overline{At_{datamod}} = P_{dm}\overline{\alpha_{dm}} + P_{ndm}\overline{\alpha_{ndm}}. \tag{3.45}$$

Where P_{dm} and P_{ndm} are the probabilities of data modulation occurrence and the probability of no data modulation occurrence respectively. $\overline{\alpha_{ndm}}$, is one because the attenuation factor is one when there is no data modulation. T_{bit} is defined as the inverse of the data bit rate. $P_{dm} = \frac{MN_sT_s}{2T_{bit}}$ and $P_{ndm} = 1 - \frac{MN_sT_s}{2T_{bit}}$.

Finally, the mean attenuation coefficient can be expressed as in shown in Eq. 3.46,

$$\overline{At_{datamod}} = 1 - \frac{MN_sT_s}{3T_{bit}}. \tag{3.46}$$

Beware of the fact that, for this analysis, it is assumed that the maximum integration time is T_{bit}, so the attenuation decreases as the coherent integration time increases. The above expressions are based on the simplified hypothesis that assumes $w_d - \hat{w_d} = 0$. When $w_d - \hat{w_d} \neq 0$ Eq.3.42 transforms into:

$$\sum_{n=0}^{tMN_s} e^{jnT_s(w_d - \hat{w_d})} - \sum_{n=0}^{(1-t)MN_s} e^{jnT_s(w_d - \hat{w_d})}. \tag{3.47}$$

The expressions for the mean and worst case attenuation deduced in [9], are reproduced.

The mean case attenuation expression is described by means of Eq.3.48.

$$\overline{At_{datamodDoppler}} \approx 1 - \left(\frac{M}{T_{bit}}\right)\left(\frac{2\cot\left(\frac{(w_d-\hat{w_d})MN_s}{2}\right)}{\frac{(w_d-\hat{w_d})MN_s}{2}} - \cot^2\left(\frac{(w_d-\hat{w_d})MN_s}{2}\right)\right). \quad (3.48)$$

The worst case attenuation expression is described by means of Eq.3.49.

$$At_{datamodDopplerwc} \approx 1 - \frac{4\cos\left(\frac{(w_d-\hat{w_d})MN_s}{2}\right)\sin^2\left(\frac{(w_d-\hat{w_d})MN_s}{4}\right)}{\sin^2\left(\frac{(w_d-\hat{w_d})MN_s}{2}\right)}. \quad (3.49)$$

Eq. 3.48 tends to yield the same results as Eq. 3.46 as $(w_d - \hat{w_d})$ approaches zero. As shown in [9], for the worst case, the energy of the main lobe is divided to form two side lobes. Therefore, an estimation bias appears.

3.4.2.6 Statistical characterization

It is well known that the GNSS signal is composed of the sum of a deterministic component (the signal transmitted by the satellite) and a noise component. In order to perform a statistical analysis of such a signal, two different situations must be considered. First, the analysis should be performed in the case the receiver is trying to search a signal which is actually not present (H_0) and finally the case in which the deterministic component is present (H_1 hypothesis).
According to [9, 10, 44, 75, 78], for the H_0 hypothesis the output signal follows a central chi-squared distribution with two degrees of freedom. This model relies on the fact the decision statistic is formed by the sum of the squares of two independent normal variables (both quadrature and in-phase components follow a normal distribution in accordance the circularly symmetric noise model). The input noise variance is σ^2, but at the correlator output the variance is $\sigma^2_{corr} = MN_s\sigma^2$. In order to construct the detection statistic, a detection threshold th must be established. If the detection statistic value exceeds the detection threshold, the GNSS signal is declared to be present. Otherwise, the signal is not present. The Probability of False Alarm (PFA) is defined as the definite integral between th and ∞ of the probability distribution under H_0. For this specific case, the PFA can be expressed as in Eq. 3.50.

$$PFA = \exp\left(\frac{-th}{2\sigma^2_{corr}}\right) \quad (3.50)$$

When the signal is present (H_1 hypothesis), the correlator output result follows a non-central chi-squared distribution (the circularly symmetric zero-mean distribution transforms into the same distribution with a non-zero mean whose mean (λ) is given by Eq. 3.23). Accordingly, the Probability of Detection (PD) can be expressed as in Eq. 3.51.

$$PD = Q\left(\frac{\sqrt{\lambda}}{\sigma^2_{corr}}, \frac{\sqrt{th}}{\sigma^2_{corr}}\right) \tag{3.51}$$

where Q is the Marcuum function as defined in [79].

Therefore, the Receiver Operation Curve (ROC) (plot of PFA vs PD for a fixed Carrier to Noise Ratio) can be obtained by considering a specific detector threshold th. Speaking in practical terms, the variance σ^2_{corr} can be estimated by measuring the variance of the result of the correlation of the input signal with a PRN code which is not present in the received signal.

3.4.2.7 Conclusions

In view of the above-mentioned points, we can conclude that the coherent detector is seriously hindered by the following factors:

1. As the integration time increases, so does the receiver sensitivity to the residual Doppler frequency error. Hence, as the number of periods coherently combined increases, so does the sensitivity to Doppler frequency and the gain due to an extended integration time can be counteracted by the attenuation caused by the input Doppler frequency. In order to circumvent this problem it is necessary to perform a very fine Doppler search which implies a computational cost increase. Therefore, in scenarios in which it is necessary to increase acquisition sensitivity using an extended integration time, the computational cost increase is two-fold.

2. This detector type is very sensitive to code Doppler. This effect is larger as the integration time increases and as the Doppler effect increases. Therefore, the integration time cannot be increased at will, without facing an attenuation caused by the code Doppler. It has been demonstrated that in order to ignore this effect, the coherent integration time must be limited to 1 ms because in this case the attenuation can be bounded to a 1% attenuation for a 30 kHz input Doppler. Accordingly, if the coherent integration time is limited to 1 ms, the code Doppler is negligible. However, as the integration time increases, the effect is no longer negligible and code correction is compulsory if no attenuation is affordable.

3. The detector is very sensitive to the data modulation effect. When a data change occurs in the middle of the integration time, the correlation cancels out. Therefore, integration times below 10 ms or the usage of methods which deal with this effect such as the "half-bit method" [80](takes two consecutive 10 ms signals knowing that the there will be no data change in one of the two 10 ms signals) are compulsory. Furthermore, the data modulation effect is not independent of the input Doppler frequency and the fact the energy of the main lobe is divided leads to an estimation bias. Accordingly, this feature must be taken into consideration when designing a receiver.

4. The detector is sensitive to phase variability and a fine synchronization is required.

3.4.3 Non-coherent detector

The non-coherent detector works by operating over coherent integration intervals, which are generally smaller than T_{bit}. The correlation outputs for each coherent integration interval are squared and added together. This process is known as non-coherent integration. The motivation for the implementation of such procedures is that the small coherent integration helps in mitigating the correlation cancellation caused by data bit reversal. However, this detector type suffers from the so-called squaring loss. The term squaring loss refers to the variation in Signal to Noise Ratio (SNR) by going from coherent integration to non-coherent integration [81]. The block diagram of this detector type is shown in Fig. 3.12.

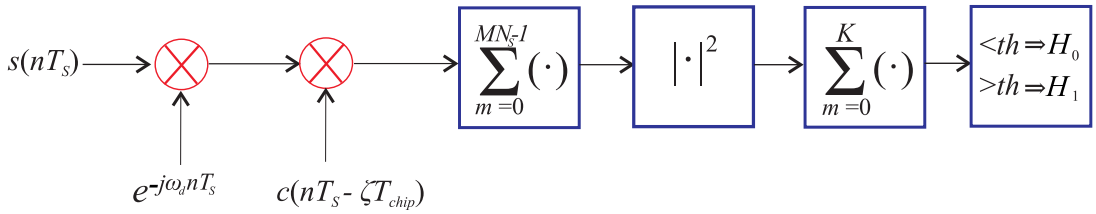

Figure 3.12: Non-coherent detector.

3.4.3.1 Non-coherent detector performance

An analogous analysis to the one performed for the coherent detector is to be performed. Again, the magnitude of the effects is quantified by analyzing just the deterministic part of the detector. Therefore, the deterministic part of the signal is affected by the following effects that cause impairments.

1. Doppler frequency.

2. Code phase estimation error.

3. Data modulation.

3.4.3.2 Doppler frequency

The attenuation caused by the input Doppler frequency is exactly the same as the Doppler attenuation for the coherent detector. Accordingly, Eq. 3.25 can be used to model the Doppler frequency attenuation for the non-coherent detector. However, it must be noted that taking into consideration that the non-coherent detector accumulates the correlation results coming from independent coherent correlations it is possible to minimize M in order to minimize the sensitivity to Doppler frequency and increase the number of non-coherent integrations K. In this way, the same number of samples can be processed at the same time is that in a coherent detector without suffering a bigger Doppler attenuation. For example, for a 22 Hz Doppler error and if $M = 20$, the attenuation factor for the coherent detector is 0.5. On the other hand, for a non-coherent detector with $M = 1$ and $K = 20$ (same number of samples processed than in the coherent detector), an attenuation of 0.5 is achieved with a 440 Hz Doppler estimation error. This reasoning illustrates how the non-coherent detector outperforms the coherent detector when dealing with Doppler frequency impairments.

3.4.3.3 Code phase estimation error

By resorting to a similar argument to the one used in the above section, it is possible to infer that the magnitude of the attenuation caused by the code drift is the attenuation in the coherent integration interval.

Following exactly the same procedure as in section 3.4.2.4, different tests with synthetic and real data are performed in order to measure how well the formulas Eq. 3.36 and Eq. 3.41 agree in measuring the attenuation caused by the Doppler code drift (when $M = 1$). First, using data from a LEO scenario using a GSS7700 Spirent signal simulator and sampled at a sample frequency of 40 Msps, using an USRPX310 device. The attenuation is measured by comparing the correlation results with and without using Doppler code correction. Four different data types are analyzed. Two data sets coming from the Spirent simulator with -9 kHz and -30 kHz and two data sets consisting on C/A codes (Matlab synthetic) affected by -9 kHz and -30 kHz Doppler. The results are displayed in Table 3.6 and Table 3.7.

From the results above it appears that:

1. The theoretical, test and synthetic results agree. Therefore, the procedures are validated.

Table 3.6: Non-coherent detector attenuation for different K and -9 kHz Doppler

K	Theoretical	Test data (Spirent)	Synthetic data (Matlab)
1	0.9971	1	0.9986
10	0.9684	0.9688	0.9710
20	0.9306	0.9547	0.9423

Table 3.7: Non-coherent detector attenuation for different K and -30 kHz Doppler

K	Theoretical	Test data (Spirent)	Synthetic data (Matlab)
1	0.9902	1	0.9804
10	0.9045	0.9059	0.8985
20	0.8139	0.7888	0.8024

2. The coherent and the non-coherent detector behave quite similarly when dealing with the code Doppler effect.

3.4.3.4 Data modulation

Considering a qualitative argument, it is possible to infer that the immunity to data modulation of the non-coherent detector is greater than the immunity to data modulation of the coherent detector. For instance, if $M = 20$ for a coherent detector or $K = 20$ and $M = 1$ for a non-coherent detector, then the same number of samples is processed. A data modulation transition can occur at any point of the coherent or the non-coherent integrations. However, if the transition occurs in the middle of the coherent integration period, the correlation is completely destroyed, whereas for the non-coherent case, just one of the 20 coherent integrations is affected so the maximum attenuation is $\frac{19}{20}$. This is the major advantage of the non-coherent detector with respect to the coherent detector. After this introduction, quantitative arguments comparing both detectors will be provided.

Lets recall that the non-coherent detector relies on K independent coherent correlations. In Fig. 3.13 the non-coherent detector managing of the input samples is shown. Each coherent integration interval consists in MN_s samples and K coherent integration intervals are processed independently and non-coherently combined.

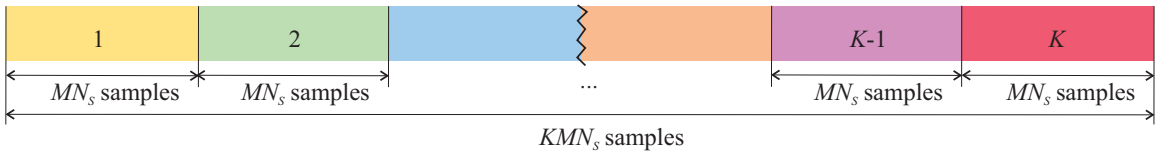

Figure 3.13: Non-coherent detector input samples scheme.

For the high-dynamics scenario under study the maximum integration time T_{maxint} will be restricted to the data bit period (T_{bit}) (i.e. for the GPS L1 C/A signal $T_{maxint} = 20\ ms$). Under these conditions, it is possible to express the data modulation attenuation for the non-coherent as a function of the data modulation attenuation for the coherent detector. The data modulation attenuation for the non-coherent detector can be expressed as in Eq. 3.52.

$$At_{dmno-cohDoppler} = 1 - \frac{M}{K}\left(1 - At_{datamodDoppler}\right). \tag{3.52}$$

For the case in which no Doppler frequency residual error exists, Eq. 3.52 transforms into Eq. 3.53.

$$At_{dmnon-coh} = 1 - \frac{M}{K}\left(1 - |1 - 2t|^2\right). \tag{3.53}$$

In the case in which Doppler frequency residual error exists, then the expression for the mean data modulation attenuation for a non-coherent detector mean attenuation can be expressed as shown in Eq. 3.54.

$$At_{dmno-cohDoppler} = 1 - \frac{M}{K}\left(1 - \left|1 - 2\exp\left(-j\frac{(w_d - \hat{w_d})MN_s}{2}\right)\frac{\sin\left(\frac{(w_d-\hat{w_d})MN_s t}{2}\right)}{\sin\left(\frac{(w_d-\hat{w_d})MN_s}{2}\right)}\right|^2\right). \tag{3.54}$$

3.4.3.5 Statistical characterization

The non-coherent combining process consists in summing K instances of the coherent detector output. Under the H_0 hypothesis and speaking in statistical terms, this translates into the sum of K central independent chi-squared with two degrees of freedom distributions. Therefore, the resulting distribution is a central chi-squared distribution with $2K$ degrees of freedom.

3.4.4 Differentially coherent detector

The differentially coherent (Post-correlation differential detector according to [10]) detector works upon a similar principle to the non-coherent detector, as K independent coherent correlations for K different signal segments are computed. However, the decision statistic is formed by multiplying the coherent correlation at time epoch m with the conjugated correlation at time epoch $m - J$, instead of taking just the modulus of the coherent correlation. The delay between the first sample used to calculate the correlation for time epoch m and the first sample for the correlation corresponding to time instant $m - J$, is JMN_s. Therefore, J represents the number of coherent integrations between the first and the second time epoch which are differentially coherently combined. Once the decision statistic is formed, K results of the product between the coherent correlation at time epoch m and the conjugated correlation at time epoch $m - J$ are non-coherently combined. The signal correlation between the two subsequent correlations is very high, but the the white noise components are independent. The procedure is illustrated in Fig. 3.14. By using this procedure it is possible to retain the non-coherent detector immunity to Doppler errors and circumvent the squaring loss problem. The non-coherent detector squaring loss appears because the noise samples are squared, whereas the differential detector forms the detector statistic multiplying independent noises. Therefore, the noise power of the differential detector is less than the resulting noise power of the non-coherent integration [43].

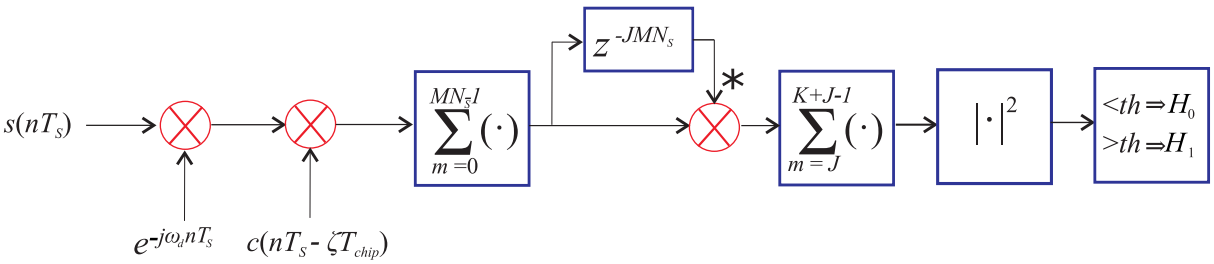

Figure 3.14: Differentially coherent detector.

3.4.4.1 Differentially coherent detector performance

An analogous analysis to the one performed for the coherent and non-coherent detectors is to be performed. Again, the magnitude of the effects are quantified by analyzing just the deterministic part of the detector. Therefore, the deterministic part of the signal is affected by the following non-idealities which can cause impairments.

1. Doppler frequency.
2. Code phase estimation error.

3. Data modulation.

3.4.4.2 Doppler frequency

According to [9] and [10], the behaviour of this detector with Doppler frequency takes the expression of the square of the attenuation for the non-coherent detector. The mathematical description is provided at Eq.3.55.

$$At_{DiffDoppler}(f_d) = \text{sinc}^4(\pi M N_s \Delta f_d T_s) \tag{3.55}$$

Note here that, as stated and demonstrated in [9], it is necessary to take the modulus of the correlation operation as an extra frequency loss would be induced elsewhere. The reason for this, is that the result of the differential product depends on an exponential term $\exp\left(\left(\frac{j(w_d - \hat{w_d})MN_s}{2}\right)(JMN_s)\right)$. In order to circumvent this problem it is compulsory to take the square modulus after the correlation operation. The incoming Doppler frequency can be safely assumed to be constant within the integration time, despite the fact in this work a high dynamics scenario is considered. According to [70], the Doppler rate is 75 Hz/s. Therefore, for a 20 ms integration time the change in Doppler frequency is $\frac{75\times 20}{1000} = 1.5$ Hz. This amount is neglible for this analysis.

3.4.4.3 Code phase estimation error

In [9], it is stated that the non-coherent detector and the Differentially coherent detector behave similarly under the influence of code Doppler in the case in which $\Delta\zeta$ is not too large. However, in the case under study in this work, the assumption $\Delta\zeta$ is small may not be correct.

By taking into account the detector working principle, it is possible to infer that the decision statistic for this detector is formed by combining two different terms R_m and R_{m-J} which are the coherent correlations results for time epochs m and $m-J$ respectively. The terms R_m and R_{m-J} are maximized when there is a chip separation of $|J\Delta\zeta|$, therefore the maximum value of the product of the two terms appears at $-J\frac{\Delta\zeta}{2}$ and $J\frac{\Delta\zeta}{2}$ from the maximum value of R_m and R_{m-J}, respectively. This reasoning is illustrated in Fig. 3.15.

From the discussion it is possible to infer that this detector type incurs in an extra attenuation with respect to the non-coherent detector. This extra attenuation term can

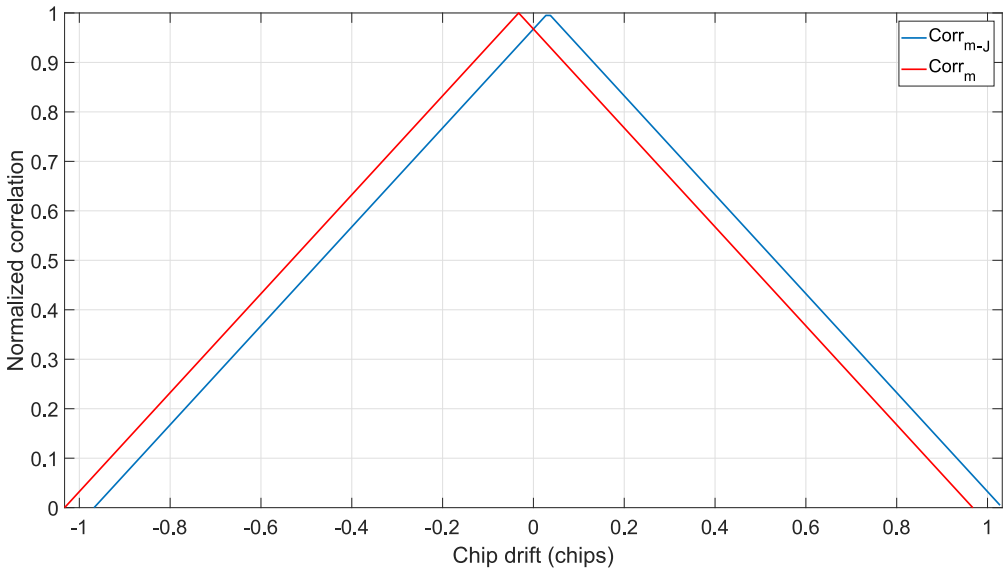

Figure 3.15: Differentially coherent detector terms drift.

be quantified after the product as expressed in Eq. 3.56.

$$At_{extraterm} = \left(1 - \left|\frac{J\Delta\zeta}{2}\right|\right)^2. \tag{3.56}$$

Both R_m and R_{m-J} incur in a $\left(1 - |\frac{J\Delta\zeta}{2}|\right)$ attenuation.

After the differential product is formed, the signal is squared, so finally, the attenuation caused by this detector type when dealing with the code Doppler effect, can be expressed as in Eq.3.57.

$$At_{diffcd} = \left(1 - \left|\frac{J\Delta\zeta}{2}\right|\right)^4. \tag{3.57}$$

For a worst case Doppler frequency of 50 kHz, the values for the extra attenuation for $J = 1$ and different values for M are shown in Table. 3.8.

If instead of taking $J = 1$, we take $M = 1$ and $J = 1, 2, 5, 10, 20$, the same attenuation values will be yielded as for the values for J and M. From the data included in Table 3.8, it is clear that the attenuation factor affects the decision very much unless $M < 2$. Therefore, it is advisable to use values for J and M that limit the product between J and M, to ensure that $JM <= 2$.

Table 3.8: Drift comparison

M	Extra attenuation
1	0.9366
2	0.8763
5	0.7128
10	0.4924
20	0.2080

3.4.4.4 Data modulation

Resorting to the simulations and formulas provided in [10], the attenuation caused by the data modulation effect for the detector under analysis can be described as shown in Eq. 3.58.

$$At_{data-mod} = \left| 1 - \frac{JMN_sT_s}{T_{bit}} \right|^2 . \tag{3.58}$$

A graph showing the data modulation attenuation for the GPS L1 C/A signal is presented in Fig. 3.16. The analysis has been restricted to a maximum integration time of 20 ms (however the study can be easily extended to other signals with different data bit period) because of the severe extra attenuation caused by the differential product. Hence, in this data modulation analysis, just one data bit transition can happen.

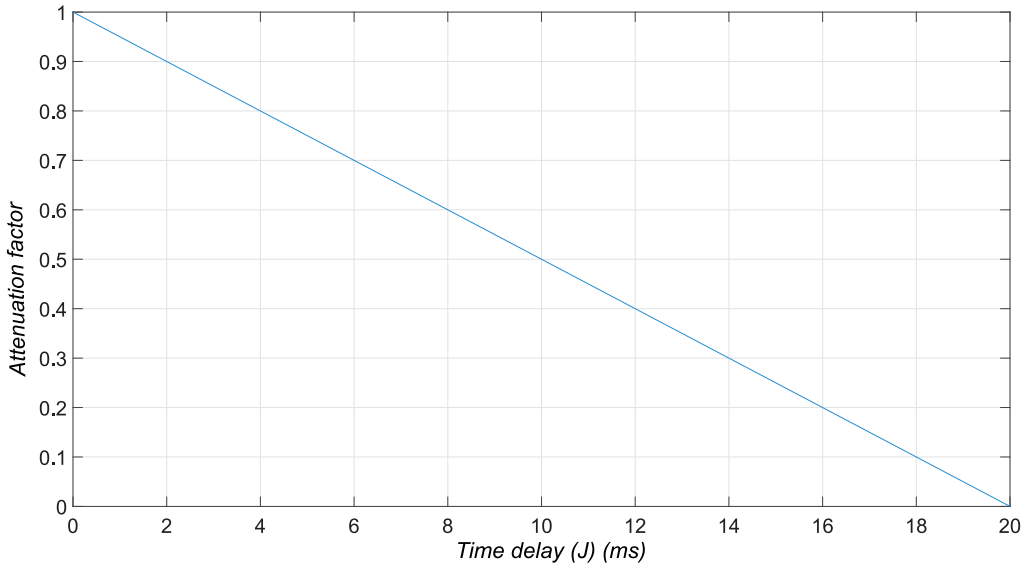

Figure 3.16: Differentially coherent detector data modulation attenuation.

JMN_s is the time delay between the signal segments used in the differentially coherent combination.

However, as stated in [9], the data modulation attenuation does depend on the Doppler frequency.

Again, the analysis of the terms R_m and R_{m-J} will be considered.

$$R_m = \sqrt{P(nT_s)} \exp\left(j\left(\phi_k + \frac{(2m+1)(w_d - \hat{w_d})MN_sT_s}{2}\right)\right) \frac{\sin\left(\frac{(w_d-\hat{w_d})MN_sT_s}{2}\right)}{\sin\left(\frac{(w_d-\hat{w_d})T_s}{2}\right)}, \quad (3.59)$$

$$R^*_{m-J} = \sqrt{P(nT_s)} \exp\left(j\left(-\phi_k - \frac{(2m+1-J)(w_d - \hat{w_d})MN_sT_s}{2}\right)\right) \cdot \cdot \frac{\sin\left(\frac{(w_d-\hat{w_d})MN_sT_s}{2}\right)}{\sin\left(\frac{(w_d-\hat{w_d})T_s}{2}\right)}, \quad (3.60)$$

the product of these two terms is,

$$R_m \cdot R^*_{m-J} = P(nT_s) \exp\left(j\left(\frac{J(w_d - \hat{w_d})T_sMN_s}{2}\right)\right) \frac{\sin\left(\frac{(w_d-\hat{w_d})MN_sT_s}{2}\right)^2}{\sin\left(\frac{(w_d-\hat{w_d})T_s}{2}\right)^2}. \quad (3.61)$$

However, if a bit transition occurs within the coherent integration interval the attenuation term, transforms into Eq. 3.62,

$$At_{diffmd} = \left(1 - 2\exp\left(j\left(\frac{J(w_d - \hat{w_d})T_sMN_s(1-t)}{2}\right)\right)\right) \frac{\sin\left(\frac{(w_d-\hat{w_d})MN_sT_st}{2}\right)}{\sin\left(\frac{(w_d-\hat{w_d})T_s}{2}\right)}. \quad (3.62)$$

Therefore, when one of the terms in the product $R_m \times R^*_{m-J}$ undergoes a data bit transition, the product can be expressed as shown in Eq.3.63,

$$R_m \cdot R^*_{m-J} = P(nT_s) \exp\left(j\left(\frac{J(w_d - \hat{w_d})T_sMN_s}{2}\right)\right) At_{data-mod}. \quad (3.63)$$

Finally, the decision statistic can be expressed as shown in Eq. 3.64.

$$\left|R_m \times R^*_{m-J}\right|^2 = \left|P(nT_s)\exp\left(j\left(J(w_d - \hat{w}_d)T_s M N_s\right)\right) At^2_{data-mod}\right|. \tag{3.64}$$

Once this product is analyzed, a final expression for the modulation data attenuation (if the integration time is such that Integration time (Tint)<Tbit), can be obtained by taking into consideration that two possible cases can happen:

1. The bit transition occurs in the first or last coherent integration segment, hence just one of the products entering the product is affected.
2. The bit transition occurs in any other coherent integration segment.

This behaviour is illustrated in Fig. 3.17.

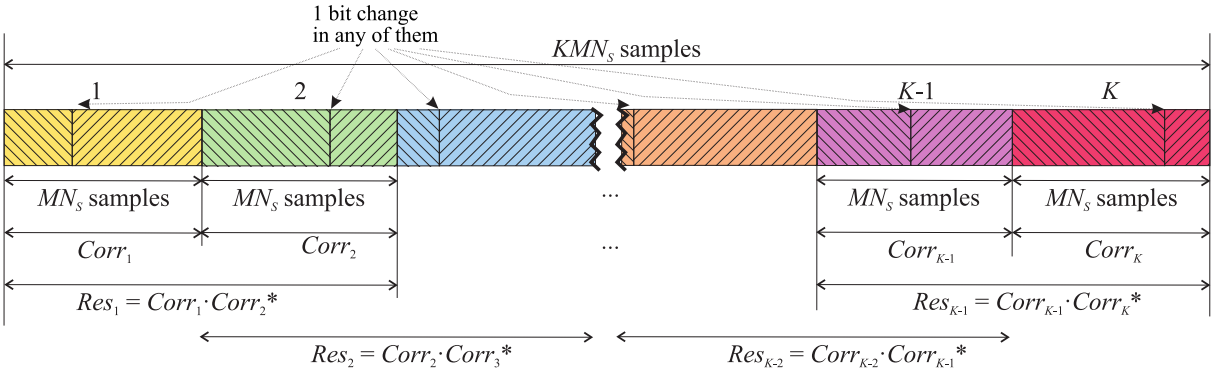

Figure 3.17: Differentially coherent detector data modulation $J = 1$.

For this case, expressions for the data modulation attenuation for this detector are given by Eq. 3.65 (case 1) and Eq. 3.66 (case 2).

$$At_{mod-data1} = \left(1 - \frac{M}{K-1}(1 - At_{data-mod})\right). \tag{3.65}$$

$$At_{mod-data2} = \left(1 - \frac{2M}{K-1}(1 - At_{data-mod})\right). \tag{3.66}$$

It is clear that, in general, the performance of the differentially coherent detector is worse than the performance of the non-coherent detector because except for the cases in which the data transition occurs in the first or last coherent integration intervals two coherent correlation integrations are affected by the data modulation effect instead of one.

3.4.5 Pre-correlation detector

The pre-correlation detector (referred to as differentially coherent in [9] or "delay and multiply" in [5]) works upon a completely different principle to the other detector schemes. Basically, this detector type eliminates the Doppler information at the input of the correlator by multiplying the input signal by a delayed and conjugated version of the input signal (i.e the Doppler behaviour is described by $\exp(jw_dT_sJ)$ being J the delay in chips). When the exponential term containing the frequency information is multiplied by the same delayed and conjugated exponential, the dependency with time of the complex exponential disappears and an appropriate choice of the delay yields minimal attenuation. Therefore, acquisition can be achieved just by correlating with the local replica code without having to perform a Doppler frequency search. This leads to a dramatic decrease in the computational cost, especially when dealing with high dynamic scenarios with large incoming Doppler frequency. However, a number of factors hindering the usage of this detector type must be addressed before. These problems are:

1. The fact the signal is multiplied before the correlation, implies that both the useful signal power and the noise power are squared. Taking into consideration that the noise power is bigger than the useful power, when performing the squaring operation the useful power decreases more than the noise power. This results in a decrease of the signal to noise ratio at the input of the correlator. Therefore, the magnitude of this attenuation must be studied in order to find out if the detector can be used in the case under study.

2. The choice of the delay is critical, as it controls the exponential attenuation term.This is a critical design parameter which must be well designed. Otherwise, the receiver does not work correctly as the the immunity to the input Doppler frequency is obtained just for some specific delays.

3. In the case the decision statistic is to be formed by taking the real part of the correlation result (by using just real part, half of the noise power is eliminated), the receiver performance improves because if J is carefully selected the useful signal component remains unaltered. Therefore, it is advisable to use the configuration which constructs the decision statistic by taking the real part of the correlation result.

4. Different small variations in the receiver shall be studied as they perform differently for the scenario under study, hence it is of paramount importance to quantify how each different detector perform in order to determine which configurations cope best with the scenario under study.

The above-mentioned factors will be assessed thoroughly in chapter 5 in order to determine if the pre-correlator detector can be used for a GNSS LEO scenarios. Therefore, empirical tests with signals coming from GNSS LEO scenarios will be performed in order to demonstrate empirically the receiver suitability for the case study.

3.5 Discussion

In this section a discussion of the suitability of different GNSS signals for the Low Earth Orbit (LEO) scenario, is provided. The analysis performed in the above section will be taken into account.

The signals which have absolutely no usage restrictions are:

1. L1 C/A.
2. E1 OS.
3. L1C.
4. L2C.
5. E5 OS.
6. L5.

Some preliminary considerations must be put forward. The E1 OS Galileo signal can be considered, despite the fact the signal contains a BOC(1,1) and a higher frequency BOC(6,1) (which requires a much higher sampling frequency), the fact the BOC(6,1) only contains $\frac{1}{11}$ of the signal power means it is possible to work using just the BOC(1,1) component. The Galileo E1 OS code has a length of 4092 chips with a code repetition of 4 ms and a bandwidth of 1.023 MHz. Moreover its spectrum is displaced 1.023 MHz, so it is necessary to use a sampling frequency of 4×4.092=16.386 Msps which suits quite well with the usage of the Fast Fourier Transform (FFT) radix-4 algorithm [61]. The Fast Fourier Transform (FFT) radix 4 algorithm is computationally more efficient than the traditional Fast Fourier Transform (FFT) radix-2 algorithm.

Another signal to be considered can be the L2C (CM, Civil Moderate signal) whose code bandwidth is 0.5155 MHz (not exactly 0.5155 MHz, because when multiplexing the CM and CL codes the binary rate is exactly the same as in the C/A code) and the repetition period is 20 ms which implies that it is necessary to work with signal of 10230 samples which is quite high in comparison with the 2046 required for the L1 C/A signal.

This problem was pointed out in [82], where the usage of the FFT was proposed to reduce the computational burden linked to the longer length codes. For the L1C signal, the code length is 10230 chips and the bandwidth is 1.023 MHz. A BOC(1,1) modulation is used and the period length is 10 ms, hence we will be working with signal fragments of 20460 samples, which is again quite higher than for the other L1 C/A case.

Nevertheless, in order to provide a reasoned discussion, it is compulsory to perform a quantitative analysis dealing with the aspects that have an influence on receiver performance.

The different aspects considered in evaluating the pros and cons in using each of the different GNSS available signals in the Low Earth Orbit (LEO) satellite scenarios are listed below:

1. Code length (linked to computational cost).
2. Doppler frequency.
3. Code drift (depends on central frequency and receiver motion).
4. Suitability for Pre-correlation detector (or Delay and multiply approach).
5. Minimum received power (depends on signal design).

Generally, the LEO scenario requires the usage of the most simple GNSS and Galileo signals. As highlighted in section 3.2.1, many LEO satellites suffer from available power shortages linked to a reduced size. Accordingly, the low power consumption requirement implies it is important to reduce the computational cost as much as possible.

3.5.1 Code length

The code length (in samples) is a key factor which determines the computational cost of the acquistion process. The acquisition process generally relies on calculating the FFT of code periods (or one code period).

When comparing the computational complexity of the L2C, Galileo E1 OS and Galileo E5 signals with the computational complexity of the L1 C/A signal, it is necessary to take into account that the length of the L2C, L1C and the Galileo E1 OS codes is larger than the L1 C/A code length. Moreover, it is well known that the computational complexity of a FFT is $5N\log_2(N)$ [54, 83].

Therefore the larger the code whose FFT is calculated, the bigger the computational cost is. This is a well known argument which is is sustained by the reasoning in [60].

To give a general proof of the above-mentioned argument, the following acquisition scenario is put forward:

1. A Doppler frequency estimation must be so precise that a 50 Hz error is achieved.
2. LEO scenario with Doppler frequencies spanning from -50 kHz to 50 kHz. This implies the Doppler search width is 100 kHz.
3. L1 C/A and the L1C are considered.

A comparison between the computational cost of the acquisition process for the L1C and the L1 C/A signals is to be performed. Basically, the aim of this study is to demonstrate that the code length (measured in samples) is the factor which determines the computational cost for the acquisition for a specific signal scenario.

The L1 C/A signal is sampled using N samples per code period, being N the number of samples corresponding to the minimum sampling frequency (f_s = 2.046 Msps). Therefore, for the L1C, signal $20N$ samples will be necessary attending to the fact the L1C code period is 10 times longer and the minimum sampling frequency is twice the minimum sampling frequency for the L1 C/A signal.

For the scheme presented in Fig. 3.18, the operation count can be described as follows:

1. 1000 complex multiplications.
2. 1000 FFT operations.
3. 1000 complex multiplications.
4. 1000 inverse FFT operations.

Here it is assumed that the FFT of the replica codes are calculated previously and stored, so it is not necessary to take this operation into account for the operation count. Taking this into consideration, for the L1 C/A signal, the computational cost is:

$10000N\log_2(N)$ flops + 2000 size N complex multiplications.

For the L1C signal, the computational cost is:

$$200000N\log_2(N)+864385N \text{ flops} + 2000 \text{ size } 20N \text{ complex multiplications.}$$

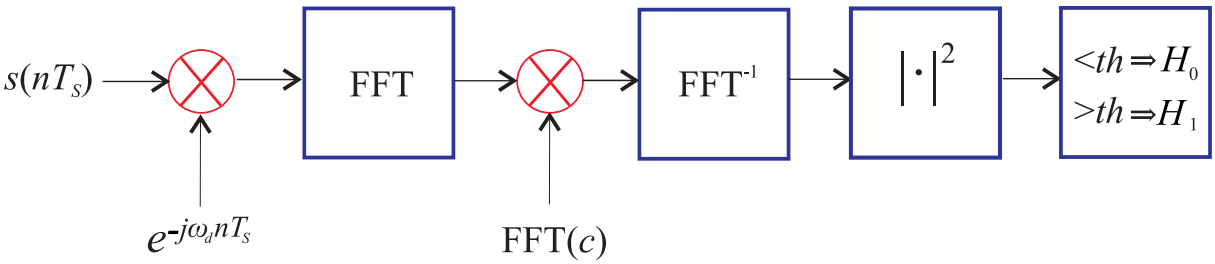

Figure 3.18: FFT-based coherent acquisition.

An additional remark to illustrate this argument, is to consider that, if we are dealing with a C/A code of length N and a L1C code of length $20N$, then it follows that the ratios of the computational complexity for the FFTs of both code types (with N=2046) is expressed in Eq. 3.67 (if $N = 2046$).

$$\frac{CC_{L1C}}{CC_{C/A}} = \frac{20N\log_2(20N)}{N\log_2(N)} = 27.859 \tag{3.67}$$

From this analysis, it is clear that the code length is the key factor determining the computational cost of the acquisition algorithm. Therefore, for a traditional FFT-based acquistion, the smaller the code, the faster the acquisition process. For a case in which the signal level is high and there is no need to extend the integration time, it is clear that the L1 C/A signal (shorter code in samples) is the best choice computationally-wise.

A simple procedure to decrease the computational cost linked to the acquisition process, is to use the FFT shift property. By performing a FFT shift, it is possible to perform the complex multiplication by $e^{jw_d nT_s}$, because the shift in the FFT is equivalent to the complex multiplication [9]. This property is used to reduce the computational burden of the acquisition process in [64, 80, 84, 85]. The frequency resolution of the FFT operation depends on the actual time duration of the signal under analysis. Accordingly, if we recall that the code repetition period of the L1C signal is 10 times longer than the code repetition period for the L1 C/A code, it follows that the frequency resolution for the FFT of one L1C code period is ten times more precise than the frequency resolution for a L1 C/A signal. Taking into consideration that the code repetition periods for the L1C and L1 C/A codes are 1 ms and 10 ms, respectively, it follows that the frequency resolutions for the

L1C and L1 C/A are 100 Hz and 1000 Hz, respectively. Accordingly, the FFT operation is more profitable in the L1C case, as a bigger reduction in Doppler search bins is achieved.

The block diagrams of the implementation of the FFT shift acquisition for the L1C and L1C/A signals are shown in Fig. 3.19 and Fig. 3.20, respectively. Note here that Fig. 3.19 uses the same procedure as the one presented in [80].

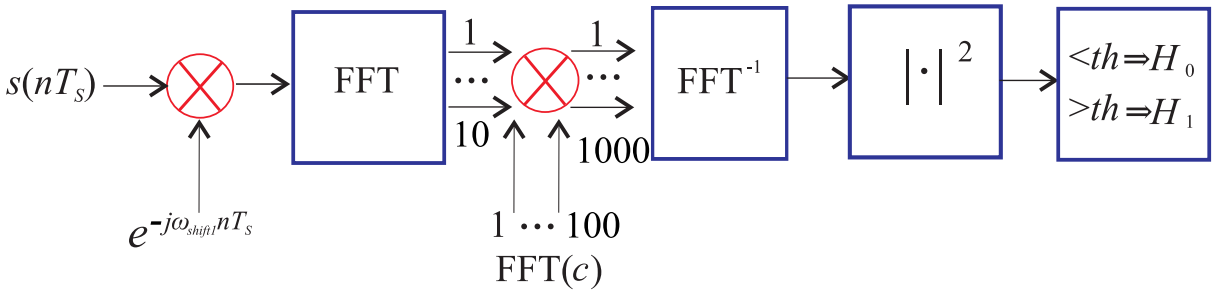

Figure 3.19: FFT shift-based L1C/A code coherent acquisition.

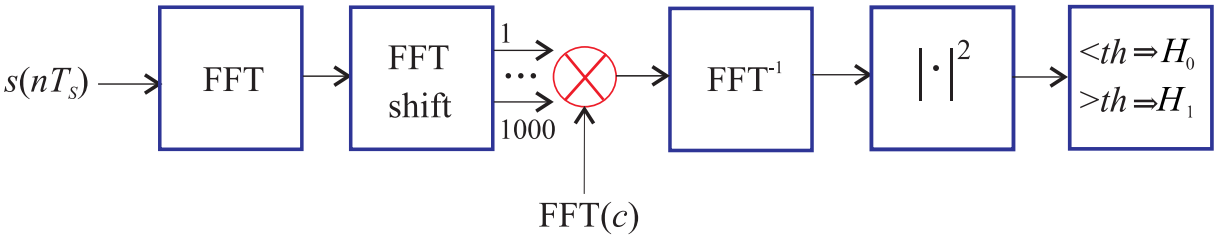

Figure 3.20: FFT shift-based L1C code coherent acquisition.

Now, the question arising is if for the FFT shift implementation the L1 C/A signal is still less computationally burdensome than the L1C signal. To answer this question we will rely on the diagrams presented in Fig. 3.19 and Fig. 3.20.

For the L1C signal the operation count can be described as follows:

1. 1 FFT with $20N$ points.
2. 1000 complex multiplications of vectors with size $20N$ samples.
3. 1000 inverse FFT with $20N$ points.

This translates into the following flop count:

$100100N\log_2(N)+$ 432625N flops + 1000 size $20N$ complex multiplications.

For the L1 C/A signal the operation count can be described as follows:

1. 10 complex multiplications of vectors with size N samples
2. 10 FFT operations of vectors with N points.
3. 1000 complex multiplications of vectors with size N samples.
4. 1000 inverse FFT with N points.

This translates into the following operation count:

$5050N\log_2(N)$ flops + 1010 size N complex multiplications.

Clearly, the L1 C/A signal computational burden is less than the computational burden for the L1C signal. This is so because of the fact the the L1C length in samples is larger than the L1 C/A code length is samples. One can realize that $100100N$log2$(N)+$ 432625N flops $>5050N\log_2(N)$ and 1010 size N complex multiplications are less computationally expensive than 1000 size $20N$ complex multiplications, hence it is demonstrated that the computational cost for the coherent L1 C/A acquisition is smaller than for the L1C signal. Accordingly, the code with shorter length in samples will be the code whose computational burden is smaller.

From the previous analysis, it is clear that the code length is a key factor affecting the computational cost. From the ratio in Eq. 3.67, it appears that the code length effect on the computational cost is much bigger than the effect of the different Doppler search space (a factor of 27 vs a factor of approximately 1.5 when comparing L2C and L1 C/A).

Finally, another aspect to consider is that the FFT algorithm is applied to sample lengths which are powers of 2 (or 4 for the radix 4 FFT). 2046 samples is very close to 2048 which is 2^{10} which is quite efficient. However, it is important to find out if all of the signals under study cope that well with the efficient use of the FFT.

In Table 3.9, the closest powers of 2 and 4 in which the minimum sample length for the codes represented, is shown.

From the table, it is clear that, from the FFT efficiency point of view, the minimum number of samples only fits well for the L1 C/A and the E1OS signals.

Table 3.9: Powers of 2 and 4

Signal	Code length (samples)	Nearest power of 2	Nearest power of 4
L1 C/A	2046	2048	4096
L1C	40920	65536	65536
L2C	40920	65536	65536
L5	20460	32768	16384
E1OS	4092	4096	4096
E5OS	20460/51150	32768/65536	65536/65536

From the points illustrated in this analysis, it is clear that the smaller the code length, the lower the computational cost. From this point of view, one can assume that the L1 C/A signal is the most cost-effective choice for a high dynamics scenario.

3.5.2 Doppler frequency

It is clear that for the signals under study, the search space changes as the Doppler frequency changes. Hence, the Doppler search space (without accounting for the clock unstability) is shown in Table 3.10. The normalized factor in Table 3.10, is the ratio between the maximum seach space (search space for E1 and L1) and the search spaces for rest of the frequency bands.

Table 3.10: Search space in kHz

Band	Search space (kHz)	Normalized factor
L1	85	1
E1	85	1
L5	65	0.765
E5	65	0.765
L2	66	0.766
E6	69	0.812

Accordingly, when measuring the computational cost for the different signals in Table 3.10 are to be used in spite of the different search spaces.

3.5.3 Code drift

As stated in section 3.4.3.3, a non corrected code phase drift in a high dynamics scenario can lead to severe signal attenuation. Hence it is necessary to take into consideration how the different GNSS signals behave under the presence of a large Doppler effect. From the comparisons in [1], it is clear that the L1 C/A signal performs the best when dealing with scenarios under large Doppler frequency drifts. Therefore it is clear that the L1 C/A signal is the signal which copes the best with the scenario under study.

3.5.4 Delay and multiply suitability

It is well known that the delay and multiply approach increases the noise power at the input of the correlator [29,63]. Accordingly, this detector type will work better with high received powers and signals with small input noise power. The signal whose bandwidth is smaller (the larger the bandwidth the larger the input noise power) and whose received power is larger is the L1 C/A signal. The L1 C/A signal has the smallest bandwidth and this is advantageous when considering the effect of the squaring loss prior to the correlator input. The smaller the the noise power, the smaller the squaring loss effect [63, 81]. Moreover, the higher the useful signal power, the smaller the squaring loss [63,81]. Taking these points into consideration, it appears that the choice of the L1 C/A signal for the LEO is an adequate choice.

3.6 Concluding remarks

The most important conclusions from the analysis on the chapter can be summarized as follows:

1. It is clear that the residual effects establish limits in the different detectors performance. Therefore, it is important to find out if the proposed SDR methodology can reproduce these effects. If the proposed SDR methodology succeeds in reproducing the residual, then it is possible to ensure that the proposed SDR methodology is a means of giving experimental proofs for the cases under analysis. This point will be discussed in chapter 4.

2. From the analysis regarding computational cost and sensitivity to code drift, it is clear that the L1 C/A signal is linked to the lowest computational cost and is the most insensitive to code drift. These two facts suggest that using the L1 C/A signal in the LEO scenario may be advisable.

3. The differentially coherent detector can only be used the LEO scenario with if the product $J \cdot M <= 2$. In fact, this condition is so restrictive that it is not advisable

to use this detector type for the scenario. Some detector architectures which form the detection statistic in the differentially coherent manner will be tested in chapter 5.

4. For any detector type, it is advisable to use low M values to limit the computational cost. This implies that for the scenario under study, the use of long coherent integration times is not advisable.

5. It appears that the usage of the L1 C/A signal, along with the pre-correlation detector is appealing. In chapter 5, a thorough study of this detector type for the LEO scenario is to be performed. In this chapter, a study to demonstrate that the pre-correlation detector is faster than standard detector schemes and that this detector can be used for LEO scenario. This is to be done by performing empirical tests measuring execution speed and post-correlation signal power level. Furthermore, this study is a major contribution, as the adequateness of the pre-correlation detector is demonstrated. In this way, theoretical and empirical evidence of a procedure that enhances receiver performance is provided.

Chapter 4

Technological demonstrator

4.1 Introduction

The aim of this chapter is to show that the results obtained using the proposed technological demonstrator agree with the theoretical behaviour presented in Chapter 3. The more the technological demonstrator behaviour resembles the behaviour portrayed in theory, the more successful the technological demonstrator is. Moreover, a comparison between the performance of the Universal Serial Bus (USB) dongle and the USRPx310 is performed in order to explore the different possible scenarios which can be simulated with each hardware setup.

4.2 Technological demonstrator

The technological demonstrator uses a SDR philosophy. As stated before, in Chapter 1, the SDR philosophy relies on implementing tasks which have been accomplished traditionally via hardware by treating the digitized signal samples using software routines. The reasons behind the usage of this philosophy are (among others):

1. The SDR philosophy is extremely flexible in that it is possible to implement the detector type and navigation algorithms at will.
2. The SDR philosophy allows to study the high dynamics scenario (circumventing the Coordinating Committee for Multilateral Export Controls (CoCom) restrictions in a legal manner. If no navigation position is calculated, the rules dictated by

the CoCom restrictions are not contravened because these restrictions only prohibit the navigation position calculation. Standard commercial receivers cannot be used for high dynamics studies, as these receivers are not designed for a high dynamics scenario and cannot be customized by the user.

3. A relatively high-quality demonstrator can be constructed at low cost (if the investment on the GNSS signal generator is not considered).

4. The tests are controllable and repeatable.

5. Platform motion is simulated, hence reducing costs and risks linked to field testing. Moreover, the fact the tests are conducted within a laboratory implies that the tests are completely safe.

In this work different technological demonstrators will be considered as different hardware elements will be used to implement each of the functional blocks. Lets recall that the technological demonstrator will comprise in all cases the following elements (see Fig.1.2):

1. Signal generator: Part in charge of generating the GNSS signal as it would arrive to the receiver front-end in a high dynamics scenario. The different options under analysis for the signal generator are: a Spirent GSS7700 (for GPS L1 C/A signal generation) and a Rohde & Schwarz SMBV100A (for Galileo E1 OS generation).

2. Digitizing hardware: Two different devices can be used for this purpose. A USRPx310 and a USB dongle based on the Rafael 820 Tuner (R820T) and the RTL2832 Integrated Circuit (IC) can be used.

3. Software end. A driver that can handle the input samples via USB is required in case the USB dongle (RTL-SDR) is used whereas the UHD driver is used for the USRPx310. The samples can be stored in a file or fed to the software routine implementing the functions of a GNSS receiver. Many different programming languages can be used to implement this features (C, Python, Scilab, Octave or Matlab GNU Radio or GNSS-SDR among others). For the tests performed in this work Matlab is used, however some tests using C and Scilab were performed, but despite yielding slower computation times, Matlab was the selected language because of its simplicity.

From the list above, it follows that a vast amount of possibilities are available in order to implement the technological demonstrator. However, some further considerations

must be taken into consideration in order to find out which are the possible combinations of hardware that can be put forward. To accomplish these tasks, first, the technical characteristics of the possible signal generators and receiver front-ends must be thoroughly analyzed. The hardware presented in this chapter is part of the equipment from the "Laboratorio de Guiado y Control" at INTA.

4.2.1 GSS7700

The GSS7700 used within the frame of this work is a high-end dedicated GNSS simulator, especially designed to simulate high dynamics scenarios. The core of the GSS7700 comprises, basically, FPGAs and precise clocks. The main capabilities and characteristics of the specific simulator used in the frame of this work can be summarized in the following list:

1. It is possible to synchronize the instant at which the signal is generated with the instant at which the signal is received using the Pulse Per Second (PPS) output (a signal emitting a pulse per second is transmitted through this port).
2. Two output RF ports are available. Hence, it is possible to generate the signal for two scenarios at the same time.
3. The C/A signal and the L2C signal can be generated. Each of the two RF ports can operate at the same time using the L1 and L2 frequency or it is possible to generate the L1 signal at the same time in the two ports. Furthermore, for validation purposes it is also possible to generate exactly the same signal in the two ports.
4. Scenarios with vehicles travelling at speeds smaller than 1200000 m/s can be simulated. This is clearly a high dynamics feature.
5. It is possible to generate satellite errors, atmospheric signal degradation, signal shadowing, multipath and antenna transmitter and receiver radiation patterns.

Once these parameters have been configured, the software can adapt the signal simulation to the user defined scenario. Moreover, the receiver dynamics are simulated with six degrees of freedom. The logs containing all the information can be exported using the National Marine Electronics Association (NMEA) format.

4.2.2 Rohde & Schwarz SMBV100A

The Rohde & Schwarz SMBV100A signal generator is not a dedicated GNSS signal generator, in fact the generator can simulate signal following the specification of well known digital radio standards or some mobile communications signals. In this work, the Rohde & Schwarz SMBV100A signal generator is to be used to simulate the Galileo E1OS signal in a LEO scenario. The standard version of this generator does not generate high dynamic scenarios as it can only generate scenarios with a single vehicle whose maximum speed is 600 m/s, however a special version of the generator can generate scenarios with a single vehicle with a maximum speed of 100000 m/s.

The main capabilities and characteristics of the simulator are summarized in the following list:

1. Just one output RF port is available. However it is possible to generate the signal for two scenarios at the same time by synchronizing a master generator with a slave generator, i.e. two generators are necessary for this feature.
2. E1OS Galileo signal can be generated.
3. Scenarios with vehicles travelling at speeds smaller than 100000 m/s can be simulated. This is clearly a high dynamics feature.
4. It is possible to generate satellite errors, atmospheric signal degradation, signal shadowing, multipath and antenna transmitter and receiver radiation patterns.

4.2.3 USRPx310

The USRPX310 is defined by the manufacturer as a scalable SDR platform for the design of generic wireless communications systems. The hardware architecture comprises two extended bandwidth daughterboard slots which provide multiple high-speed interface options such as Peripheral Component Interconnect Express (PCIe), Gigabit Ethernet (GigE)). These interfaces give access to the user-programmable Kintex-7 FPGA. Furthermore, the UHD (which is a dedicated driver) provides low-level routines that can handle the communication between the USRP device and the host computer granting access to some receiver configuration parameters.

The block diagram is shown in Fig. 4.1. The figure was taken from the commercial information provided in [86].

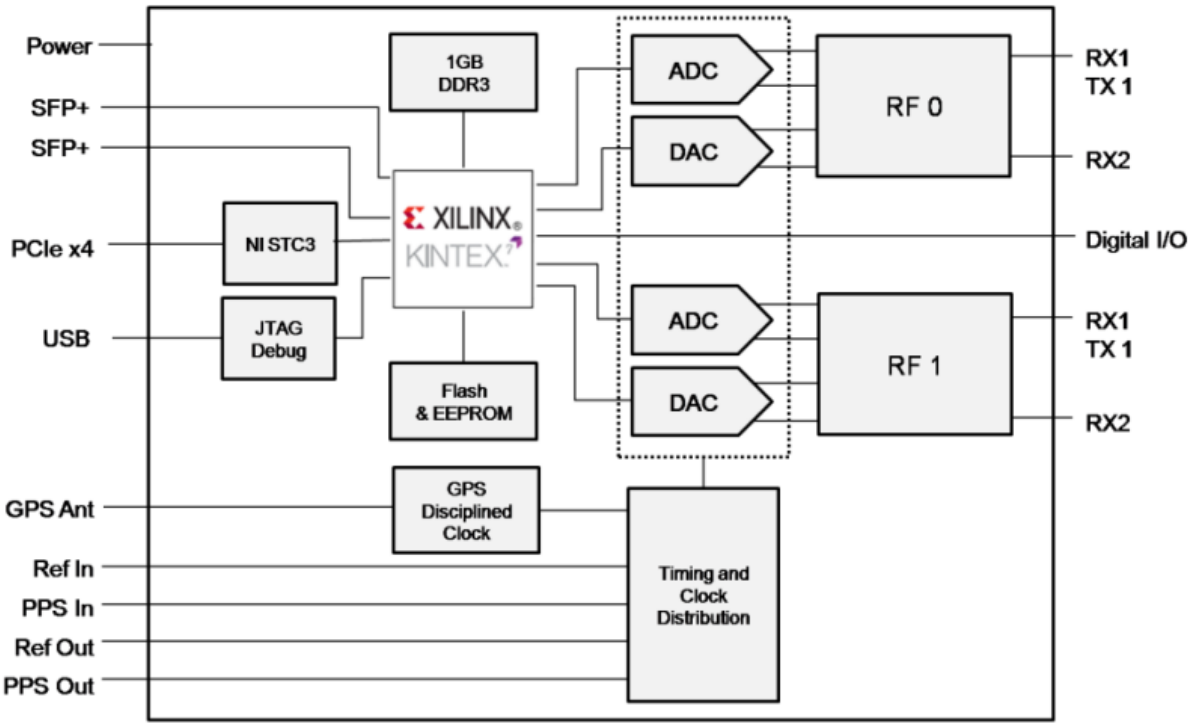

Figure 4.1: USRP block diagram (from [86]).

From Fig. 4.1, it follows that the two available daughterboards with two receiver ports and one transmitter port (with their corresponding ADC and Digital to Analog Converter (DAC)) are controlled via a FPGA which can be programmed using the Joint Test Action Group (JTAG) port. The architecture also comprises a EEPROM and a Random Access Memory (RAM). A clock with 20 Part Per Billion (PPB) stability is used as the timing reference. The clock stability can be further improved by using a GPS disciplined clock [87].

The important features of the USRP can be summarized in the following list:

1. Working frequency: 0 MHz to 6000 MHz.
2. Number of bits: 14.
3. Sampling rate (without sample loss): 200 Msps (if the host computer can cope with the sample rate).
4. Clock stability: 20 PPB.

4.2.4 USB dongle

The USB dongle used in this work is the Newsky TV82T. Even though this detector was first envisioned as a TV receiver [33], it was latter demonstrated that it could be used as a generic RF front-end which is able to receive a GNSS signal. The received GNSS signal is digitized and the digitized I/Q samples are sent via USB to the host computer. The internal structure of the dongle comprises a Micro Coaxial Connector (MCX) which connects the antenna cable with the dongle, a sintonizer chip (R820T) a RTL2832U chip which contains the necessary electronics to handle the I/Q samples and an Erasable Electronic Read Only Memory (EEPROM).

The block diagram is shown in Fig.4.2.

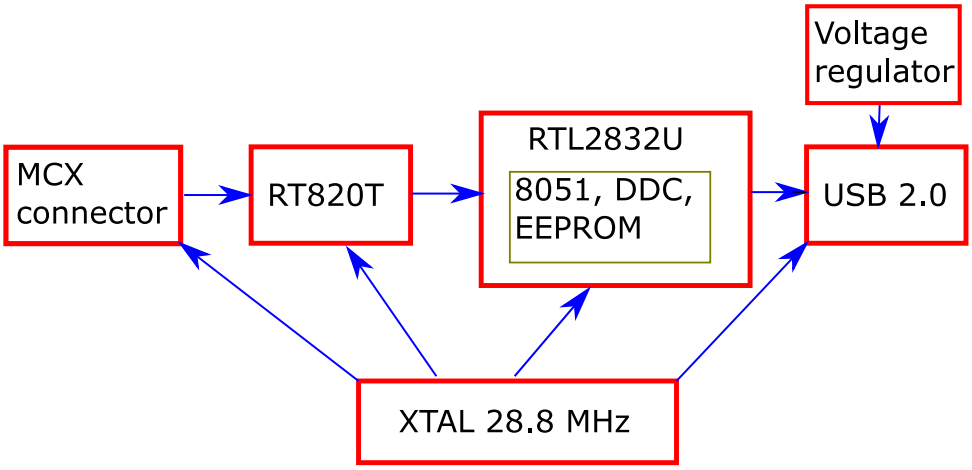

Figure 4.2: USB dongle block diagram.

The RT820T tuner works in the frequency band spanning from 24 MHz to 1760 MHz, hence it is possible to receive GNSS signals. The tuner amplifies and filters the received signal and downconverts the signal to an IF of 3.57 MHz. The IF I/Q components are then digitized using an 8 bit analog to digital converter. Furthermore, the RTL2832U integrated circuit is able to send the samples into the host computer using a binary rate of 2.4 Mbps (without losing samples). Actually, the RTL2832U contains an 8051 microcontroller which is in charge of the USB control but the microcontroller does not deal with the actual samples. In fact, the RTL2832U chip contains an Analog to Digital Converter (ADC) which samples the signal with a fixed rate of 28.8 MHz (in this case the 50 Part Per Million (ppm) error crystal oscillator was substituted by a 0.5 ppm error Temperature Controlled Oscillator (TXCO)). This signal is then passed to a digital downconverter, then a lowpass-filter is applied and finally the signal is resampled. In

fact, inside the RTL2832U, all the different elements within the dongle are controlled by the crystal oscillator. Using the RTL-SDR driver it is possible to dump the digital I/Q samples to a data file. GNU radio is also able to interact with this hardware.

The important features can be summarized in the following list:

1. Working frequency: 24 MHz to 1760 MHz.
2. Number of bits: 8.
3. Sampling rate (without sample loss): 2.4 Msps.
4. Clock stability: 0.5 ppm.

4.2.5 Discussion

Insight regarding two comparisons will be considered in this discussion. The comparison between the signal generators will determine which scenarios and signals can be actually generated. Later, the comparison between the two receiver front-ends determines which signals can be received. The information of both comparisons will be combined and in this way it will be possible to determine which signals can be studied in the proposed technological demonstrator framework.

Clearly, if one wants to study high dynamics scenarios subject to large Doppler frequencies and to relatively fast changes in the Doppler frequency, it is advisable to use the USRPx310 instead of the dongle because the 0.5 ppm stability error will yield a 787 Hz error (which could mask some Doppler frequency dynamics effects), whereas the USRPx310 20 PPB stability error yields a 31.5 Hz error in the estimation which is close to being considered negligible.

Another aspect to take into consideration is that the number of bits used by the USRPx310 to digitize signals is 14 instead of 8. Hence, the USRPx310 can cope with signals whose dynamic range is larger than for the case of the USB dongle [88]. This is important to consider in cases in which jamming is under study because the jammer signal tends to have a much bigger power than the GNSS signal, hence the larger the dynamic range (and the larger the number of bits) the better the receiver can cope with jamming devices [89]. Even though in this work, jamming scenarios are not going to be studied, it is important to include this jamming consideration as it might be interesting to consider the combined effects of jamming and high dynamics, in future studies.

For both the USRPx310 and the USB dongle, the front-end receiver band and frequencies are suitable for GNSS signals.

The sampling rate of the USB dongle can only cope comfortably with the L1 C/A signal and the L2C signal [90]. At this point it is important to recall that 2.4 Msps $>$ 2.046 Msps (minimum sample rate for L1 C/A) but 2.4 Msps $<$ 4.092 Msps (minimum sample rate for Galileo E1 OS). Hence, the possible studies which can be performed using the USB dongle are limited to the L1 C/A and L2C signals. On the other hand, the sampling rates which can be processed using the USRPx310 imply it is possible to process any GNSS signal.

4.3 Performance evaluation

In order to evaluate the performance and the capabilities of the technological demonstrator, different experiments using the coherent detector SDR implementation will be carried out. Furthermore, a Septentrio PolaRx2 receiver has been used to validate the results (to make sure that the obtained results are correct, however the PolaRx2 results are not included as the PolarRx2 result were just used for validation purposes). The PolaRx2 receiver does not provide user position beyond the CoCom limits, however it does acquire and track satellites beyond the the CoCom limits.

1. Configuration 1: Doppler behaviour of the coherent detector for L1C/A signal, using the Spirent+USRPx310 configuration.
2. Configuration 2: Doppler behaviour of the coherent detector for L1C/A signal, using the Spirent+USB dongle configuration.
3. Configuration 3: Doppler behaviour of the coherent detector for the Galileo E1 OS signal, using the Rohde & Schwarz+USRPx310 configuration.
4. Configuration 4: Code phase behaviour of the coherent detector for L1C/A signal, using the Spirent+USRPx310 configuration.
5. Configuration 5: Code phase behaviour of the coherent detector for the Galileo E1 OS signal, using the Rohde & Schwarz +USRPx310 configuration.

For each and every configuration, the same software acquisition block (coherent detector) will be considered. If theoretical and empirical data agree, the proper operation of the technological demonstrator is ensured. Hence, the behaviour of the algorithm implementation under study (taking for granted that the software implementation is correct) can be studied by performing a comparison with the baseline coherent detector.

4.3.1 Configuration 1

In order to evaluate the Doppler behaviour of configuration 1, the theoretical Doppler frequency error estimation response will be compared with the obtained Doppler frequency error response. To do so, a signal generated using the Spirent simulator with a known Doppler frequency will be used. The comparison procedure will be as follows

1. Obtain the theoretical Doppler attenuation with $M = 1$, $N_s = 2041$ (accordingly $f_s = 2.041$ Msps). At this point we must recall that Eq. 3.25 is a good a approximation only when the chip error is less than one chip and the Doppler error is less than 1 kHz [1]. More specifically, the error for the above-mentioned code phase/Doppler region is less than 0.58%. Moreover, when the phase error is zero (this will be the case for all the cases under study), the error is even smaller. Therefore, Eq. 3.25 can be used to establish a theoretical comparison.

2. Use the SDR coherent detector to acquire the signal. In this way, it is possible to obtain the acquired (or empirical Doppler) attenuation using the cross-ambiguity function with M=1, N_s=2041 (accordingly $f_s = 2.041$ Msps).

3. Compare empirical and theoretical Doppler attenuation responses (the closer the empirical and theoretical attenuation responses are, the better the theoretical demonstrator is).

In Fig. 4.3, the theoretical Doppler attenuation and the empirical Doppler attenuation are compared. Note that the empirical Doppler is centered in 630 Hz. Nevertheless, the Spirent generated signal, is centered at a 615 Hz Doppler frequency. However, the 15 Hz error is within the margins discussed in section 4.2.5.

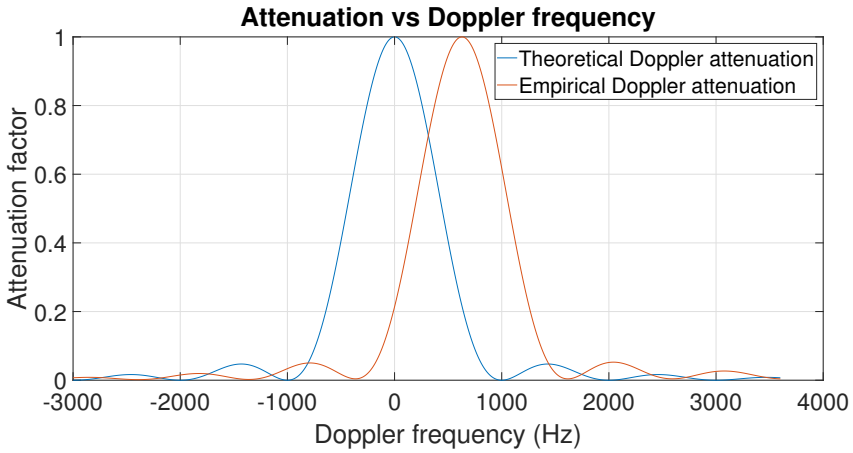

Figure 4.3: Theoretical and empirical Doppler attenuation comparison for configuration 1.

If the Doppler shift in the input signal is eliminated, the comparison is shown in Fig. 4.4

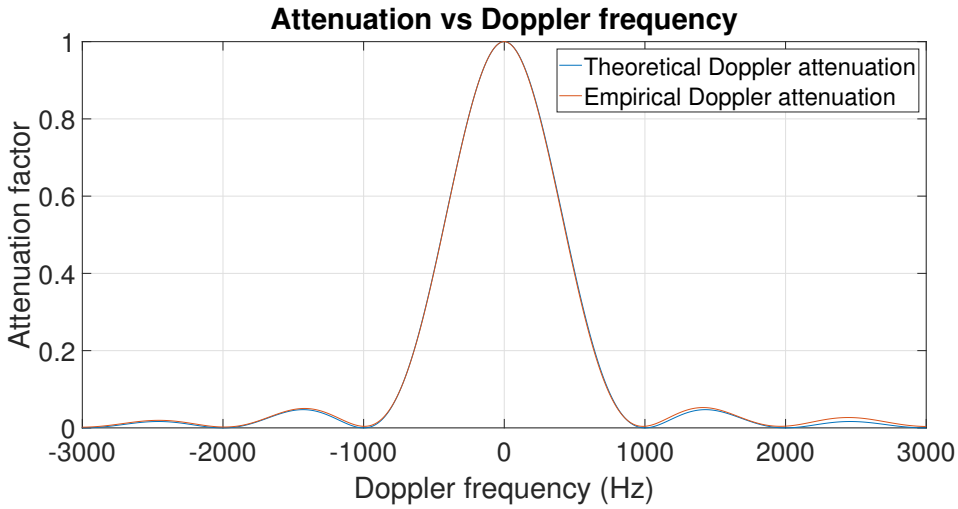

Figure 4.4: Theoretical and empirical (0 Hz) Doppler attenuation comparison for configuration 1.

The two graphs are virtually coincident, hence it is proved that using configuration 1 it is possible to correctly reproduce the Doppler effect. The high degree of resemblance between the graphs, implies that the Doppler behaviour has been correctly reproduced in the case under study. Accordingly, it is possible to study (from the Doppler effect study point of view) GNSS acquisition algorithms using this configuration.

4.3.2 Configuration 2

Exactly the same procedure and simulated signal than in configuration 1 will be used. However, the signal in this case will be processed using the USB dongle. The comparison procedure will be the procedure explained in the following list:

1. Obtain the theoretical Doppler attenuation with M=1, N_s=2048 (accordingly f_s = 2.048 Msps).
2. Use the SDR coherent detector to acquire the signal. In this way, it is possible to obtain the acquired (or empirical Doppler) attenuation using the cross-ambiguity function with M=1 and N_s=2048.
3. Compare empirical and theoretical Doppler attenuation responses (the closer the empirical and theoretical attenuation responses are, the better the theoretical demonstrator is).

In Fig. 4.5, the theoretical Doppler attenuation and the empirical Doppler attenuation are compared. Note that the empirical Doppler is centered at 180 Hz. However, the generated signal has a 630 Hz Doppler frequency. The 445 Hz error is within the margins discussed in section section 4.2.5.

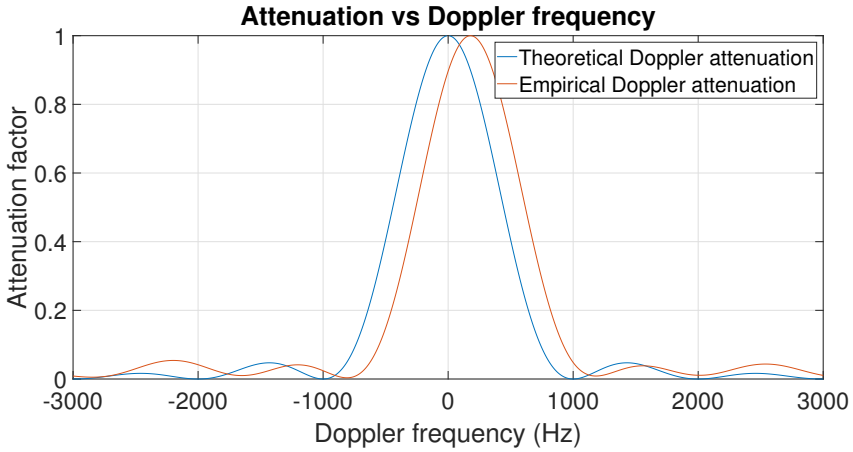

Figure 4.5: Theoretical and empirical Doppler attenuation comparison for configuration 2.

If the Doppler shift in the input signal is eliminated the comparison is shown in Fig. 4.6

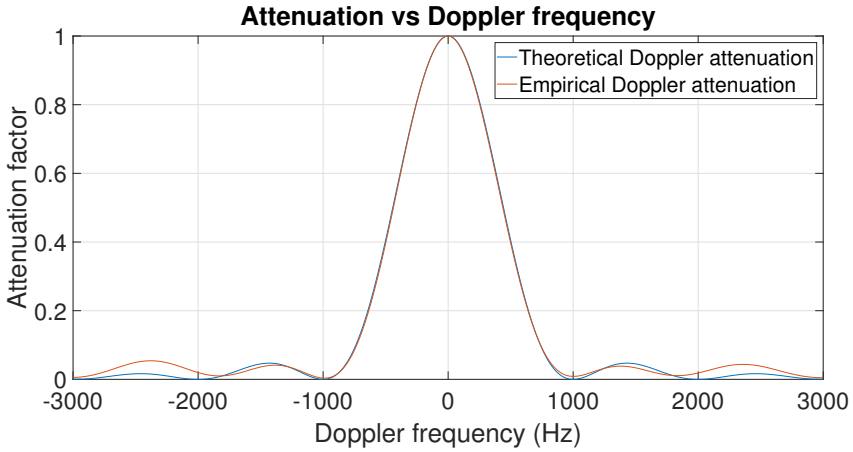

Figure 4.6: Theoretical and empirical (0 Hz) Doppler attenuation comparison for configuration 2.

In this case it possible to appreciate some differences between the two graphs, especially when the absolute value of f_d>2 kHz. However, it is proved that using configuration 2 it is possible to reproduce the Doppler effect when the absolute value of f_d<2 kHz, which is the most interesting area in the evaluation of acquisition performance. Accordingly, it

is possible to study GNSS acquisition algorithms using this configuration if considering Doppler effect. Nevertheless, it is clear that configuration 1 (see section 4.3.1) reproduces the theoretical Doppler frequency response (see section 3.4.2.3) in a more precise manner.

4.3.3 Configuration 3

The same 3-step validation procedure as in configuration 1 will be used. Nevertheless, the signal generator is in this case is the Rohde & Schwarz generator and a Galileo E1OS signal is generated. The sample rate is now 8.333 Msps, in order to cope with the Galileo E1OS signal bandwidth. Fig 4.7 shows that the drift in the Doppler estimation is just 60 Hz.

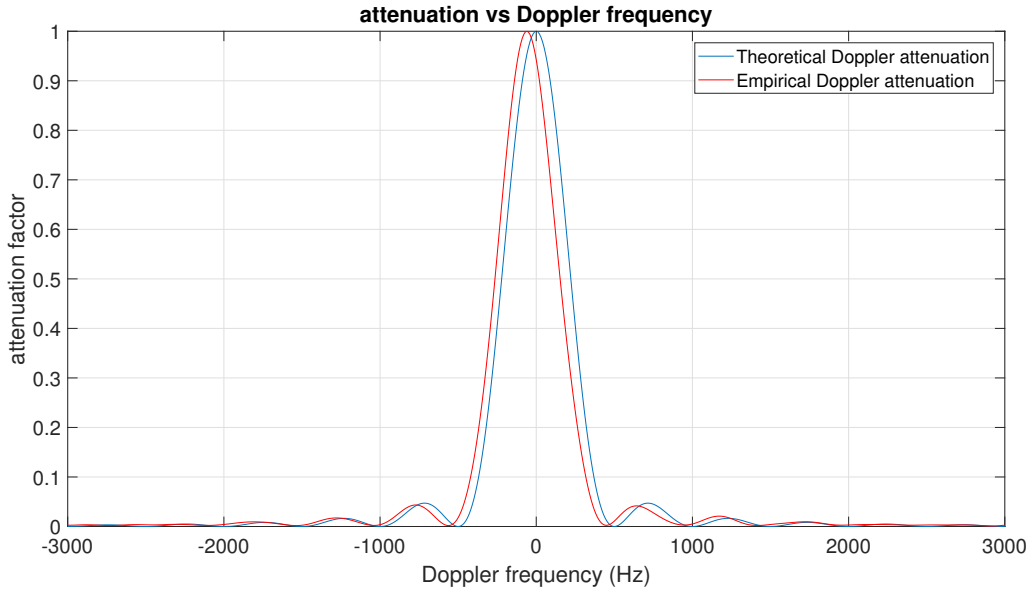

Figure 4.7: Theoretical and empirical Doppler attenuation comparison for configuration 2.

If the Doppler shift in the input signal is eliminated the comparison is shown in Fig. 4.8

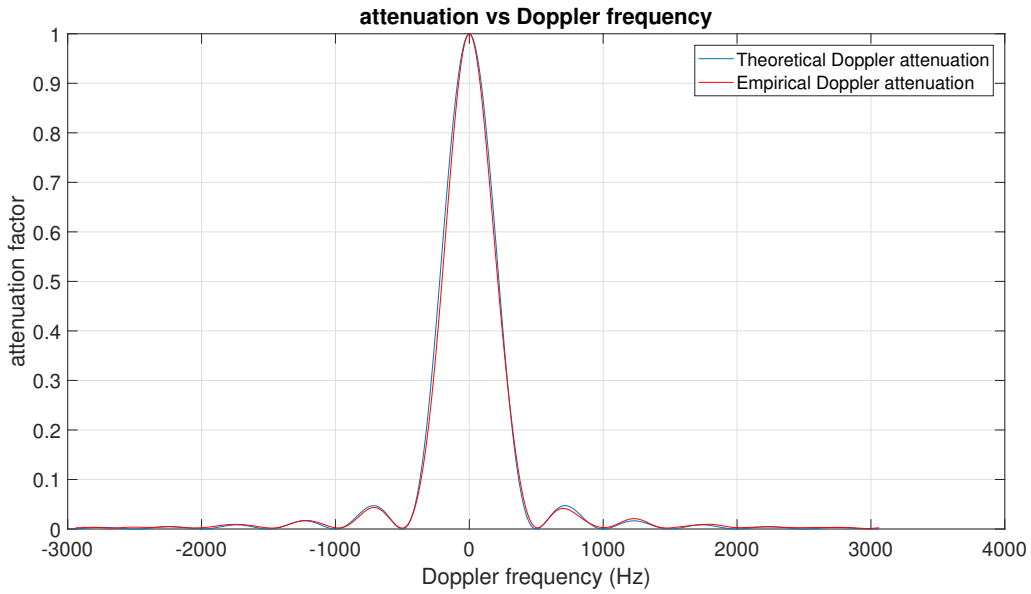

Figure 4.8: Theoretical and empirical (0 Hz) Doppler attenuation comparison for configuration 2.

Fig. 4.8 supports the idea the theoretical and empirical Doppler responses behave very similarly, hence the technological demonstrator when using configuration 3, succeds in reproducing the Doppler effects.

4.3.4 Configuration 4

Configuration 1 will be replicated in this case, but now the code phase behaviour is considered. The procedure (procedure 4) in this case will be as follows:

1. For a set of 2 sets of 600 signals (set 1 with $f_s = 2.041$ Msps and set 2 with $f_s = 8.333$ Msps) with a small Doppler frequency value (the absolute value of $f_d < 1$ kHz), the coherent acquisition algorithm is applied. The maximum peak value for each of the signals is recorded. Each of the 600 signals will be generated by taking the same signal generated by the GNSS generator with random start points within the same 20 ms interval.

2. Find out if Eq. 3.28 applies. This will be achieved if the maximum attenuations caused by code phase errors match Eq. 3.28.

A histogram showing the maximum correlation peak for each of the 600 experiment realizations is shown in Fig. 4.9.

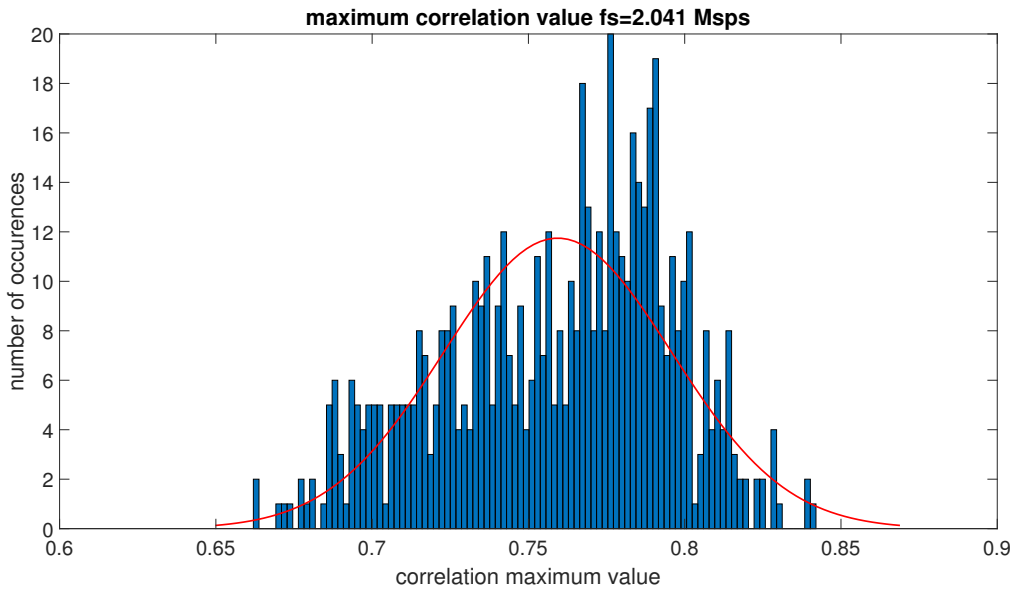

Figure 4.9: Histogram for quotient correlation distribution for f_s=2.041 Msps.

The same experiment for a sampling frequency of f_s=8.333 Msps is performed, the histogram showing the results is presented in Fig. 4.10.

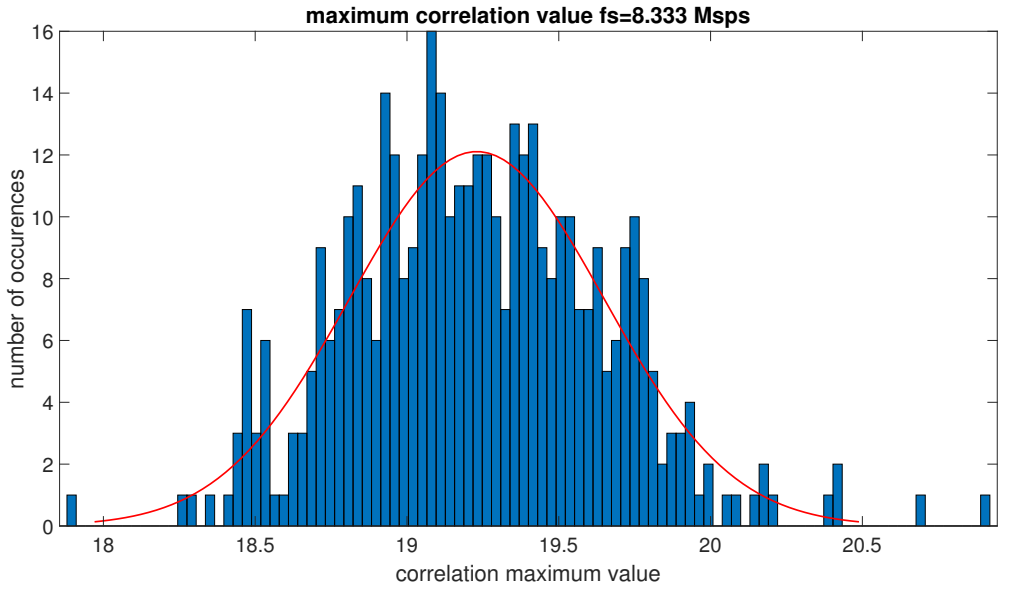

Figure 4.10: Histogram for quotient correlation distribution for f_s=8.333 Msps.

From the analysis of the plots, it is important to highlight that if the quotient between the difference between the maximum and minimum value and the mean value

is calculated, the normalized span is bigger for the case in which f_s=2.041 Msps than for the case in which f_s=8.333 Msps (0.3273 vs 0.2264). This behaviour agrees with Eq. 3.28. According to Eq. 3.28, the bigger the sampling frequency, the smaller the maximum code phase error is, hence the difference between the maximum and minimum of the maximum correlation value decreases. The results presented sustain this argument because for the case in which the sampling frequency is bigger the normalized maximum correlation span is smaller. Hence, the demonstrator succeeds in reproducing qualitatively Eq. 3.28, as the normalized span is bigger for the case in which f_s=2.041 Msps than for the case in which f_s=8.333 Msps. However, the measured span does not match exactly the attenuation predicted by Eq. 3.28. Therefore, the demonstrator does not succeed in reproducing the quantitative behaviour of the code phase error. The theoretical behaviour is not reproduced exactly, hence random variations are effectively distorting the behaviour. This suggests that in order to correctly characterize behaviour, the empirical tests should be performed many times in order to reduce the experimental random variations. Bear in mind that according to the Monte-Carlo theorem, the variance reduces with the inverse of the square root of the experimental trials.

4.3.5 Configuration 5

Configuration 3 will be replicated in this case, but now the code phase behaviour is considered. The procedure included in the experiment for procedure 4 will be used. However, in this case just 50 different Galileo E1OS signals have been recorded. The results are displayed in Fig. 4.11.

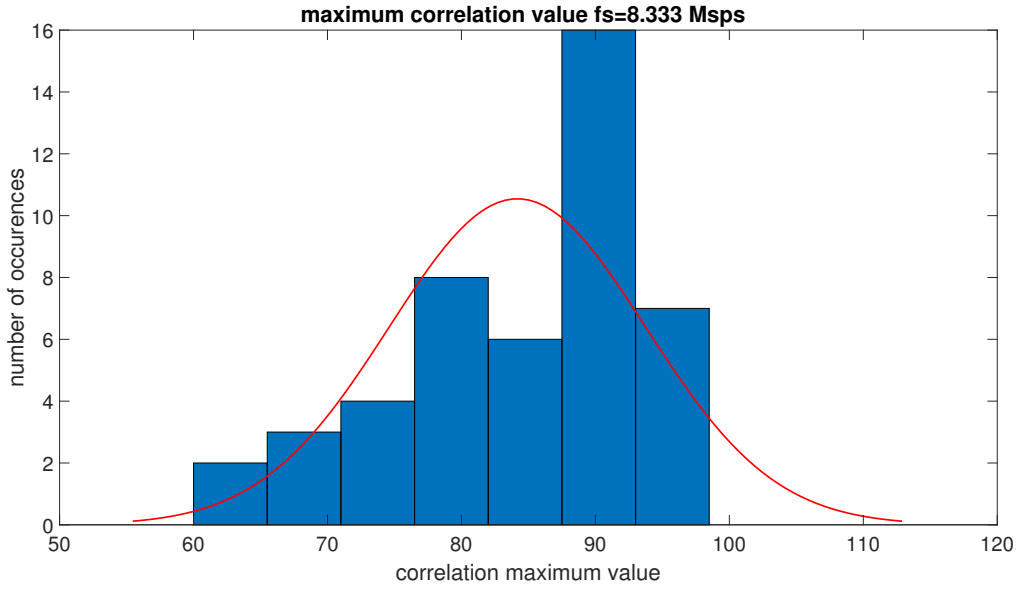

Figure 4.11: Histogram for correlation distribution for configuration 5.

The results show that the behaviour is similar to the one presented for the L1 C/A signals in configuration 4 because the margin between the maximum and minimum correlation value is close to the value than for the L1 C/A case study. Again, the demonstrator succeeds from a qualitative point of view but is unable to reproduce the quantitative behaviour of the code phase error as described in Eq. 3.28.

4.3.6 Figure of merit

This section will be devoted to presenting an ad-hoc figure of merit. The designed figure of merit intends to measure performance for signals whose strength is well above the detection threshold. The proposed figure of merit is defined as the quotient between the maximum of the correlation if the signal is present and the maximum value of the correlation peak if no signal is present. Detection is possible when the correlation peak is larger than the maximum, hence by measuring this quotient, a worst case comparison of the margin between the maximum correlation peak for the H_1 hypothesis and the maximum correlation peak for the H_0 hypothesis is obtained. A representation of the comparison between the correlation peaks under the H_0 and H_1 hypotheses is shown in Fig. 4.12. From Fig. 4.13, it is clear that the designed figure of merit reflects the magnitude of the detection margin when dealing with a high signal level case study.

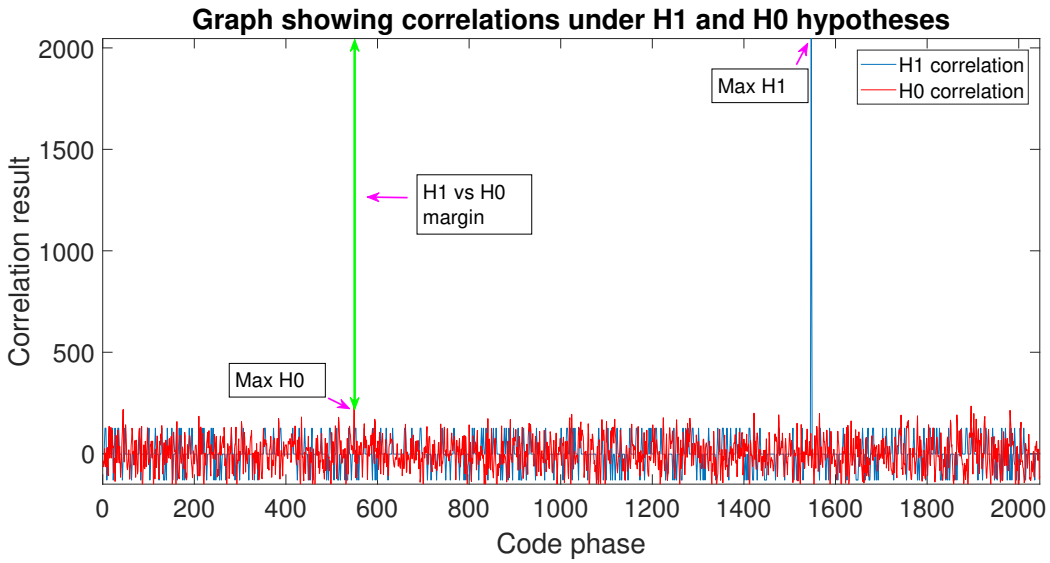

Figure 4.12: Designed figure of merit representation.

When measuring the detector performance, the most intuitive approach is to use the SNR. Nevertheless, as stated in [91], the receiver's output SNR cannot be used to fully characterize the receiver detector. A widely used figure of merit is the deflection

coefficient (which is the ratio between the square of the difference of the means under H_1 and H_0 hypotheses and the variance under H_0) as defined in [10, 75]. However, according to [75, 92] this detection metric cannot be used in cases in which receivers with decision statistics with different probability distributions have to be compared, as the comparison by means of the deflection coefficient magnitude can be misleading (as it fails in correctly comparing performance between different acquisition strategies). Another aspect to consider is the deflection coefficient paradox defined in [75] i.e., when using a detector in which the detection statistic is formed via a squaring operation, the deflection coefficient increases without increasing performance. This is another factor advising against the usage of this performance metric. Therefore, the deflection coefficient can only be used to compare the performance of a specific detector in different scenarios. This means that if one wants to measure the performance of different receivers in a specific scenario, the deflection coefficient cannot be utilized. A reliable procedure to measure detector performance is to use the ROC as in [76]. The ROC relates the detection probability, and the false alarm probabilities for a fixed signal strength. However, if for the simulated scenario, the input signal power is 47 dB/Hz, then the detection probability in absence of unwanted effects should very close to 1. Accordingly, there is a need to find a method to measure performance for different receivers under scenarios with different Doppler frequency signals. Considering this fact, the ROC curves and ROC based figures of merit such as the equivalent coherent SNR defined in [44, 93] cannot be used alone to measure detection performance in such scenarios, and some other performance metric must be used. An additional figure of merit aiming at measuring how much the detected signal stands out from noise is required.

The new figure of merit is obtained by comparing the maximum value corresponding to the correlation for the null hypothesis H_0 (no signal present), with the maximum value of the correlation for the H_1 hypothesis (signal present). The maximum value for H_0 is obtained by correlating the signal with a local code which is not broadcasted by any satellite. In this way, the margin separating the H_0 and H_1 hypotheses is measured. The bigger the margin is, the easier it is to distinguish between the two hypotheses. This figure of merit can be defined as a worst-case figure of merit because it does not use the mean value of H_0 for the comparison. Instead, it uses the maximum value of H_0, establishing a harsher comparison criterion. This specific figure of merit is especially designed to deal with cases in which the signal level is high enough, but empirical tests to measure the effects of residual effects are to be conducted. Hence, a tool to measure performance in such tests is provided.

A comparison between the designed figure of merit and the performance of configuration 1 will be conducted. A graph showing the great degree of correlation between the maximum correlation and the designed figure of merit is presented in Fig. 4.13.

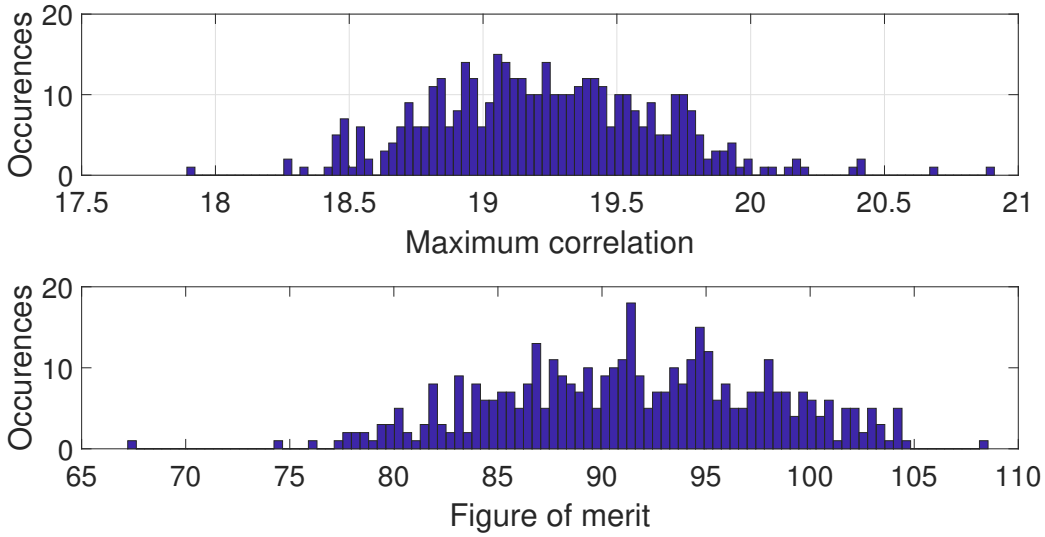

Figure 4.13: Figure of merit vs maximum correlation.

It is clear that the designed figure of merit succeeds in reproducing the behaviour of the maximum correlation value. Moreover, at the same time, the maximum value for the H_0 hypothesis is taken into account. Hence, the designed figure of merit succeeds in storing information of both hypotheses. From one side, the figure of merit follows a similar distribution as the maximum correlation value (see Fig. 4.13). However, at the same time, the designed figure of merit contains information from the H_0 hypothesis.

The capability of storing information for both hypotheses, is the feature that makes the difference between the output SNR and the figure of merit. The output SNR only includes information on the H_1 hypothesis, whereas the designed figure of merit includes information for both hypotheses.

A specific figure of merit has been designed and its performance has been measured proving its adequateness for the empirical studies performed.

Chapter 5

Pre-correlation detector for LEO satellite embedded receiver

5.1 Introduction

The aim of this chapter is to carry out a study to describe (quantitatively) the behaviour of the pre-correlation detector within a LEO scenario. In light of the points presented in chapter 3 (Eq. 3.25) or in [67], when designing a GPS receiver for LEO space applications, the Doppler frequency search space must be adapted to be able to detect the satellite signal. The code Doppler effect must be taken into consideration too, as stated in [5, 94] or as can be inferred from the code attenuation as shown in Table 3.2. Studies dealing with LEO GNSS receivers such as [6], present a standard non-coherent acquisition method in order to successfully tackle the problem. In [30], a computationally efficient method based on [64] is applied for the case of GPS and Galileo signals. Both the standard and the computationally efficient approaches successfully deal with solving the problem. Nevertheless, the computationally costly Doppler frequency search is still performed. In the analysis presented in this chapter, the usage of the differential detector is considered. This detector type need not perform a Doppler search [9, 10], and this is why this detector is considered to perform the best in terms of sensitivity to dynamics. In [95], it is stated that the major drawback in the usage of this detector, is the fact that a longer integration time (in comparison to other detectors), is required to acquire signals. However, in a LEO scenario, the signal level is generally high and it is appealing to take advantage of the higher acquisition threshold. A proof of concept

study in order to respond if the pre-correlation differential detector performs as expected in a realistic simulation environment is to be performed. The receiver sensitivity to input Doppler frequency and data modulation is measured and hence the performance of the pre-correlation differential receiver/detector is assessed. Some different implementations of the detector are studied to investigate if these forms help in improving the performance of the baseline pre-correlation differential detector. These detectors are characterized in a statistical fashion. The distinct implementations will differ in the way in which the decision statistic is formed. The performance is measured by means of an ad-hoc figure of merit. The speed-up achieved using the pre-correlation differential detector, instead of the standard baseline non-coherent receiver, is quantified. Moreover, a method which is not computationally burdensome is tested to provide an estimate of the Doppler frequency.

5.2 Baseband signal model

To fully understand the effects of a GNSS signal in a high dynamic platform, a baseband signal model (the signal is down-converted and the f_{L1} frequency is eliminated), is presented. This model is only valid for small integration times, as it is assumed that the Doppler carrier and code are constant when the integration time is small. The signal model is the one used in [9]. The model only considers the signal transmitted by one satellite, because it is a suitable assumption for this study. The near-far effect will not be studied in this work.

A specific signal model for the C/A signal is presented below after baseband conversion, is presented in Eq. 5.1.

$$s(nT_s) = \sqrt{P(nTs)}C(nT_s - \zeta T_{chip})e^{j(w_d nT_s + \theta_k)} + n_w(nT_s). \tag{5.1}$$

Where:

T_s: Sampling period.
n: Number of signal sample.
D: Data signal whose repetition period is 20 ms.
P: Signal power (158.5 dBW [55]).
C: GPS L1 C/A Gold code.
T_{chip}: Chip period.
w_d: Signal Doppler angular frequency.
θ_k: Signal carrier random phase.
ζ: Code phase offset.
n_w: Function modeling the channel's additive Gaussian noise.

According to [6] and [9], $n_w(nT_s)$ can be described using a complex normal distribution, composed of a real and an imaginary part, which are jointly normal and independent. For the coherent and non-coherent detectors, the receiver evaluates how well each of the possible frequency-phase combinations estimates the GNSS signal parameters. In this way, a two-dimensional search space is formed as illustrated in Fig. 5.1 (a). The pre-correlation differential detector only needs to search the code phase space, so just a one-dimensional search space (Fig. 5.1 (b)) must be explored instead of a two-dimensional search.

The parameters involved in the 2-D search space are the following:

1. ζ: Code phase offset, which is one of the parameters in the search space.
2. f_d: Doppler frequency, which is one of the parameters in the search space.
3. $\Delta\zeta$: Code search spacing, i.e. the step used in exploring the code phase search space.
4. Δf_d: Doppler frequency search spacing, i.e. the step used in exploring the Doppler frequency search space.

The interest in studying the pre-correlation differential detector arises from the fact this type of detector as defined in Fig. 5.2 need not explore the frequency search space to detect the presence of a GNSS signal, as illustrated in Fig. 5.1 (b). From the study performed in chapter 3, it is possible to extract that the computational cost associated to the acquisition process in the LEO scenario is ten times bigger than the computational cost for an earth-based scenario (for the coherent detector with $M = 2$ to limit the Doppler attenuation factor to 0.8751). This fact is particularly interesting in a situation in which the Doppler search space is wide. In these wide Doppler search space scenarios, the use of this type of receivers is interesting because a great reduction in the computational burden associated to the acquisition process can be achieved.

In an analogous manner as for the detectors studied in chapter 3, residual effects are a key aspect affecting the pre-correlator detector performance. These effects have not been analyzed thoroughly in previous works but will be studied in this work. Accordingly, this is one of the main contributions of this work. The focus is set on quantifying how much these factors affect the receiver performance in this case. Just in the same way as for the other detector types, the effect of the following factors is studied:

1. Doppler carrier frequency.
2. Residual phase offset.

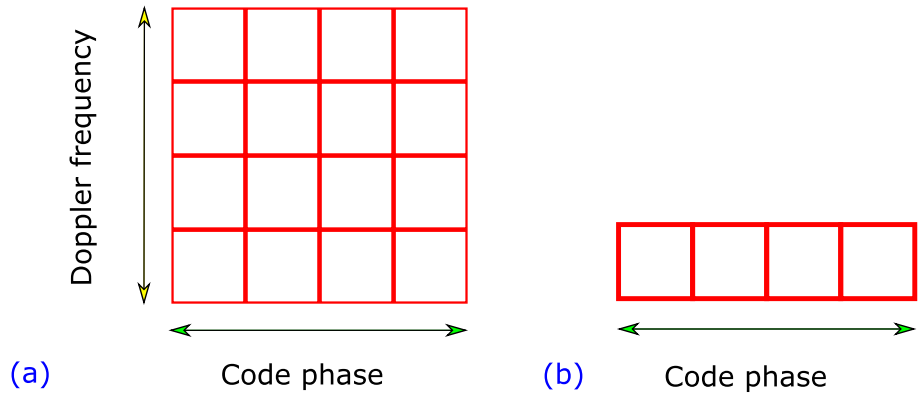

Figure 5.1: Acquisition grid complexity reduction

3. Data modulation.

A statistical analysis to compare groups of signals with different Doppler frequencies, and groups whose signals are modulated or not modulated by GPS data navigation information, is performed. By studying the aspects affecting the receiver performance, the receiver usage suitability for the case study can be assessed.

5.3 Receiver working principle and general aspects

5.3.1 Working principle

The block diagram of the pre-correlation detector is presented in Fig. 5.2 (Type 1 detector). This receiver appears as the pre-correlation differential detector in [10], as the differentially coherent detector in [9] or as the pre-detector differential scheme in [96]. The 'delay and multiply method' in [5] and [97] relies on the same concept but works with an IF signal, instead of a baseband signal. More recently, this detector type has been used to circumvent the ambiguity arising from the multiple correlation peaks for the BOC [98].

The input signal is delayed an integer number of samples (J), and correlated with a Gold code generated as the product of two Gold codes. Finally, the decision statistic is formed by taking the real part of the correlation. N_s is the number of samples in one C/A code period and M is the number of C/A code periods combined. The working principle of this type of detector is based on the well-known Gold codes (defined in [99,100]), 'delay and multiply' property [5]. When multiplying a Gold code by a shifted version of the same Gold code, the result of the product is a Gold code itself. This property holds for any Gold code [3, 5, 9, 96, 99]. As stated in [95], there is a subtle difference between the 'delay and multiply' method and the pre-correlation differential receiver/detector. The difference is that the pre-correlation differential receiver works on zero-IF (zero intermediate frequency)

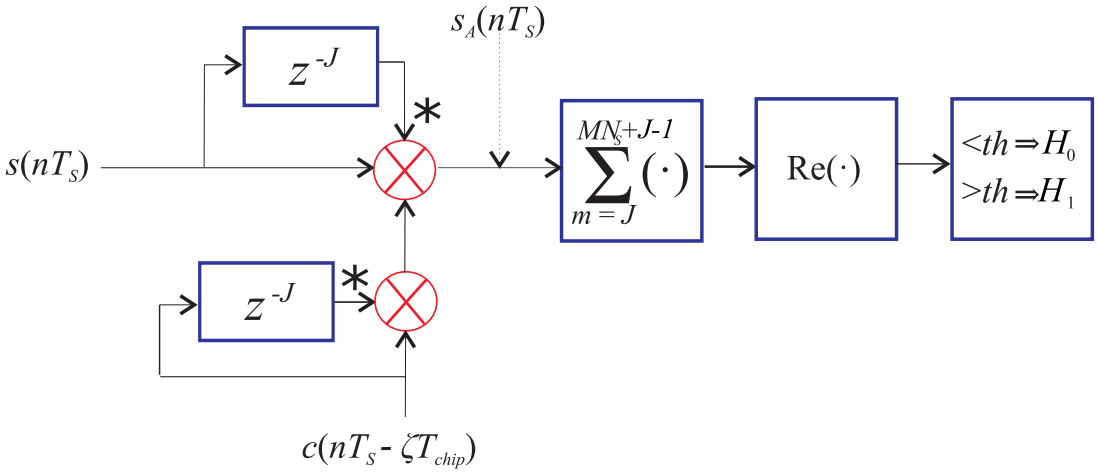

Figure 5.2: Pre-correlation differential detector (Type 1 detector).

signals, whereas the 'delay and multiply' approach uses the receiver working principle to eliminate both the Doppler frequency drift and the IF. If the input signal can be expressed in the same way as in Eq. 5.1 and if the noise term is ignored, when analyzing the signal labelled as s_A in the diagram, it can be deduced that s_A can be obtained by multiplying a shifted and conjugated version of the input signal by the input signal. Mathematically, the resulting product can be expressed in the following manner:

$$s_A(nT_s) = s(nT_s)s^*(nT_s - \tau). \tag{5.2}$$

Where $\tau = JT_s$ is the time shift applied to the input signal.

Recalling Eq. 5.1, ignoring the noise, carrier phase and power terms and considering an observation interval in which the navigation data terms do not change, we have:

$$s(nT_s) = C(nT_s - \zeta T_{chip})e^{jw_d nT_s}. \tag{5.3}$$

In an analogous manner:

$$s^*(nT_s - \tau) = C(nT_s - \tau - \zeta T_{chip})e^{-jw_d(nT_s - \tau)}. \tag{5.4}$$

Substituting $\tau = JT_s$ in Eq. 5.2 (which is the product of expressions Eq. 5.3 and Eq. 5.4 and evaluating the part of the equation in which complex exponentials are multiplied,

we have:

$$e^{jw_d nT_s} e^{-jw_d(nT_s-\tau)} = e^{jw_d\tau}. \tag{5.5}$$

The resulting product is a constant, because w_d and τ can be considered to be constant when analyzing small observation intervals (this means the assumption will hold when working with small integration times). The fact the product is constant with time implies that it is not necessary to perform a frequency search process to detect the GPS signal because $e^{jw_d\tau}$ is a constant factor with no frequency information. The result of evaluating the code product is expressed mathematically in Eq. 5.6.

$$C(nT_s - \zeta T_{chip})C(nT_s - \tau - \zeta T_{chip}) = C_{new}. \tag{5.6}$$

These new codes, are Gold codes, according to the Gold code 'delay and multiply' property. The correlation peak is placed in the exact same position as in the original code [5]. The theoretical aspects presented, show that the pre-correlation detector does not need to perform a Doppler space search to detect the presence of the GPS signal. Therefore, the detector can be implemented with no further calculations, as the correlation peak appears in the same exact position. To quantify how well the pre-correlation differential detector (with a FFT implemented correlation) performs in reducing the computational cost, first the computational cost of the standard non-coherent detector over one period, and using the FFT implementation, is evaluated. The non-coherent detector is used for the comparison as it simple and widely used. The block diagram of the non-coherent receiver implemented using the FFT to calculate the correlation, is as shown in Fig. 3.12 in chapter 3.

If just 1 ms of signal is processed, and considering a Doppler search span of 100 kHz, using a Doppler frequency step of 100 Hz and being N_s the number of signal samples in 1 ms, then the number of operations is:

$$1000 \times (2N_s \text{ complex products } + \ 2N_s \text{ sized FFT}) \tag{5.7}$$

The fact (100 kHz/100 Hz) =1000, implies that 1000 frequencies must be explored. This is considered when a factor of 1000 is included in the expression to calculate the number of operations to be performed to process 1 ms of signal. When examining the block diagram of the pre-correlation differential detector Fig. 5.2, it can be seen that just two FFT operations and two complex multiplications are performed. Therefore, the

operation count for this detector is:

$$2N_s \text{ complex products } + 2N_s \text{ sized FFT} \tag{5.8}$$

At this point, it is important to highlight that one of the shortcomings of this detector is that a Doppler frequency estimation is not obtained. In standard tracking loops, the Doppler frequency must be a known parameter. If no Doppler frequency estimate is available, a tracking loop that implements a differentially coherent tracking loop like the one presented in [101], must be used. In [3, 10], the fact no Doppler frequency estimation is obtained is considered an important shortcoming hindering the usage of this type of detector. However, as explained in [102], it is possible to overcome this problem. Using the PFS technique [70], once the correct signal phase offset is obtained, the Doppler frequency can be calculated by multiplying the input signal by a C/A code whose phase has been shifted the same number of phases as the input signal's phase offset. Once this product is obtained, the FFT of the product is calculated and a peak in the corresponding Doppler frequency appears, as the spectrum has been unspreaded. After the unspreading process, the original C/A code and carrier signal will only contain the original carrier signal. In the case the signal Doppler frequency value is required, the additional computational cost is not too large, as just an additional FFT and an additional complex multiplication are required.

The final computational cost is:

$$3N_s \text{ complex products } + 3N_s \text{ sized FFT} \tag{5.9}$$

Since not much computational is added if the Doppler frequency estimation is performed in this fashion, and no more complexity is added in the tracking loop, it is advisable to use the above-mentioned frequency estimation technique.

5.3.2 Input Doppler effect on performance

The feature that motivates the usage of the pre-correlation differential detector is the fact it performs in the same way, no matter the Doppler frequency shift of the input signal. Therefore, it is important to study to which extent and under which assumptions this is true. According to the mathematical statements included in [9], the expression describing the attenuation caused by the Doppler frequency of the input signal and the time delay

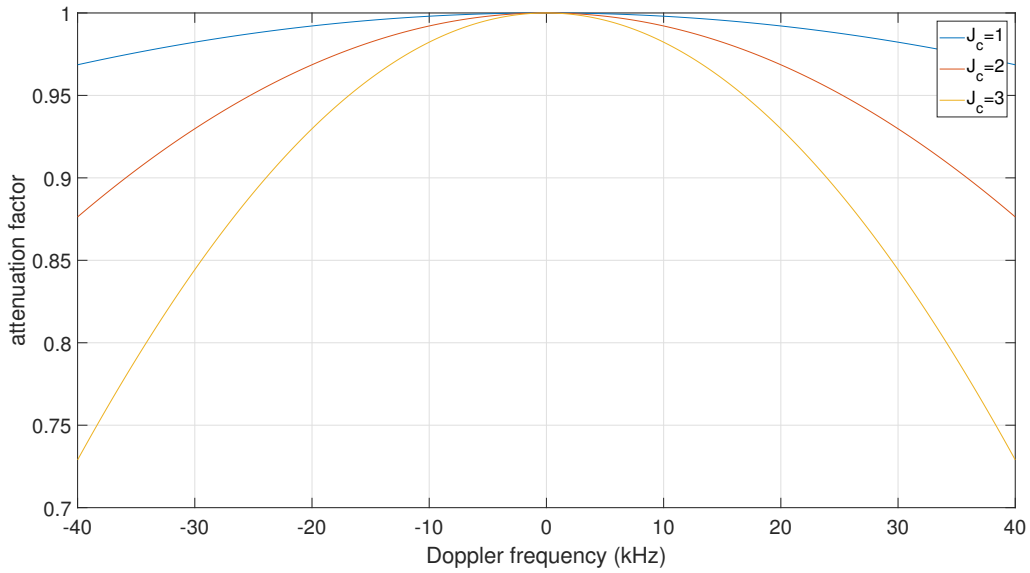

Figure 5.3: Pre-correlation differential type 1 detector attenuation for different values for J_C and Doppler frequency.

applied in the type 1 pre-correlation differential operation, is ilustrated in Eq. 5.10.

$$AtDop - pre(f_d) = \frac{\cos(\frac{2\pi J_c f_d}{1000})}{L}, \tag{5.10}$$

where J_c represents the number of chips the input signal is shifted, L=1023 (number of chips of the C/A code), $f_d/1000$ is the value of the Doppler frequency of the input signal in kHz. The expression Eq. 5.10 is plotted in Fig. 5.3, including different values of J_c. From Fig. 5.3, it can be inferred that the attenuation increases as J_c increases and that the attenuation increases too as the Doppler frequency increases. As explained in [9], a necessary condition for the pre-correlation differential detector to work is to apply shifts corresponding to an integer number of chips. In the detector implementation studied in this work, a value of $J_c = 1$ (which corresponds to a value of J=2, if the sampling frequency is twice the chip frequency) is used, as this is the smallest value for J_c.

For J_c=1, the attenuation is negligible for Doppler values below 10 kHz, and an input Doppler bigger than 40 kHz is needed for an attenuation larger than 3% to happen.

5.3.3 Residual phase error effect on performance

The residual code phase error happens when the estimate for the code phase obtained in the acquisition process does not match the actual code phase. The residual code phase error is the error that affects the receiver performance the most (especially when the sampling frequency is not high) and it does so in a random fashion. In [9], it is pointed out that as long as the quotient $\frac{f_d}{f_{L1}}$ is close to 0 (in the order of 10^{-5}), the input to the coherent accumulator is the product of two Gold codes. Consequently, the pre-correlation differential receiver behaves in the same way as the coherent detector when considering the residual phase offset. The maximum phase offset error caused by this effect can be quantified recalling the expression provided in Eq. 5.11 (which is exactly the same expression that describes this effect for the coherent detector as in Eq. 3.26).

$$\Delta\tau_{max} = \frac{L}{N_s} \tag{5.11}$$

Being L=1023 (number of chips of the C/A code), and for the experiments with the pre-correlation detector, the sampling frequency used will be 2.041 Msps (this small value is used to minimize the computational cost). When using this sampling value, the quotient $\frac{L}{N_s}$ is approximately 0.5. The actual expression that describes the attenuation caused by this effect is given in Eq. 5.12 and is the same as the expression for the attenuation for the coherent detector.

$$Att_{code-pre} = 1 - \frac{L}{N_s} \tag{5.12}$$

If the sampling frequency is 2.041 Msps, the maximum attenuation is close to 50% of the original value. In a LEO scenario, the code Doppler drift is not negligible. In this scenario, it is advisable to use code compensation. Code Doppler compensation will be implemented in the upcoming tests.

5.4 Data modulation effect

The pre-correlation differential detector/receiver is not affected by the data modulation effect, and a qualitative reasoning can be used to sustain this argument. When analyzing how the signal $s_A(nT_s)$ in Fig. 5.2 is formed, it can be noted that the signal is obtained by multiplying the input signal by a shifted version of the same signal, so when a phase reversal occurs in the input signal, the phase reversal will only affect one sample, as the other samples involved in the product operation will always have the same phase sign. Considering this reasoning (if $f_s = 2.041$ Msps, $N_s = 2041$), just one sample out of 2041

samples of the resulting product is affected by the data modulation effect and therefore it can be stated that the pre-correlation differential detector/receiver is not affected by the data modulation effect. Nevertheless, this statement is not only true if J is small. However, J must be small for the pre-correlation detector to avoid severe attenuation as ilustrated in Eq. 5.10. The same reasoning is included in [9, 10]. The immunity against the data modulation effect of the detector is demonstrated in the experiment al part of this work.

5.5 Noise analysis

For the noise analysis, the product $s(nT_s)s^*(nT_s - \tau)$ must be examined. For simplicity, we ignore the data signal (which can be assumed to be constant for this analysis).

We recall here that $n_w(nT_s)$ follows a Gaussian distribution with power σ_n^2 $N(0, \sigma_n^2)$. The signals involved are:

$$s(nT_s) = \sqrt{P}C(nT_s - \zeta T_{chip})e^{jw_d nT_s} + n_w(nT_s), \tag{5.13}$$

$$s^*(nT_s - \tau) = \sqrt{P}C(nT_s - \zeta T_{chip} - \tau)e^{-jw_d(nT_s-\tau)} + n_w^*(nT_s - \tau). \tag{5.14}$$

The multiplication of both terms yields:

$$s(nT_s)s^*(nT_s - \tau) = S_{sig} + S_{n1} + S_{n2} + S_{nn} \tag{5.15}$$

Where

$$S_{sig} = PC(nT_s - \zeta T_{chip})C(nT_s - \tau - \zeta T_{chip})e^{jw_d\tau} \tag{5.16}$$

$$S_{n1} = \sqrt{P}C(nT_s - \zeta T_{chip})n_w^*(nT_s - \tau)e^{jw_d nT_s} \tag{5.17}$$

$$S_{n2} = \sqrt{P}C(nT_s - \tau - \zeta T_{chip})n_w(nT_s)e^{jw_d(nT_s-\tau)} \tag{5.18}$$

$$S_{nn} = n_w(nT_s)n_w^*(nT_s - \tau) \tag{5.19}$$

The terms $e^{jw_d(nT_s)}$ and $e^{jw_d(nT_s-\tau)}$, when multiplied by noise, cause a complex rota-

tion in the noise components, which does not affect their probability density functions [9] and hence will be ignored. The terms S_{n1} and S_{n2} are zero-mean Gaussian noise terms with power σ_n^2, because if $n_w^*(nT_s - \tau)$ or $n_w(nT_s)$ are multiplied by a C/A code, the noise power remains unchanged [103].

At the correlator input, the quotient between the signal and noise components is:

$$SN_{prec} = \frac{PC(nT_s - \zeta T_{chip})C(nT_s - \tau - \zeta T_{chip})e^{jw_d\tau}}{S_{n1} + S_{n2} + S_{nn}}. \tag{5.20}$$

Recalling equation Eq. 5.20 and using the fact $e^{jw_d\tau} \approx 1$, Eq. 5.20 transforms into:

$$SN_{prec} = \frac{\sqrt{P}C_{new}(nT_s - \zeta T_{chip})}{\frac{S_{n1}+S_{n2}+S_{nn}}{\sqrt{P}}}. \tag{5.21}$$

S_{n1} and S_{n2} are the products of shifted noises and C/A codes, and are hence, uncorrelated due to the fact white Gaussian noise is uncorrelated. The noise product term S_{nn} is uncorrelated with the C/A term S_{n1} and S_{n2} contain. Considering S_{n1}, S_{n2} and S_{nn} are uncorrelated processes, the sum of the variances is equal to the variance of the sum of the three processes.

The noise power of the denominator in Eq. 5.21 is

$$E\left[\left(\frac{S_{nn} + S_{n1} + S_{n2}}{\sqrt{P}}\right)^2\right] = \frac{1}{P}(E[S_{nn}^2] + E[S_{n1}^2] + E[S_{n2}^2]) \tag{5.22}$$

S_{nn} is the product of two independent Gaussian distributions. According to [104], S_{nn} follows a normal product distribution with variance σ_n^4.

$$E\left[\left(\frac{S_{nn} + S_{n1} + S_{n2}}{\sqrt{P}}\right)^2\right] = 2\sigma_n^2 + \frac{\sigma_n^4}{P} \tag{5.23}$$

Clearly

$$2\sigma_n^2 + \frac{\sigma_n^4}{P} > \sigma_n^2 \tag{5.24}$$

Which means that the signal to noise ratio at the input of the correlator is smaller for the pre-correlation detector than for any detector that does not perform the 'delay and multiply' operation.

For any pre-correlation detector, the noise at the input of the correlator is:

$$2P\sigma_n^2 + \sigma_n^4 \tag{5.25}$$

At the correlator output the noise power σ_{pre}^2 is:

$$\sigma_{pre}^2 = (MN_s)(2P\sigma_n^2 + \sigma_n^4). \tag{5.26}$$

For the type 1 pre-correlator when forming the decision statistic using the real part, the signal power remains unchanged if $e^{jw_d\tau}$ is close to 1.

However, after taking the real part of the signal, the signal power is divided by two.

$$\sigma_{det}^2 = (0.5MN_s)(2P\sigma_n^2 + \sigma_n^4). \tag{5.27}$$

The decision statistic is formed by accumulating independent variables, hence by invoking the Central limit, the resulting distribution can be assumed to be Gaussian under both H_0 and H_1 hypotheses [103].

Under H_0 the decision statistic follows a zero-mean Gaussian distribution $N(0, \sigma_n^2)$ Under H_1 the decision statistic follows a non-zero mean Gaussian distribution $N(\mu, \sigma_n^2)$

Where

$$\mu = MN_sP \tag{5.28}$$

The probability of false alarm and the detection probability are given by

$$P_{fa} = \frac{1}{2}\text{erfc}\left(\frac{th}{\sqrt{2\sigma_{det}^2}}\right) \tag{5.29}$$

$$P_d = \frac{1}{2}\text{erfc}\left(\frac{th-\mu}{\sqrt{2\sigma_{det}^2}}\right) \tag{5.30}$$

Where th is the decision threshold and erfc is the complementary error function.

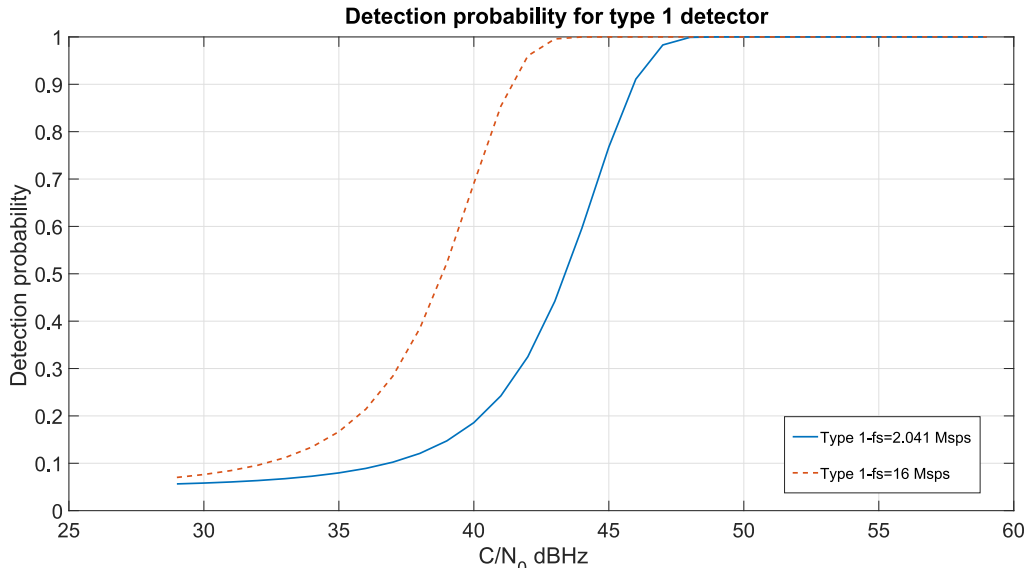

Figure 5.4: Detection probability graph for a 10 ms integration time and different sampling frequencies. PFA=0.02.

The erfc is defined as 1-erf, where erf is the error function. The expression for the erfc is presented in Eq. 5.31, as defined in [105].

$$\text{erfc(z)} = \frac{2}{\sqrt{(\pi)}} \int_z^{\infty} e^{-t^2} dt. \tag{5.31}$$

Two detection probability traces for a false alarm probability of 0.02 traces are shown. Referring to Eq. 5.4, the continuous trace shows the detection probability for the proposed sampling frequency, whereas the dotted line shows detection probability if a times 8 oversampling scheme is used. Performance increases at the expense of an increased computational cost. The theoretical analysis for the selected configuration, provides the information to perform an empirical test.

5.6 Receiver architecture types

The pre-correlation differential detector can be implemented in different manners because it is possible to generate the decision statistic in diverse ways. The decision statistic is formed using only the real part of the correlation result, or generating the statistic using the modulus. A hybrid detector is studied too, as the decision statistic is formed in a differential fashion, by combining correlation results from different C/A periods. These

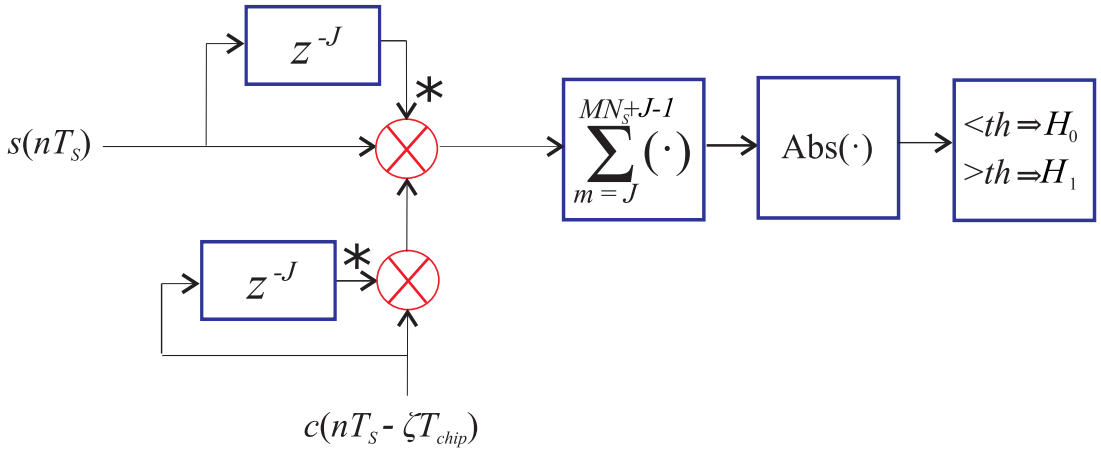

Figure 5.5: Type 2 detector.

detectors are studied in order to find out if slight implementation changes improve the detector performance.

5.6.1 Type 1 receiver

The type 1 receiver is considered the baseline receiver Fig. 5.3, upon which, others are formed by applying slight modifications. The decision statistic is formed by taking the real part of the correlation result, because the correlation output function describing the attenuation caused by input's signal Doppler frequency depends on the term $e^{jw_dT_sJ}$ When the argument of this attenuation function is small, the imaginary part of the term is close to zero, and there is no need to use the imaginary part to form the decision statistic. However, if the Doppler frequency increases some energy moves to the imaginary part. The decision statistic is found to follow a zero mean Gaussian distribution under the H_0 (no signal present) hypothesis and a non-zero mean Gaussian distribution under the H_1 (signal present) hypothesis. This is explained by the fact the decision statistic is formed by taking the real part of the correlation.

5.6.2 Type 2 receiver

The type 2 receiver is a modified version of the classical pre-correlation differential receiver. In this case, the decision statistic is formed by taking the modulus of the correlation result.

Examining the product w_dT_s, it is important to consider that for an earth-based user, w_d takes values of tens of rad/s and T_s takes values of microseconds, then it follows that the product must have a small value. However, in a high dynamic GNSS scenario as the one studied in this work, the values of w_d are 10 times larger than the values of w_d in an earth based receiver and the argument of $e^{jw_dT_sJ}$ is 10 times larger. As the

value of w_d gets larger, more energy moves to the imaginary part of the exponential and it might be interesting to use the imaginary part to form the decision statistic as proposed in [9]. Therefore, it is interesting to study if in a high dynamic scenario, type 2 receiver, outperforms type 1 detector (lets recall at this point the fact that for type 1 detector, the decision statistic is formed using the real part of the correlation and this reduces the noise power). The distribution of this detector is found to follow a Rayleigh distribution under the H_0 hypothesis and a Rice distribution under H_1. This fact is consistent with the theoretical argument included in [76]. This argument sustains that a Rayleigh distribution is obtained when the absolute value (magnitude) of a complex number whose components are Gaussian is calculated. When the magnitude operation is applied to non-zero Gaussian variables, the distribution changes from a Rayleigh to a Rice distribution.

5.6.3 Type 3 and 4 receivers

In [95], the Doubly-differential detector is presented. Type 3 and 4 detectors are implemented using this approach. The Doubly-differential detector consists in a pre-correlation differential operation like in type 1 and 2 detectors, followed by a post-correlation multiplication of 1 ms separated correlation outputs (recall from section 3.4.4.3 that $J \cdot M < 2$). For a type 3 detector, the decision statistic is formed using the real part of the correlation result, whereas for type 4 detector the decision statistic is formed using the modulus of the correlation result. In Fig 5.6, type 3 and 4 detectors are represented. Type 4 detector is identical to type 3 detector, except in that the decision statistic is formed using the modulus instead of the real part. The output correlations are obtained in the same fashion as for type 1 and 2 detectors, but one of the correlations is delayed MN_s samples (LT_{chip} seconds) with respect to the other. The final decision statistic is formed by multiplying two delayed correlation outputs. This detector design pursues a reduction of the noise interfering in the decision statistic. According to [72], the signal components should be correlated, whereas the noise components should be independent. Using this procedure, the correlation peak value should not be affected and the noise should be reduced. However, in a high-dynamics environment, the fast time-varying Doppler shift implies the performance decreases in a significant manner. This behaviour is described in section 3.4.4.3. Furthermore, the post correlation differential product introduces more noise terms in the same way the pre-correlation operation does. Hence, this detector should perform worse. This hypothesis is studied using statistical comparisons of simulation results. To deduce the decision statistic distributions for type 3 and 4 detectors, the same analysis as for type 1 and 2 detectors is performed. For the type 3 detector, the decision statistic distribution is found to follow a Gaussian distribution, whereas for type 4 the decision statistic follows the same distributions as for type 2.

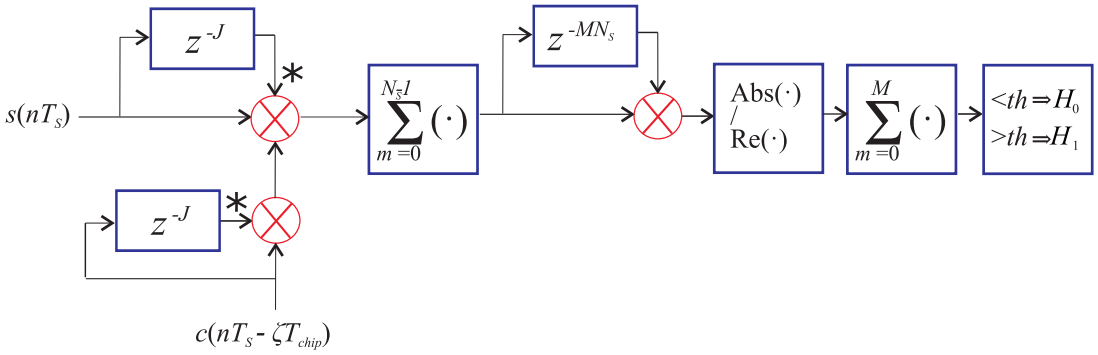

Figure 5.6: Type 3 and 4 detectors.

It is interesting to point out, that a detector based on the pre-correlation differential detector is implemented in [10], using the pre-correlation differential detector preceded by a coherent detector. In fact, the author states that this receiver improves performance by improving the receiver sensitivity for low signal level scenarios. Furthermore, in [10], the author aims to design a detector with the pre-correlation differential detector immunity to Doppler, data modulation effects, and the coherent detector sensitivity performance. In the LEO case study, the detector sensitivity is not a major issue and thus the study of the detector sensitivity is no longer not considered in this analysis.

5.7 Methodology

5.7.1 General aspects

The theoretical aspects presented are validated using a SDR philosophy to implement receiver architectures. The setup referred to as Configuration 1 in chapter 4 will be employed for this case study. Nevertheless, instead of working with a validation earth-based scenario, now the Spirent GSS7700 GNSS signal generator is used to generate the GPS signal for a receiver embedded in a LEO satellite, using the following configuration:

- Full L1 C/A constellation in which the Doppler frequency changes.
- The receiver is placed in a 1000 km LEO.
- Variable received signal power (depending on the simulated dynamic behaviour of the vehicles in the scenario).

Throughout this experiment, the flexibility of the SDR philosophy will be fully exploited as the different MATLAB routines will implement the different detectors/receivers under test The study will start by measuring the performance of the acquisition process for a non-coherent receiver/detector. The results obtained in this baseline case are used to

compare the figures of merit of the detectors under study. For the baseline, non-coherent detector, a Doppler frequency search spanning from [-50 kHz to 50 kHz] must be explored. A Doppler frequency search step of 10 Hz is used (this search space is used to minimize the effect of the residual Doppler frequency). Bear in mind that as explained in chapter 3, for the non-coherent detector a 10 Hz residual Doppler (with M=1 and $f_s = 2.041$ Msps) the Doppler attenuation factor is 0.9997, which translates into a 0.0013 dB loss.

Considering that the pre-correlation detector is a promising technique regarding execution time speed, it is interesting to find out if the detector performance in the LEO GNSS receiver study is acceptable, for different Doppler frequency conditions.

5.7.2 Statistical analysis description

The final aim of the statistical analysis, is to detect significant differences in the performance of different detectors and to detect if the performance of a specific detector changes when processing signals with different mean Doppler frequencies or when processing signals that have been modulated by GPS data or signals that have not been modulated. The data is arranged in 5 different sets formed by 600 GPS signals. Each set is characterized by its own mean Doppler frequency. In order to fully characterize the scenario, it is necessary to repeat the experiment by storing the signal the same number of times as the experiment is repeated, obtaining statistical distributions that can characterize the receiver's behaviour for the case studied. This procedure allows to compare the performance for different Doppler frequencies and to study the effect of data modulation. The data used is described in a more specific manner now. Each of the 5 sets of 600 signals, can take one of the following mean Doppler frequencies: 0 Hz, -18 kHz and -30 kHz. (Groups 1, 2 and 3 respectively). Groups 1a and 3a correspond to the Doppler frequencies 0 Hz and -30 kHz, but the signals included in the groups 1a and 3a have been modulated by a GPS navigation data signal. By comparing group 1 with group 1a and group 3 with group 3a, the effect of data modulation can be characterized. The comparison procedure consists in calculating the mean and standard deviations for the figures of merit of each of the 600 signal groups. Using probability density functions and the mean and standard deviation, it is possible to determine if performance changes for different receiver implementations and for different signal conditions. Comparisons between receiver/detector architectures, mean Doppler frequency groups and modulated and non-modulated signals are carried out. The figure of merit obtained after processing each signal forming part of each particular Doppler set, is arranged to obtain the probability density functions which characterizes the performance of a specific Doppler group. For each type of detector under test, the Doppler frequency groups are compared. In this way, the detector behaviour under different Doppler scenarios is characterized. Using a fixed Doppler frequency, the distributions formed by the figures of merit for each method are compared. In this way,

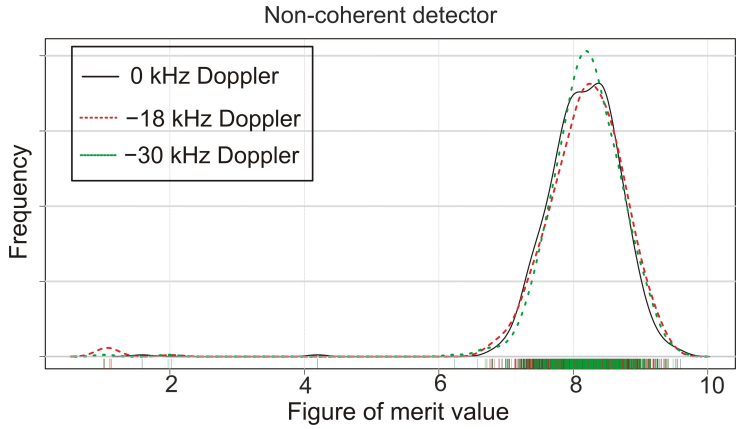

Figure 5.7: Decision statistic distribution for the figure of merit of the three Doppler frequency groups for the non-coherent detector.

the performance of the detector under test can be studied. The other important aspect to be studied is the execution time for each receiver. The execution time for the different acquisition algorithms is measured and compared. The differences are studied to validate the theoretical statement that asserts that the pre-correlation differential detector execution time is remarkably smaller than the execution time for the baseline non-coherent algorithm.

5.8 Results

In this section different results regarding experiments aiming to characterize the receiver behaviour under the factors affecting the detector performance (signal impairments), are presented.

5.8.1 Non-Coherent detector (non-modulated signal)

First, the performance results for the 3 Doppler frequency groups for the non-coherent detector are presented for the dataset of signals that are not data modulated. A 10 ms integration time is used. The figure of merit for all the signals contained in each of the 3 Doppler frequency groups is calculated. The mean and the standard deviation of each of the 3 Doppler groups are presented, and the probability distribution functions for the three groups are examined. In Table. 5.1 , the values for the mean and standard deviation of the 3 groups are shown, using the non-coherent detector with a frequency search step of 10 Hz. The receiver code replica chip frequency has been adjusted taking into account the code Doppler effect. The probability distributions for the three Doppler frequency groups, are obtained and shown in Fig. 5.7.

When analyzing Fig. 5.7, it important to highlight that the signals do not contain GPS data and that the attenuation caused by the Doppler frequency residual error is negligible as the Doppler frequency search bin used in this case is 10 Hz, and a 10 Hz residual Doppler results in a negligible attenuation [9, 10, 30]. Hence, the only effect (if the noise level is kept constant) that can affect the signal's figure of merit is the residual code offset error. The variability is large, and this is explained by the fact the sampling frequency is close to twice the code chip frequency. The points showing a figure of merit whose value is <2 are outlier points coming from experiments in which no signal was recorded. In fact, as stated in Eq. 3.28, when the sampling frequency is twice the chip frequency, an attenuation of 50% of the theoretical value can be obtained. As expected, the figure of merit shows that performance is similar for the three Doppler frequency groups. The execution speed is assessed by measuring the non-coherent acquisition execution time, 1000 times for each of the 600 signals integrating a Doppler group. The mean execution time is used as the estimator of the execution time. A 100 Hz frequency search step is used in this case (instead of the 10 Hz frequency search step used to obtain the figure of merit) and the Doppler search space spans from [-50 kHz to 50 kHz]. A 100 Hz frequency search step has been used instead of a 10 Hz, because this search step value yields the same frequency resolution than the proposed procedure to obtain the Doppler frequency for the pre-correlation detector. Accordingly, the comparison is fair regarding a frequency resolution consideration. The experiment is performed and the mean execution time for the non-coherent detector is found to be 80.165 s.

5.9 Pre-correlation differential detector (non-modulated signal)

5.9.1 Figure of merit results

In Table. 5.2, the mean and the standard deviation of the figures of merit which result of the signal processing, using pre-correlation differential detectors are presented. For the experiment, a 10 ms integration time is used. In table 5.1, the normalized deflection coefficient for type 1 detector is presented to highlight the great degree of correlation between the designed figure of merit and the deflection coefficient in measuring performance in different Doppler scenarios. Bear in mind that the deflection coefficient succeeds in comparing performance for a specific detector under different scenarios. Therefore, the fact the designed figure of merit agrees with the deflection coefficient implies that the designed figure of merit succeeds in measuring performance for a specific detector under different scenarios. In order to estimate the execution time, the acquisition algorithms are executed 1000 times for each of the 600 signals and the mean execution time measured using timing routines is used as an estimate. The same signals as the ones used to

measure the execution time of the baseline non-coherent detector, are processed using the pre-correlation differential detector. The correlations for the pre-correlation differential detector have been implemented using the FFT method. Therefore, the procedure used to measure the execution time was exactly the same for the two algorithms. The mean acquisition execution time is 0.092 s instead of the 80.165 s needed using the baseline method (non-coherent detector).

Table 5.1: Figure of merit mean and standard deviation for Doppler frequency groups for the non-coherent detector

Doppler	0 kHz	-18 kHz	-30 kHz
Mean figure of merit	8.15	8.12	8.18
Standard deviation	0.58	0.91	0.62

In Table. 5.2, the mean and the standard deviation of the figures of merit resulting of the signal processing, using pre-correlation differential detectors are presented. For the experiment, a 10 ms non-coherent integration time is used. In Table. 5.3, the normalized deflection coefficient for type 1 detector is presented to highlight the great degree of correlation between the designed figure of merit and the deflection coefficient in measuring performance in different Doppler scenarios.

Table 5.2: Figures of merit mean and standard deviation for different Doppler frequency groups and different pre-correlation differential detectors.

Doppler/Type	0 Hz	-18 kHz	-30 kHz
Type 1 Mean	5.75	5.60	5.78
Type 1 S.D	0.66	0.73	0.66
Type 2 Mean	3.83	3.94	4.00
Type 2 S.D	0.28	0.39	0.31
Type 3 Mean	2.48	2.49	2.52
Type 3 S.D	0.37	0.38	0.40
Type 4 Mean	2.22	2.23	2.24
Type 4 S.D	0.32	0.31	0.33

In order to estimate the execution time, the acquisition algorithms are executed 1000 times for each of the 600 signals and the mean execution time measured using timing routines is used as an estimate. The same signals as the ones used to measure the execution

Table 5.3: Deflection coefficient for type 1 detector

Deflection coefficient/Doppler	0 kHz	-18 kHz	-30 kHz
Type 1/Mean	2.46	2.38	2.40

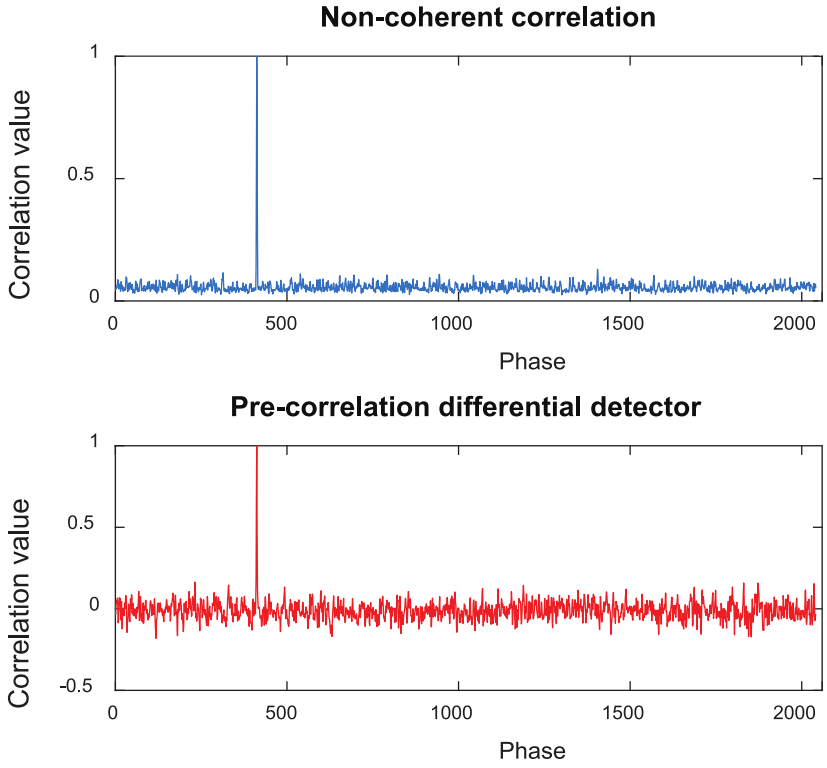

Figure 5.8: Correlation peak for different receiver architectures (10 ms integration time).

time of the baseline non-coherent detector, are processed using the pre-correlation differential detector. The correlations for the pre-correlation differential detector have been implemented using the FFT method. Therefore, the procedure used to measure the execution time was exactly the same for the two algorithms. The mean acquisition execution time is 0.092 s instead of the 80.165 s needed using the baseline method.

In Fig 5.8, the correlation results obtained by processing the same signal with different detectors are presented. It is shown that the acquisition peak appears for the same code phase offset.

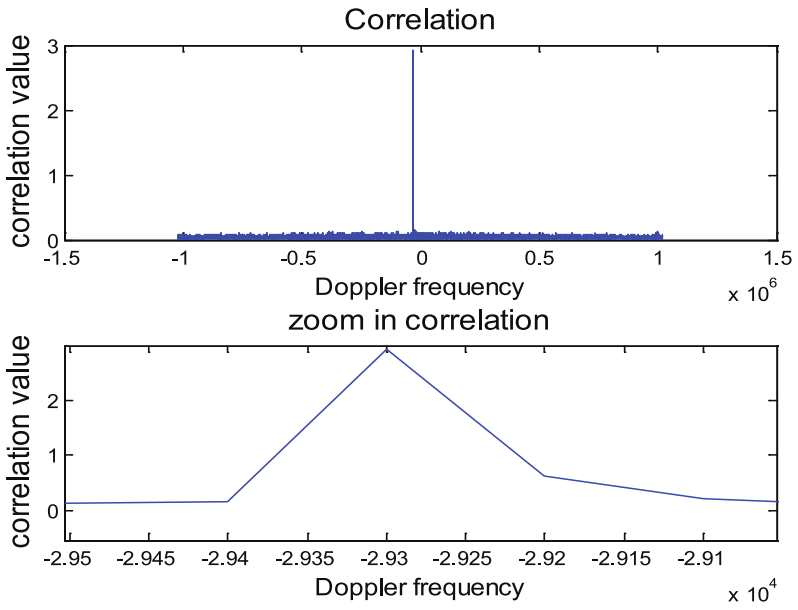

Figure 5.9: Doppler frequency estimation using the phase estimate (10 ms integration time).

5.9.2 Doppler frequency estimation

The concepts presented in [100] can be used to obtain an estimate for the GPS signal Doppler frequency. First, the input GPS signal is multiplied by a shifted version of the C/A code (the number of shifted samples must correspond to the phase offset obtained using the pre-correlation differential detector).

Once the input signal is multiplied by the shifted C/A code, the GPS signal is de-spreaded. If the FFT of the de-spreaded signal is calculated and plotted, a peak corresponding to the Doppler frequency appears. The process is applied to a 10 ms signal, hence the frequency resolution of the FFT is 100 Hz, [106]. In Fig. 5.9, the top graph, shows the entire frequency spectrum and the in the bottom graph, a zoom-in operation near the peak area. The zoom-in is applied to determine the Doppler frequency value.

The Doppler frequency is found to be -29.4 kHz, instead of -29.3 kHz, which is the actual Doppler frequency. The estimation error is equal to the FFT frequency resolution; therefore, the Doppler frequency estimation is successful.

5.9.3 Input Doppler Frequency effect Analysis

The statistical analysis intends to find out if statistically significant differences between the figures of merit of the signals that form each Doppler frequency group can be detected. In fact, this is the same statistical analysis procedure as the one used for the non-coherent detector. For each frequency group, the figures of merit of each signal are processed to obtain the probability density function. This analysis is useful to determine if significant differences in the characteristic probability density plots exist. Moreover, if differences are detected, the procedure helps in determining between which frequency groups these differences appear. As stated, each of the three groups is composed by a set of 600 signals which are not modulated by navigation data and are sharing the same Doppler frequency. The first case study deals with the study of the effect of the Doppler frequency on the classical pre-correlation differential detector. The objective is to demonstrate that the receiver works well despite the signal's Doppler frequency

In Fig. 5.10 the frequency distributions for type 1 and type 2 detectors are shown. When analyzing the frequency distributions, it is important to point out that the characteristic group probability density functions overlap in the vast majority of points. This fact sustains the idea the performance is similar for the three frequency groups. Therefore, in a practical, real world application, it can be concluded that the pre-correlation differential detector is coping well with high input Doppler frequency GPS signals. The results demonstrate that the receiver performance is virtually invariant to the input frequency. Hence, this detector can be used in high dynamic applications as the performance is not affected by the frequency, and the execution time speed-up is large. It is true, however, that for type 2, the 0 kHz group performs slightly worse. The major drawback of the method is that the figure of merit is approximately 6, whereas for the non-coherent detector the figure of merit is near to 8.

This means that for this case a bigger difference between the H_0 hypothesis maximum value and the H_1 hypothesis maximum value is obtained if the baseline non-coherent receiver is used. Therefore, the baseline detector performs better, but the difference in performance is not very large. The probability density distribution comparison for type 3 and type 4 detectors, shown in Fig. 5.11 reveals that, in fact, the probability distributions for the 3 groups with different mean Doppler frequency are similar. Therefore, the detector is working well despite the signal's input Doppler frequency. Using an experimental setup, it has been demonstrated that all the pre-correlation differential forms presented are close to being immune to the Doppler effect.

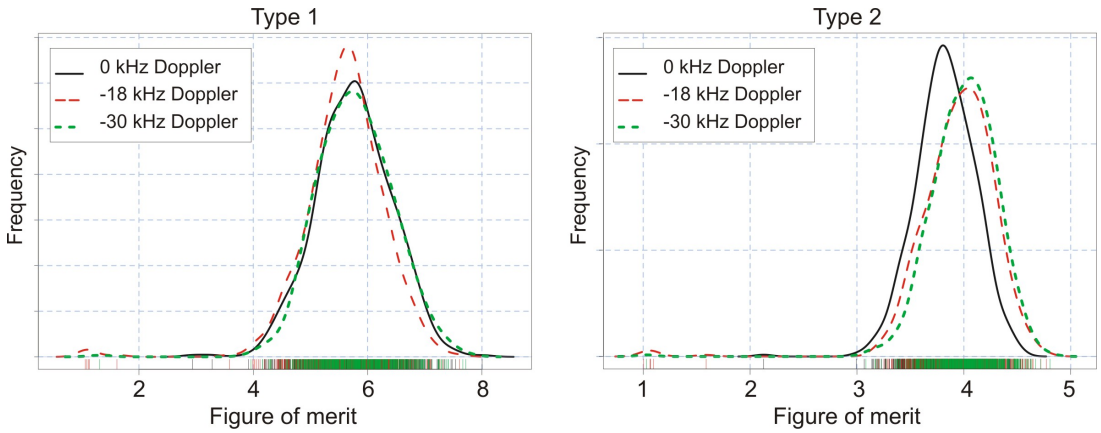

Figure 5.10: Probability density plots for the figures of merit of type 1 and 2 detectors (10 ms integration time).

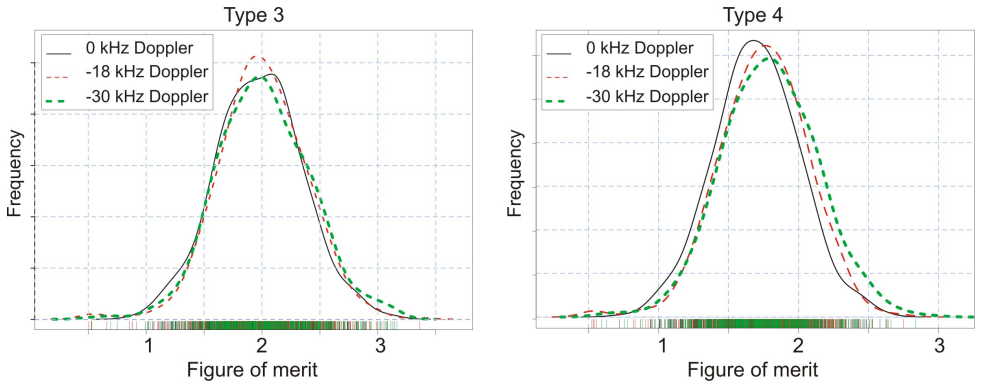

Figure 5.11: Probability density plots for the figures of merit of type 3 and 4 detectors (10 ms integration time).

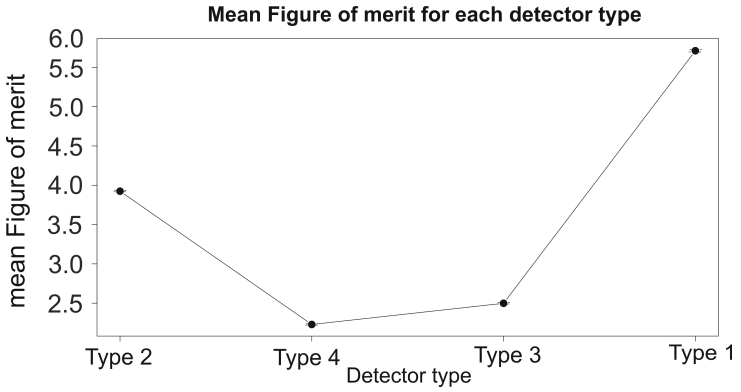

Figure 5.12: Detector figure of merit means (10 ms integration time).

5.9.4 Data modulation effect analysis

Once the receiver's Doppler behaviour has been characterized, the next step is to obtain a receiver/detector architecture comparison i.e. comparing detector performance for different detector architectures. To do so, the figures of merit of 600 signals belonging to the same Doppler frequency group are calculated and a statistical study to compare receiver performance is carried out. According to Fig. 5.12, detector types 1 and 2 (detectors that do not build the decision statistic using differential products) perform much better than detector types 3 and 4, which build the decision statistic using a differential product. The receiver/detectors that generate the decision statistic using the real part of the correlation result (type 1 and 3 detectors) perform better than receivers in which the decision statistic is formed using the modulus of the correlation result, no matter the input signal Doppler frequency. An explanation for this behaviour can be found in section 3.4.4.3.

5.9.5 Receiver architecture comparison

To analyze the data modulation effect on receiver performance, comparisons using signals with the same Doppler frequency are performed. Two sets of 600 signals are compared in Fig. 5.13. The two sets are characterized by a mean input Doppler frequency of 0 kHz (group 1 is compared with group 1a) and one set contains data modulated signals, whereas the other contains non-modulated signals. The figure of merit for the signals is calculated and the results are arranged into two probability frequency distribution graphs. The graph shows that the two signal sets behave similarly. The same study is performed to compare group 3 with group 3a) and, again, the two signal sets behave similarly. The frequency distributions shown in the two graphs agree with the theory, as they point out that the data modulation has virtually no effect on the receiver performance.

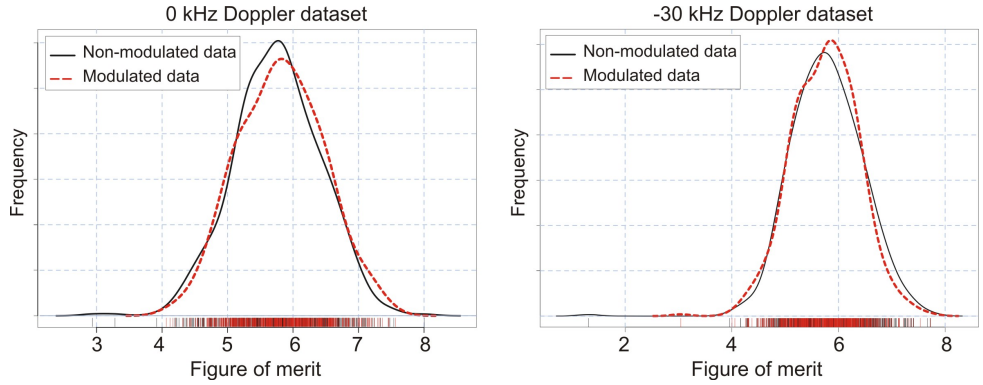

Figure 5.13: Probability distribution comparisons for modulated and non-modulated data (10 ms integration time).

5.10 Discussion

The evidence presented backs up the idea that the receiver/detector is working as expected, because despite the slight performance differences observed between Doppler frequency groups, these differences have no correlation with the group mean Doppler frequency value. Therefore, the observed differences are caused by the non-ideal behaviour of elements in the experimental setup and signal residual effects. The statistical frequency distribution analysis, shows that the Doppler frequency group behaviour is similar and that in a realistic simulation no behaviour differences caused by the Doppler frequency are appreciated. This argument is sustained by the fact that the values for the figure of merit of the 0 kHz Doppler frequency group have not been greater than for the other group values, so the detector is not performing better for low Doppler frequencies. The demonstrated invulnerability to high input Doppler frequency values, which is presented in the theoretical analysis and validated experimentally, suggests that the receiver is suitable for the LEO case study. An aspect to be highlighted, is the fact that if the probability density functions for detector architectures (as the one shown in Fig. 5.7) are analyzed, the residual phase offset effect makes the figure of merit change substantially and in random fashion. This is explained by the small sampling frequency used to reduce the computational cost. As stated in the theoretical discussion, this effect affects both the baseline non-coherent detector and the pre-correlation differential detector to the same extent. The performance comparison between the baseline non-coherent and the different pre-correlation differential detectors points out, that the non-coherent detector performs better. The figure of merit comparison for groups containing navigation data and groups that do not, shows that the receiver is not affected by the presence of the data signal, i.e.

it is immune to the presence of this signal. This fact is stated in the theoretical analysis, and confirmed by the results presented in Fig. 5.13) Statistical distributions for each receiver/detector are obtained. For detectors that generate the decision statistic using the real part of the correlation result (Type 1 and 3 detectors), the decision statistic is found to be distributed approximately following a Gaussian distribution both for the H_0 and H_1 hypotheses. On the other hand, detectors that generate the decision statistic using the modulus of the correlation (Type 2 and 4 detectors), result in Rayleigh distributions for the H_0 hypothesis and Rice distributions for the H_1 hypothesis. In [72], the H_0 hypothesis for type 3 receiver is said to follow a Laplace distribution for low signal power levels, but are said to follow a Gaussian distribution when considering a high signal level case-study so the obtained results match the results presented in [72]. In [9], it is suggested that for scenarios where the input Doppler frequency is high, it might be interesting to generate the decision statistic using the modulus of the correlation result, however the evidence presented here proves that, for the case study, the modulus decision statistic does not improve performance. Nevertheless, it must be stated that in [9], the suggestion is made considering a signal model with no additive noise. An explanation for the fact the detector forming the decision statistic does not improve performance, can be found if the probability density functions are considered. In Rayleigh distributions, more samples tend to concentrate on the right distribution tail, hence if the maximum value for the H_1 hypothesis does not change, the difference between the H_0 and H_1 hypotheses maximum values decreases. This fact partly explains the decrease in the performance of the decision statistics generated using the modulus. When dealing with type 3 and 4 detectors, the decision statistic is generated using the differential product. From the experiments performed, it is confirmed that the correlation peak decreases, so the figure of merit does not improve. So, in fact, in a high dynamic context, the two differential inputs are not as correlated accounting for the fast frequency variations caused by the dynamic stress. This behaviour was predicted and described when studying the differentially coherent detector in section 3.4.4.3. Therefore it is confirmed that the doubly differential architecture does not work well in this scenario. Beyond detection, the other key aspect is the execution time. The pre-correlation differential detector improves the acquisition time by a factor of 1000, at the expense of a slightly decreased signal quality. Recalling the above-mentioned aspects, it can be stated that pre-correlation differential implementation using the real part decision statistic is feasible for a high dynamic scenario, especially baring in mind the 1000 times speed-up. In addition, the decrease in the detector performance (when comparing with the non-coherent detector) is not so important when considering that for a LEO satellite the signal level is high and that each time GNSS systems are updated, the transmitted power increases substantially. The Doppler frequency estimation procedure works perfectly and it is proved that the estimation procedure is not computationally

burdensome. This result agrees with the theoretical computational cost study performed. Therefore, the procedure can be employed, and the pre-correlation differential detector can be used along with a standard tracking loop.

5.11 Conclusions

A SDR experimental setup is used to implement a technological demonstrator for detector/receiver architectures in a realistic LEO scenario. The pre-correlation differential detector for the LEO context has been studied theoretically to evaluate its suitability for the case study. Moreover, the receiver's suitability for the case study (especially taking into consideration that GNSS evolutions tend to include new signals with increased transmitted power) has been validated experimentally using a Spirent GSS7700 signal generator to generate a realistic scenario. The detector has been able to acquire signals without performing a frequency search. An ad hoc figure of merit has been designed and used to evaluate the detector performance. The figure of merit has been used to show that the pre-correlation differential detector can be used in this high signal level scenario. The residual effects affecting the pre-correlation differential detector performance, such as the data modulation and the residual phase offset effect, have been studied. Using the standard pre-correlation differential detector presented as the starting point, different modified architectures have been implemented and evaluated in a LEO scenario. The architecture that generates the decision statistic using the real part (type 1 detector) of the correlation result performs the best. Each detector type has been characterized by means of statistical distributions, which help in describing the detector performance. The figure of merit decreased performance in the pre-correlation differential detector in comparison to the non-coherent detector has been quantified. This information is useful in future applications, as it can be used as a reference. The speed-up has been quantified by comparing the execution time of the non-coherent detector and the detectors under test. The large speed-up obtained suggests that for the case of a LEO satellite in which constraints linked to the receiver movement, imply a fast acquisition is needed, the proposed detector is a suitable choice. Furthermore, LEO satellites, generally have limited power capabilities, and a method as the one proposed in this work can help in energy management issues. A method to estimate the Doppler frequency is successfully used, and it is demonstrated that this method does not increase the computational cost substantially.

Chapter 6

DBZP for LEO embedded receivers

6.1 Introduction

In this chapter, a specific receiver acquisition solution for LEO embedded GPS receivers is studied. As pointed out in section 3.2.1, the receiver specifications for a LEO embedded GNSS receiver are different from the requirements for a ground application receiver, primarily because of the fast LEO satellite movement and because of the different environmental conditions. Therefore, it is appealing to perform a study to evaluate pros and cons of the usage of the DBZP algorithm in the LEO scenario as this algorithm is known to alleviate the computational cost as stated in [1]. The final aim of the work included in this chapter is to prove that the DBZP is suitable for this LEO scenario. More specifically, the algorithm sensitivity and execution time will be analyzed theoretically and experimentally.

6.2 DBZP working principle

The DBZP algorithm relies on an effective implementation of the standard FFT correlation concept for GNSS acquisition. The idea behind the usage of the DBZP is to take advantage of the fact partial correlations are computationally more efficient than a full correlation. Moreover, the DBZP does not perform the costly Doppler frequency search space as the Doppler search is implemented via a Fast Fourier Transform shift using the FFT shift properties. Therefore, it is appealing to use this algorithm for a LEO satellite receiver attending to computational cost reduction considerations.

Basically, the DBZP implements the PFS [70] algorithm on signal blocks smaller than a coherent integration period. In this way partial correlations which are less computationally burdensome are used (as stated in section 3.5.1, 10 N points FFT operations are computationally less burdensome than a single 10N points FFT operation). However, the major drawback is that for the DBZP the correlation depends on two Doppler attenuation terms. The first attenuation term appears when implementing the partial correlation with a circular shifted C/A code. This process is equivalent to the standard serial search and results in a equivalent attenuation term. The second attenuation term appears when using the FFT (using the FFT shift property) to search for the input Doppler frequency.

Some definitions that will help in the performance analysis of the DBZP will be detailed in the following lines.

The time duration of one block is:

$$t_{bd} = \frac{T_c}{N_b} \text{ s.} \tag{6.1}$$

Therefore, the number of samples per block is:

$$spb = \frac{N_s}{N_b} = \frac{T_c}{N_b} f_s = t_{bd} f_s \text{ samples} \tag{6.2}$$

Where:

f_s is the sampling frequency. T_c is the coherent integration time.

The DBZP algorithm can be divided in the following steps:

1. An input signal composed of N_s samples is divided into N_b blocks of $\frac{N_s}{N_b}$ samples (*spb* samples per block).
2. The signal blocks are arranged to form signal slices of two consecutive blocks.
3. The same splitting process is performed for the local spreading code. A C/A code of N_s samples is generated and splitted into N_b blocks of spb samples.
4. The N_b blocks of the local code are zero-padded with $\frac{N_s}{N_b}$ samples. In this way both the code and signal blocks have the same size. The code blocks must be zero-padded to preserve the correlation isolation provided by C/A codes [1]. Note that when performing a partial correlation, the isolation characteristics are not preserved.

Remember that the longer the correlation code is, the larger the correlation isolation is.

5. The blocks of the input signal and the blocks of the code are correlated using the FFT based correlation principle and only the first part of the correlation vector result is stored i.e. the first *spb* samples In this way, the partial correlations are calculated.

6. For every iteration, code blocks are circularly permuted to perform the Doppler frequency search and the steps from 4 to 7 must be repeated to form a matrix of size $N_b N_s$. The circular permutation of the code blocks implies that a Doppler frequency search is performed. Note that $Corr_{11}$ is the correlation of the first signal slice and the first code slice. $Corr_{22}$ is the result of the correlation of the second signal slice and the second code slice.

7. The FFT of the columns of the matrix is calculated.

The size of N_b is:

$$N_b = \Delta f_d T_c \tag{6.3}$$

Where Δf_d: Doppler frequency search span.

Steps 1-6 are illustrated in Fig 6.1.

Note that the number of bins is fixed. The receiver coherent integration time can be increased in order to increase the frequency search bins and the sensitivity to input Doppler can be handled in this way. Nevertheless, if the coherent integration time is increased so does the computational cost. The data modulation effect may lead to a complete attenuation of the signal. Moreover, the sensitivity to frequency Doppler is one of the most important shortcomings of the DBZP method. Nevertheless, it is still appealing to study this algorithm in high dynamics scenario to find out if by carefully selecting the acquisition parameters the method can yield some computational cost decrease.

Three very important aspects to point out prior to performing tests are the following:

- The DBZP does not perform the costly frequency search, therefore it is interesting to use the DBZP in wide Doppler search spaces (as LEO embedded satellites).

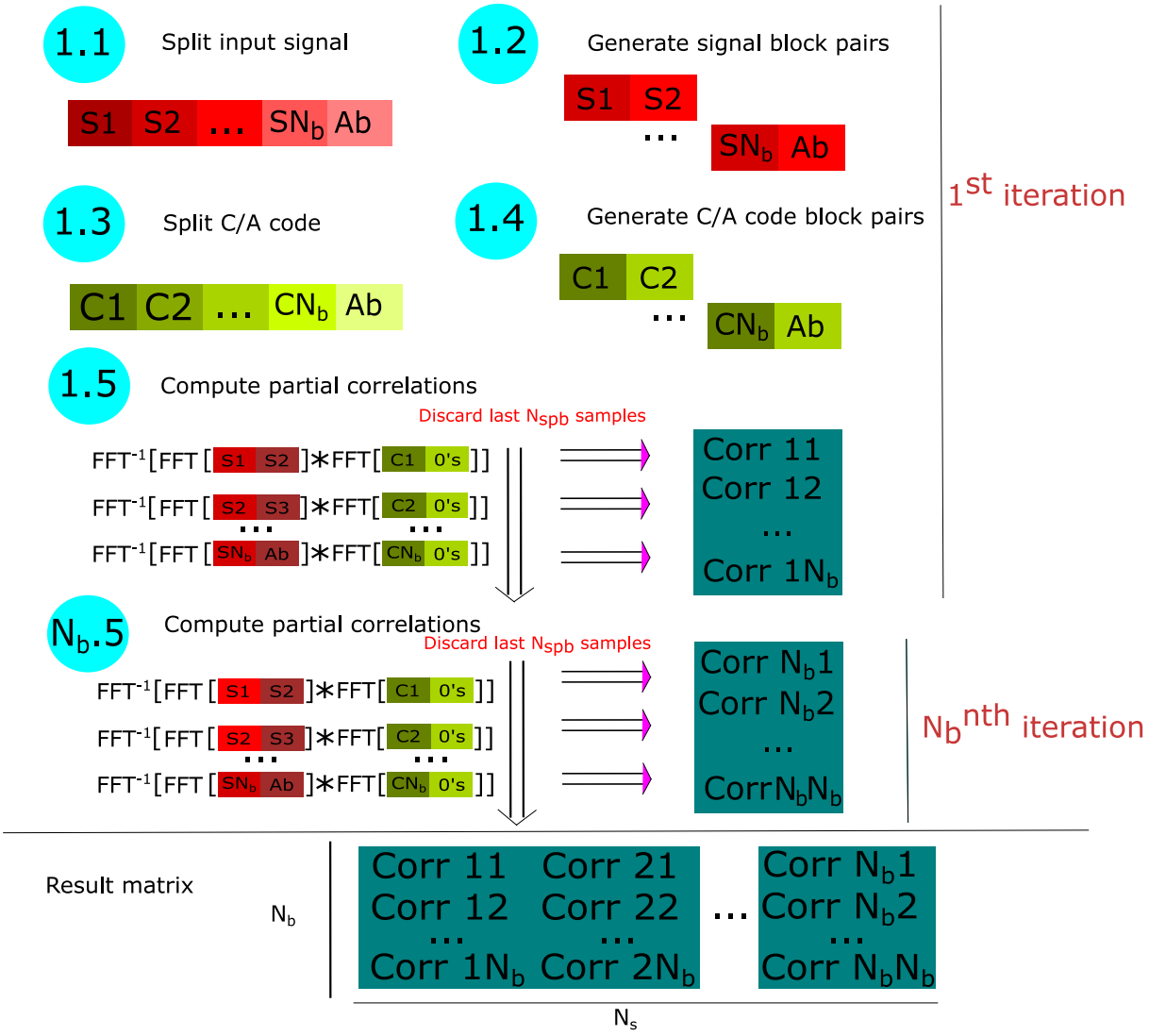

Figure 6.1: DBZP acquisition process.

- DBZP uses partial correlations which lead to reduced size FFTs, which are more computationally efficient.
- The probability distributions of the non-coherent detector and the DBZP are exactly the same. This feature makes it easier to compare performance.

The performance of the DBZP can be seriously hindered by the Doppler frequency attenuation. More specifically, the equations describing the attenuation to which the GPS is subject to because of the DBZP are Eq. 6.6 and Eq. 6.7. A thorough study of this effect on the DBZP performance is provided in section 6.3.1.

6.3 DBZP theoretical performance in a LEO scenario

6.3.1 Doppler attenuation

The theoretical performance of the DBZP depends on the so-called Doppler signal impairments. Specifically, a term describing the attenuation caused by code Doppler and a term describing the frequency Doppler are provided. For details on how these terms are derived, the reader is invited to check [1].
As highlighted in [1], the DBZP attenuation dependency with the input Doppler frequency depends on two different terms. The first term depends on the Doppler frequency magnitude and the second term has periodic dependence on the Doppler frequency. The total attenuation caused by the DBZP is described in Eq. 6.4, in which Doppler and code Doppler attenuations are considered.

$$Att_{dbzptotal} = Att_{codedoppler} Att_{Doppler}. \tag{6.4}$$

Where:

$$Att_{Doppler} = Att1dbzp \times Att2dbzp, \tag{6.5}$$

and

$$Att1dbzp = \mathrm{sinc}^2(\pi f_d t_{bd}). \tag{6.6}$$

In Fig. 6.2, the attenuation corresponding to Eq. 6.6 is represented for the LEO search space $fd = -50$ kHz to 50 kHz , $T_c = 1$ ms and $N_b = [100, 200, 500 \text{ and } 1000]$.

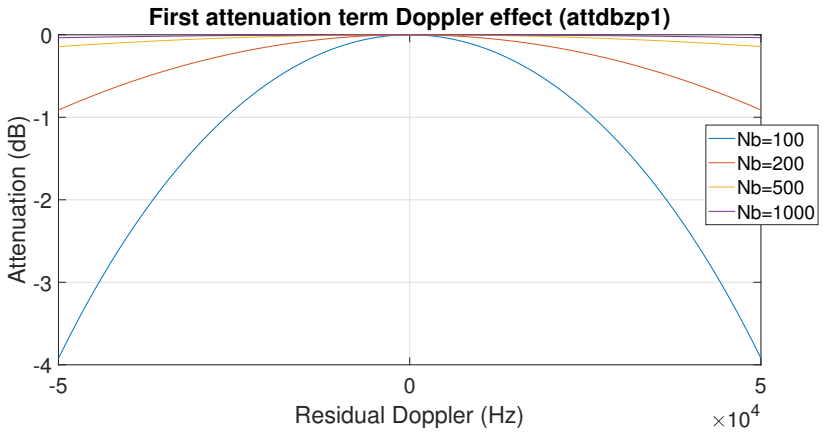

Figure 6.2: DBZP attenuation first term.

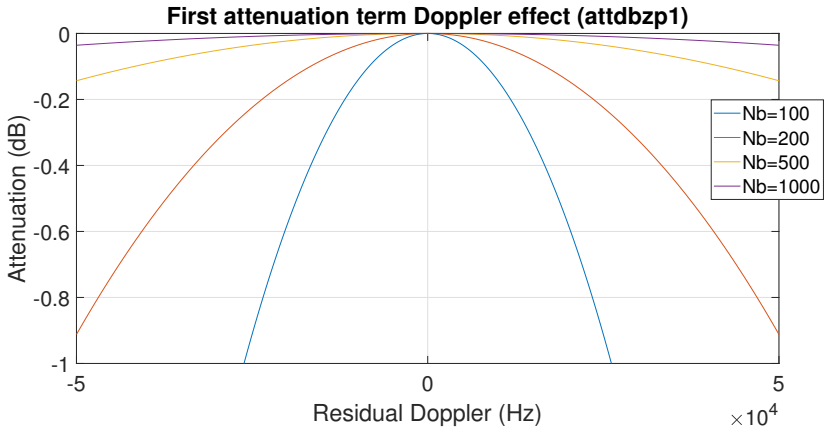

Figure 6.3: DBZP attenuation zoom first term.

The detail of the top part of Fig. 6.2 is shown in Fig. 6.3. It is very important to take note of the fact the sensitivity to Doppler frequency increases as N_b decreases. Hence increasing N_b increases the DBZP immunity to Doppler frequency. Eq 6.6 describes the attenuation caused by the Doppler frequency error (equivalent to the usual frequency drift error for the coherent detector). Bear in mind the DBZP implements the Doppler frequency search by performing a circular shift on the local code replica. And when the time duration of the code blocks decreases, the frequency resolution of the FFT increases, hence the Doppler frequency estimation error decreases.

$$Att2dbzp = \frac{\text{sinc}^2(\pi\,(r - f_d T_c))}{\text{sinc}^2\left(\frac{\pi(r - f_d T_c)}{N_b}\right)}. \tag{6.7}$$

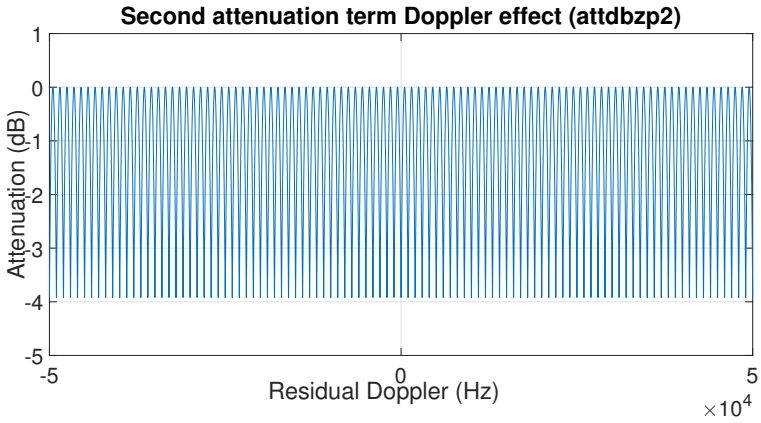

Figure 6.4: DBZP attenuation second term.

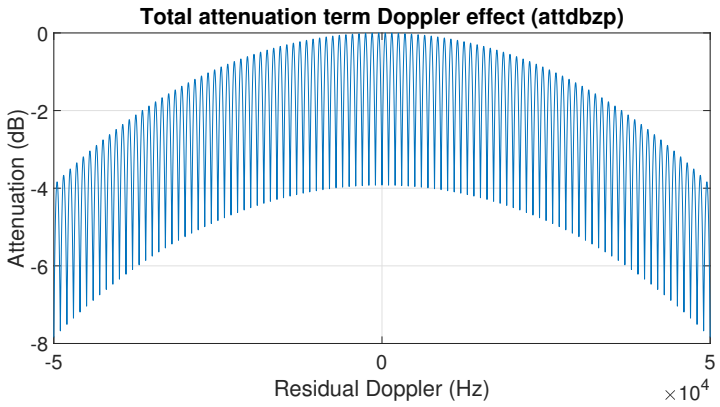

Figure 6.5: DBZP acquisition attenuation.

Where $r = 0, 1, ...N_b - 1$.

In Fig. 6.4, the attenuation corresponding to Eq. 6.7 (second attenuation term) is represented for the LEO search space $fd = -50$ kHz to 50 kHz, $T_c = 1$ ms and $N_b = 100$. The attenuation shows a periodic behaviour with a maximum attenuation of circa 4 dB.Accordingly, the combined effect of the two attenuation terms for an integration time of 1 ms T_c=1 ms and N_b=100 as shown in Eq. 6.4. In Fig. **??**, the attenuation for the LEO search space, for a GPS L1 C/A signal with an integration time of 1 ms is shown. The graph shows that the attenuation takes values close to 8 dB for an input Doppler of 50 kHz. Therefore, the DBZP incurs in a very important signal loss. Even in scenarios where the 8 dB signal loss is not a problem (sensitivity wise), an 8 dB attenuation linked to the receiver dynamics can be a problem as an 8 dB dynamic range can be difficult to manage.

Bear in mind that for a LEO satellite scenario, the attenuation is not larger than for

a static scenario because the number of frequency search bins is larger (in order to explore the full Doppler search space) and if the number of search bins increases the attenuation factor decreases. However, from the above analysis it follows that in order to be usable the attenuation of the DBZP must be reduced. In section 6.5.1, a configuration that deals with the problem is discussed.

6.3.2 Code Doppler

In the LEO scenario, the code Doppler can cause serious attenuation and is an effect which has to be accounted for. For the L1 C/A signal, the code Doppler attenuation depends on the code drift in chips as expressed in Eq. 6.8 and Eq. 6.9.

$$\Delta\zeta = T_c f_{chip} \frac{f_d}{f_{L1}}. \tag{6.8}$$

$$R_c^2 = \left(1 - |\Delta\zeta|\right)^2. \tag{6.9}$$

The code Doppler attenuation for a Doppler frequency of 50 kHz and different coherent integration times is shown in Table 6.1.

Table 6.1: DBZP code Doppler attenuation

T_c (ms)	Attenuation (dB)
1	0.282
2	0.574
5	1.514
10	3.350
20	8.874

When taking into consideration coherent integration times larger than 1 ms, the attenuation is not negligible and when considering integration times above 5 ms the attenuation can be considered to be severe. In the following analysis a value of T_c= 1 ms will be considered in order to make the code Doppler attenuation as close to negligible as possible.

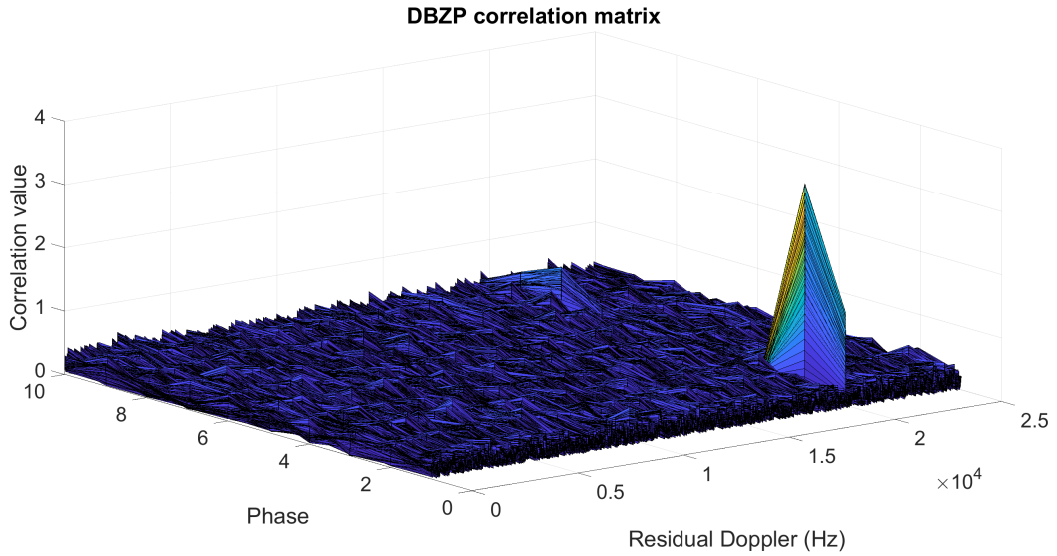

Figure 6.6: DBZP acquisition.

6.4 Software implementation for the Modified DBZP

Using a SDR methodology the DBZP acquisition algorithm has been implemented. We simulate the LEO scenario GNSS signal using a Spirent GSS7700 and we use an USRPx310 as a front-end as described in configuration 1 in section 4.3. The DBZP is implemented and an example of a successful acquisition is shown in Fig. 6.6. It is interesting to point out that the peak is triangular in the Doppler domain because the frequency search bin is not quite wide ($T_c = 1$ ms, N_b and $T_c = 10$ ms). The Doppler frequency and code phase obtained with the algorithm are compared to the results obtained using the baseline non-coherent detector. The estimated parameters using the DBZP and the non-coherent detector are found to be the same, hence the DBZP is correctly implemented. Moreover, the histograms of the decision statistics of a standard non-coherent detector and the histogram of DBZP are compared in Fig. 6.7. As in theory [1], the histograms follow the same distribution. Hence taking into consideration that the histograms and the correlation matrices of the DBZP and the non-coherent detector yield identical results, the SDR implementation is correct.

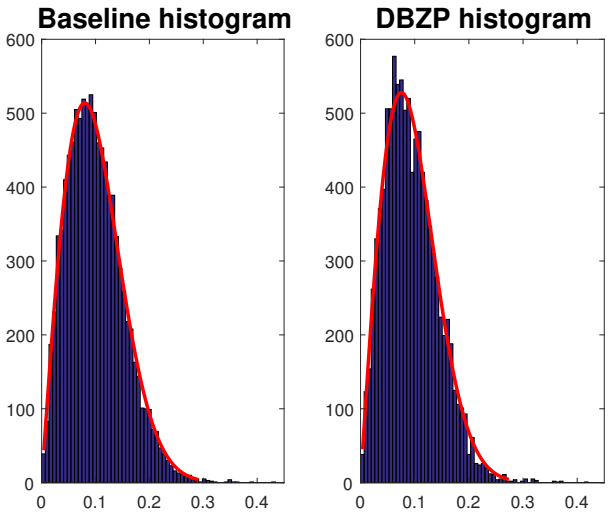

Figure 6.7: Histogram comparison.

6.5 Modified DBZP performance for a LEO scenario

6.5.1 LEO scenario attenuation mitigation

The DBZP working principle is explored in order to find out a solution to overcome the constraints. The method is optimized to make its usage in a LEO scenario possible. By zero padding and by increasing the number of blocks it is possible to limit the attenuation, however the bigger the number of blocks and the zero padding, the bigger the computational cost is. Therefore, the parameters must be carefully examined and a compromise between improving execution speed and limiting attenuation is compulsory.

In order to mitigate the attenuation two design rules can be adopted. More specifically, it is possible to modify the number of blocks. By artificially doubling the number of blocks the maximum attenuation caused by the input Doppler frequency is reduced from 4 dB to 0.9 dB. To mitigate the effect of the periodic attenuation term, it is necessary to zero-pad the columns of the matrix before applying the final FFT. The new correlation matrix has a size of $2N_b \times 4N_s$ In this way, the attenuation caused by the periodic term is reduced from 4 dB to 0.2 dB. The impact of both modifications is shown in Fig. 6.8 if the initial parameters are $N_b = 100$ and $N_s = 10000$

The maximum attenuation is now 1.12 dB, hence Fig.6.8 demonstrates that the usage of the DBZP is now feasible. The graph has been plotted showing an attenuation range spanning from -8 dB to 0 dB in order to give an idea of the attenuation decrease (bear in mind that the standard DBZP produces an 8 dB maximum attenuation, see

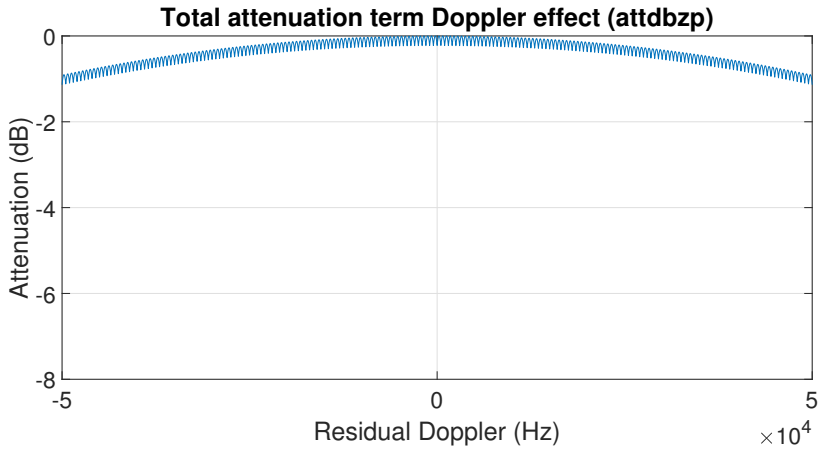

Figure 6.8: Modified DBZP attenuation.

Fig. 6.5) by showing the attenuation of the modified DBZP in the attenuation range of the non-modified DBZP. This theoretical discussion shows that by modifying N_b and N_s, it is possible to solve the attenuation problem. However, depending on the receiver specifications it might be interesting to accept a higher worse case attenuation to improve execution time.

6.5.2 Sensitivity empircal tests

Using a SDR philosophy (Configuration 1 in section 4.3.1), it is proved that by modifying the DBZP it is possible to use the DBZP in a LEO scenario. To prove the feasibility of implementing the DBZP in the LEO scenario, a test is performed to compare the sensitivity loss of the DBZP and the modified DBZP with respect to the baseline non-coherent algorithm for the worst-case Doppler frequency. Signals with different carrier to noise ratio are generated and three different algorithms are used to acquire signal for the various signal power levels. Starting with a signal with a high power level, the signal power is reduced until the signal level reaches a point in which the algorithm is unable to acquire the signal as the detection threshold is not surpassed, the acquisition threshold is obtained. In Table 6.2, the sensitivity loss of the DBZP and the modified DBZP with respect to the baseline non-coherent algorithm are shown.

Table 6.2: Sensitivity loss comparison

Algorithm	Sensitivity loss
DBZP	7.9
DBZP (modified)	0.5

The modified DBZP incurs in just a 0.5 dB loss when comparing with the baseline

non-coherent detector. Therefore, the modified DBZP performs similarly sensitivity-wise. Now the final question to answer is if the execution time of the modified DBZP is faster than the execution time of the non-coherent detector.

6.5.3 Execution time comparison

Once the sensitivity analysis is performed, the next stage is to investigate if the execution speed of the modified DBZP is smaller than the execution time for the baseline non-coherent detector. The execution speed for the two algorithms are measured 1000 times for the same signal. The results are shown in Table 6.3.

Table 6.3: Execution time comparison between baseline and modified DBZP

Search space/Algorithm	Baseline	Modified DBZP
-10 kHz to 10 kHz	0.1026 s	0.0705 s
-50 kHz to 50 kHz	0.8865	06146 s

The modified DBZP yields some execution time improvement when comparing with the baseline non-coherent detector. Hence the usage of the modified DBZP is advisable for the LEO scenario.

6.6 DBZP conclusions

After zero padding and increasing the number of blocks, the DBZP execution time is still faster than the execution time for the baseline non-coherent detector, so the proposed configuration is suitable for the application. The DBZP working principle is explored in order to find out a solution to overcome the constraints. The method is optimized to make its usage in a LEO scenario possible. By zero padding and by increasing the number of blocks it is possible to limit the Doppler attenuation, however the bigger the number of blocks and the zero padding, the bigger the computational cost is. Therefore, the parameters must be carefully examined and a compromise between improving execution speed and limiting attenuation is compulsory.

Chapter 7

Conclusions

The theoretical analysis and the empirical performance tests included, sustain the idea that both the pre-correlation detector and the DBZP are well-suited to deal with the LEO scenario problem. Nevertheless, both the pre-correlation detector and the DBZP suffer from sensitivity loss when compared with the baseline acquisition procedures. However, it has been demonstrated that the sensitivity loss is not large enough to prevent a successful acquisition for high signal power scenarios. Moreover, the trend for modernized signals is to increase the transmitted power level. Therefore, these detectors will be better suited to the LEO scenario problem as the GNSS satellites transmitted power increases. Accordingly, the reported improvement in execution time speed and the correct signal sensitivity performance imply a significant performance improvement.

In the following paragraphs, the main results and the concluding remarks which can be extracted from these results are presented.

7.0.1 Summary of results

The main points which have been discussed in this work can be summarized in the following list:

1. A technological demonstrator for high dynamics scenarios has been assembled from scratch. Procedures to validate the correct operation of a GNSS technological demonstrator have been provided and discussed. Furthermore, a figure of merit to measure performance for the specific LEO scenario is introduced, described and tested. This figure of merit is shown to perform well in the tests performed. Hence,

an appropriate SDR environment and theoretical tools to study the LEO scenario have been provided.

2. The behaviour of some detector architectures (coherent, non-coherent, differentially coherent and pre-correlation) for the GNSS LEO scenario has been discussed and analyzed. Mathematical descriptions for the signal impairments (focusing on the LEO scenario) have been provided. Using this analysis, the pros and cons linked to the usage of different GNSS signals for the LEO scenario are provided. In this way, a reasoned signal selection that takes into consideration the characteristics of the LEO scenario (within the acquisition problem), can be performed.

3. A complete and detailed theoretical study of the pre-correlation detector and its performance for the LEO scenario, is included. Moreover, a detailed description of the practical implementation and a theoretical computational cost study are included. Furthermore, the theoretical computational cost and performance studies are validated via empirical tests. Therefore, a theoretical and a practical proof of the suitability of the pre-correlation detector for the LEO scenario is provided.

4. A feasible practical implementation for the DBZP method for the LEO scenario is presented. The performance of this method for the LEO scenario is measured by performing an execution time study. Using a similar procedure, the feasibility in terms of sensitivity performance is validated via empirical tests. Therefore, the two main aspects related to receiver performance have been covered.

From the summary of the work performed, the main conclusions can be listed as follows:

1. It is clear that the L1 C/A signal is a sensible choice to tackle the acquisition problem in the LEO scenario. It has been demonstrated that this signal is the best choice regarding computational cost considerations. Moreover, the L1 C/A code signal tolerates the receiver dynamics the best.

2. The experiments to validate the technological demonstrator performance, point out that the technological demonstrator succeeds in reproducing the Doppler effects, which are actually the main concern for the LEO GNSS case-study. Nevertheless, the experiments must be repeated a number of times in order to obtain meaningful information for receiver characterization.

3. The tests performed and the theoretical suitability studies show that the pre-correlation detector is able to deal with the acquisition of the L1 C/A signal in

the LEO scenario (the 47 dBHz signal level has been selected taking into consideration that GNSS evolutions tend to include new signals with increased transmitted power).

4. Moreover, tests demonstrating a huge speed-up linked to the usage of the pre-correlation detector have been conducted. In the case of a LEO satellite, the constraints linked to the receiver movement imply a fast acquisition is needed. The large speed-up reported, suggests that the pre-correlation detector is very well adapted for the LEO case study.

5. The feasibility study of the DBZP method for the the LEO scenario, points out that the DBZP method provides a moderate speed-up. Nevertheless, despite the fact the speed-up is moderate, it is enough to test this method in specific hardware within a LEO scenario. LEO satellites, generally, have limited power capabilities and the speed-up (despite being a moderate one) can be decisive.

7.0.2 Future research lines

The points developed in this work can help in tackling the LEO acquisition problem, as from the empirical tests performed an improvement in the execution speed is obtained. Moreover, the receiver performance is demonstrated to be sufficient for the LEO scenario, as the output SNR level is enough to acquire the signal. Nevertheless, the execution time speed improvement in the technological demonstrator may not translate into the same execution time improvement when implementing the algorithms in hardware such as a FPGA. Accordingly, a future research line is the FPGA implementation of the pre-correlation and the DBZP algorithms for a LEO scenario. Furthermore, some real dynamic testing in which the receiver suffers from real dynamic stress could be performed to quantify the effect of the dynamic stress on the receiver clock oscillator. Finally, a study in which the noise is modelled as colored noise instead of Gaussian noise could be performed to validate which noise hypothesis models the noise effect the best.

The insight provided in this work, can be used as the foundations to study more complex scenarios in which phenomena such as jamming, multipath and dynamics coexist. For instance, the automated rendez-vouz scenario is a scenario in which multipath and high-dynamics coexist. Furthermore, a future interesting case-study could be a case in which jamming and high-dynamics coexist.

Another point to be addressed in future studies, is to construct a full high-dynamics receiver by dealing with the high-dynamics tracking problem. This means that a special acquisition to tracking transition should be implemented. Moreover, a study to find out the pros and cons of the pre-correlation tracking method should be performed.

Finally, the technological demonstrator can be used to implement some other computational cost reduction methods such as compressed sensing methods for more upcoming modernized signals. The hybridization of acquisition based on computational cost reduction methods with sensor information using Kalman filters, is another potential area of future interest.

Figure list

Table list

Acronyms

ADC Analog to Digital Converter.

AGPS Assisted Global Positioning System.

AltBOC Alternative Binary Offset Carrier.

ASIC Application-Specific Integrated Circuit.

AWGN Additive White Gaussian Noise.

BOC Binary Offset Carrier.

BPSK Binary Phase Shift Keying.

CBOC Composite Binary Offset Carrier.

CDMA Code Division Multiplexing Access.

CN Carrier to Noise Ratio.

CoCom Coordinating Committee for Multilateral Export Controls.

CRC Cyclic Redundancy Check.

DAC Digital to Analog Converter.

DBZP Doble Block Zero Padding.

DME Distance Measuring Equipment.

EEPROM Erasable Electronic Read Only Memory.

EGNOS European Geostationary Navigation Overlay Service.

FDMA Frequency Division Multiplexing Access.

FEC Forward Error Correction.

FFT Fast Fourier Transform.

FPGA Field Programmable Gate Array.

GigE Gigabit Ethernet.

GLONASS GLObalnaya Navigasionnay Sputnikovaya Sistema.

GLRT Generalized Likelihood Ratio Test.

GNSS Global Navigation Satellite System.

GPS Global Positioning System.

GPU Graphics Processor Unit.

IC Integrated Circuit.

IF Intermediate Frequency.

INTA Instituto Nacional de Técnica Aeroespacial.

IRNSS Indian Regional Navigation Satellite System.

JTAG Joint Test Action Group.

LEO Low Earth Orbit.

LNA Low Noise Amplifier.

LRT Likelihood Ratio Test.

MCX Micro Coaxial Connector.

MEO Medium Earth Orbit.

MGDC Modified General Differential Combination.

MLE Maximum Likelihood Estimator.

NH Neuman-Hofman.

NMEA National Marine Electronics Association.

NP Neyman-Pearson.

OS Open Service.

PCIe Peripheral Component Interconnect Express.

PD Probability of Detection.

PDF Probability Density Function.

PFA Probability of False Alarm.

PFS Parallel Frequency Search.

PPB Part Per Billion.

ppm Part Per Million.

PPS Pulse Per Second.

PRN Pseudorandom noise.

PRS Public Regulated Service.

PSK Phase Shift Keying.

QPSK Quadrature Phase Shift Keying.

QZSS Quasi-Zenith Satellite System.

R820T Rafael 820 Tuner.

RAM Random Access Memory.

ROC Receiver Operation Curve.

SA Selective Availability.

SDR Software Defined Radio.

SNR Signal to Noise Ratio.

Tbit Data bit period.

Tint Integration time.

TMBOC Time Multiplexed Binary Offset Carrier.

TXCO Temperature Controlled Oscillator.

UHD USRP Hardware Driver.

UMP Uniform Most Powerful.

USB Universal Serial Bus.

USRP Universal Software Radio Peripheral.

Bibliography

[1] M. Foucras, "Performance analysis of modernized gnss signals acquisition," Ph.D. dissertation, Institut National Polytechnique de Toulouse, February 2015.

[2] S. H. Kong, "High sensitivity and fast acquisition signal processing techniques for gnss receivers: From fundamentals to state-of-the-art gnss acquisition technologies," *IEEE Signal Processing Magazine*, vol. 34, no. 5, pp. 59–71, Sept 2017.

[3] J. Arribas, C. Fernández-Prades, and P. Closas, "Antenna array based gnss signal acquisition for interference mitigation," *IEEE Transactions on Aerospace and Electronic Systems*, vol. 49, no. 1, pp. 223–243, Jan 2013.

[4] H. Al-Bitar, "Advanced gps signal processing techniques for lbs services," Ph.D. dissertation, Institut National Polytechnique de Toulouse, July 2007.

[5] J. B.-Y. Tsui, *Fundamentals of Global Positioning System Receivers: A Software Approach*. 605 Third Avenue, New York, NY 10158-0012: John Wiley & Sons, Inc., 2000.

[6] L. M. B. Winternitz, W. A. Bamford, and G. W. Heckler, "A gps receiver for high-altitude satellite navigation," *IEEE Journal of Selected Topics in Signal Processing*, vol. 3, no. 4, pp. 541–556, Aug 2009.

[7] ESA, *GNSS Market Report Issue 5*. Luxembourg: Publications Office of the European Union, September 2017.

[8] R. T. Ioannides, T. Pany, and G. Gibbons, "Known vulnerabilities of global navigation satellite systems, status, and potential mitigation techniques," *Proceedings of the IEEE*, vol. 104, no. 6, pp. 1174–1194, June 2016.

[9] C. O'Driscoll, "Performance analysis of the parallel acquisition of weak gps signals," Ph.D. dissertation, National University of Ireland, January 2015.

[10] S. K. Shanmugam, "New enhanced sensitivity detection techniques for gps l1c/a and modernized signal acquisition," Ph.D. dissertation, University of Calgary, January 2008.

[11] L. Musumeci, F. Dovis, P. F. Silva, H. D. Lopes, and J. S. Silva, "Design of a very high sensitivity acquisition system for a space gnss receiver," in *2014 IEEE/ION Position, Location and Navigation Symposium - PLANS 2014*, May 2014, pp. 556–568.

[12] W. Zhang and M. Ghogho, "Improved fast modified double-block zero-padding (fmdbzp) algorithm for weak gps signal acquisition," in *2010 18th European Signal Processing Conference*, Aug 2010, pp. 1617–1621.

[13] G. X. Gao and P. Enge, "How many gnss satellites are too many?" *IEEE Transactions on Aerospace and Electronic Systems*, vol. 48, no. 4, pp. 2865–2874, October 2012.

[14] D. Franc, B. Matej, B. Daniele, G. Ciro, B. Gianmarco, and B. Marco, "An experimental evaluation of low—cost gnss jamming sensors," *Navigation*, vol. 64, no. 1, pp. 93–109, 2017. [Online]. Available: https://onlinelibrary.wiley.com/doi/abs/10.1002/navi.184

[15] R. H. Mitch, R. C. Dougherty, M. L. Psiaki, S. P. Powell, O'Hanlon, B. Brady W., J. A., and T. E. Humphreys, "Signal characteristics of civil gps jammers," in *Proceedings of the 24th International Technical Meeting of The Satellite Division of the Institute of Navigation*, September 2011, pp. 1907–1919.

[16] M. Amin, Z. Liang, and A. R. Lindsey, "Subspace array processing for the suppression of fm jamming in gps receivers," *IEEE Transactions on Aerospace and Electronic Systems*, vol. 40, no. 1, pp. 80–92, Jan 2004.

[17] M. Amin, Z. Liang, and A. Lindsey, "Performance analysis of subspace projection techniques for anti-jamming gps using spatio-temporal interference signatures," in *Proceedings of the 11th IEEE Signal Processing Workshop on Statistical Signal Processing (Cat. No.01TH8563)*, 2001, pp. 361–364.

[18] L. Zhao, M. G. Amin, A. Lindsey, and Y. Zhang, "Subspace array processing for the suppression of fm jamming in gps receivers," in *Conference Record of the Thirty-Fourth Asilomar Conference on Signals, Systems and Computers (Cat. No.00CH37154)*, vol. 2, Oct 2000, pp. 1000–1004 vol.2.

[19] Z. Liang and A. Amin, Mo. G.and Lindsey, "Subspace projection techniques for anti-fm jamming gps receivers," in *Proceedings of the Tenth IEEE Workshop on Statistical Signal and Array Processing (Cat. No.00TH8496)*, 2000, pp. 529–533.

[20] S. Daneshmand, A. Broumandan, J. Nielsen, and G. Lachapelle, "Interference and multipath mitigation utilising a two-stage beamformer for global navigation satellite systems applications," *IET Radar, Sonar Navigation*, vol. 7, no. 1, pp. 55–66, Jan 2013.

[21] G. Seco-Granados, J. A. Fernandez-Rubio, and C. Fernandez-Prades, "Ml estimator and hybrid beamformer for multipath and interference mitigation in gnss receivers," *IEEE Transactions on Signal Processing*, vol. 53, no. 3, pp. 1194–1208, March 2005.

[22] F. Antreich, F. Wendler, A. Iliopoulos, M. Appel, M. Sgammini, S. Caizzone, A. Konovaltsev, F. Trötschel, M. Marinho, and M. Cuntz, "Robust multi-antenna gnss receiver for maritime applications," 09 2015.

[23] J. Vila-Valls, P. Closas, C. Fernandez-Prades, and J. T. Curran, "On the ionospheric scintillation mitigation in advanced gnss receivers," *IEEE Transactions on Aerospace and Electronic Systems*, pp. 1–1, 2018.

[24] J. Vila-Valls, P. Closas, and J. T. Curran, "Performance analysis of multi-frequency gnss carrier tracking for strong ionospheric scintillation mitigation," in *2017 25th European Signal Processing Conference (EUSIPCO)*, Aug 2017, pp. 2699–2703.

[25] G. Sivavaraprasad, R. S. Padmaja, and D. V. Ratnam, "Mitigation of ionospheric scintillation effects on gnss signals using variational mode decomposition," *IEEE Geoscience and Remote Sensing Letters*, vol. 14, no. 3, pp. 389–393, March 2017.

[26] F. Ghafoori and S. Skone, "Impact of equatorial ionospheric irregularities on gnss receivers using real and synthetic scintillation signals," *Radio Science*, vol. 50, no. 4, pp. 294–317, April 2015.

[27] V. Sreeja, M. Aquino, and Z. G. Elmas, "Impact of ionospheric scintillation on gnss receiver tracking performance over latin america: Introducing the concept of tracking jitter variance maps," *Space Weather*, vol. 9, no. 10, pp. 1–6, Oct 2011.

[28] N. Antonietti, L. C. Feletti, and G. Pagana, "The picpot project: Gps and galileo in high dynamic scenario," in *2005 2nd International Symposium on Wireless Communication Systems*, Sep. 2005, pp. 847–851.

[29] C. Alcaide-Guillén, A. Vidal-Pantaleoni, and J. Martín-Romero, "A proof of concept study for a fast acquisition in a leo satellite gps receiver," *Navigation*, vol. 65, no. 2, pp. 231–246, 2018. [Online]. Available: https://onlinelibrary.wiley.com/doi/abs/10.1002/navi.224

[30] V. Calmettes, A. A.Dion, E. Boutillion, and E. Liegeon, "Fast acquisition unit for gps/galileo receivers in space environment," in *Proceedings of the 2008 National Technical Meeting of The Institute of Navigation*, San Diego (CA), 2008, pp. 288–297.

[31] M. Powe, F. Zanier, M. Porretta, A. Garcia-Rodriguez, and O. Mongrard, "Analysis of the international space station multipath and masking environment for automated transfer vehicle relative gps rendezvous manoeuvres," in *2012 6th ESA Workshop on Satellite Navigation Technologies (Navitec 2012) European Workshop on GNSS Signals and Signal Processing*, Dec 2012, pp. 1–7.

[32] B. Parkinson and J. Spilker, *Global Positioning System: Theory and Applications, vol. I, II.* vol. 163-164 of , Washington DC: Progress in Astronautics and Aeronautics, American Institute of Aeronautics, Inc., 1996.

[33] Fernández-Prades, J. C., Arribas, and P. Closas, "Turning a television into a gnss receiver," in *Proceedings of the 26th International Technical Meeting of The Satellite Division of the Institute of Navigation (ION GNSS 2013)*, Sep 2013, pp. 1492–1507.

[34] GMV, "srx-10 dataheet," https://www.gmv.com/export/sites/gmv/DocumentosPDF/srx-10/srx-10_brochure_2013.pdf, Last accessed on 2018-7-4.

[35] Deimos, "Granada dataheet," http://www.elecnor-deimos.com/wp-content/uploads/2017/09/G3_EN.pdf, Last accessed on 2018-7-4.

[36] L. Musumeci, F. Dovis, J. S. Silva, P. F. da Silva, and H. D. Lopes, "Design of a high sensitivity gnss receiver for lunar missions," *Advances in Space Research*, vol. 57, no. 11, pp. 2285 – 2313, 2016. [Online]. Available: http://www.sciencedirect.com/science/article/pii/S027311771630045X

[37] P. J. Mumford, K. Parkinson, and A. Dempster, "The namuru open gnss research receiver," in *Proceedings of the ION ITM*, 2006, pp. 2847–2855.

[38] P. J. Mumford and Y. Heo, ""namuru-gpl", open source software for the namuru fpga-based gnss receiver," in *International Global Navigation Satellite Systems Society IGNSS Symposium 2007*, 2007.

[39] DLR, "Phoenix datasheet."

[40] O. Montenbruck, B. Nortier, and S. Moster, "A miniature gps receiver for precise orbit determination of the sunsat 2004 micro-satellite," in *Proceedings of the 2004 International Technical Meeting of The Institute of Navigation*, Jan 2004.

[41] F. Principe, G. Bacci, F. Giannetti, and M. Luise, "Software-defined radio technologies for gnss receivers: A tutorial approach to a simple design and implementation," *International Journal of Navigation and Observation*, vol. 27, 05 2011.

[42] C. Fernández-Prades, J. Arribas, P. Closas, C. Aviles, and L. Esteve, "Gnss-sdr: An open source tool for researchers and developers," in *Proceedings of the 24th International Technical Meeting of The Satellite Division of the Institute of Navigation (ION GNSS 2011)*, Sep 2011, pp. 780–794.

[43] A. Schmid, "Enhanced sensitivity for galileo and gps receivers," Ph.D. dissertation, Technischen Universitat MÃ$\frac{1}{4}$nchen, January 2007.

[44] D. Borio, "A statistical theory for gnss signal acquisition," Ph.D. dissertation, Politecnico de Torino, 2008.

[45] D. Borio and L. Lo Presti, "Data and pilot combining for composite gnss signal acquisition," *International Journal of Navigation and Observation*, vol. 2008, 04 2008.

[46] M. Tamazin, M. Karaim, and A. Noureldin, *GNSSs, Signals, and Receivers*, 05 2018.

[47] P. M. Kintner, B. M. Ledvina, and E. de Paula, "Gps and ionospheric scintillations," *Space Weather*, vol. 5, 09 2007.

[48] iac, "Information and analysis center for positioning , navigation and timing," https://glonass-iac.ru/en/guide/index.php, Last accessed on 2019-21-5.

[49] E. D. Kaplan, *Understanding GPS: Principles and Applications.* Norwood MA 02062: Artech House Publishers, 1996.

[50] M. Foucras, J. Leclère, C. Botteron, O. Julien, C. Macabiau, P.-A. Farine, and B. Ekambi, "Study on the cross-correlation of gnss signals and typical approximations," *GPS Solutions*, vol. 21, pp. 293–306, 04 2017.

[51] J. Leclère, R. Landry Jr, and C. Botteron, "Comparison of l1 and l5 bands gnss signals acquisition," vol. 18, p. 2779, 08 2018.

[52] J. Arribas, "Gnss array-based acquisition: Theory and implementation," Ph.D. dissertation, Universtitat Politecnica de Catalunya, May 2012.

[53] C. Lee, Y.-H. Chen, G. Wong, S. lo, and P. Enge, "Multipath benefits of boc vs. bpsk modulated signals using on-air measurements," pp. 742–751, 01 2013.

[54] J. W. T. J. W. Cooley, "An algorithm for the machine computation of complex fourier series," *Mathematics of Computation*, vol. 19, pp. 297–301, April 1965.

[55] Navstar, "Is-gps-200," April 2018.

[56] ——, "Is-gps-05," April 2018.

[57] J. Ángel Ávila Rodríguez, "On generalized signal waveforms for satellite navigation," Ph.D. dissertation, UAF MÃ$\frac{1}{4}$nchen, June 2008.

[58] ESA, "Galileo os sis icd, issue 1.3," December 2016.

[59] W. D. W. J-M. Sleewaegen, "Galileo altboc receiver," in *ENC-GNSS*, May 2004, pp. 1–9.

[60] H. K. W. Stansell T. A. and K. R. G., "Future wave: L1c signal performance and receiver design," *GPS World*, vol. 4, pp. 46–47, April 2011.

[61] S. F. Ahamed, G. Laveti, R. Goswami, and G. S. Rao, "Fast acquisition of gps signal using radix-2 and radix-4 fft algorithms," in *2016 IEEE 6th International Conference on Advanced Computing (IACC)*, Feb 2016, pp. 674–678.

[62] D. J. R. Van Nee and A. J. R. M. Coenen, "New fast gps code-acquisition technique using fft," *Electronics Letters*, vol. 27, no. 2, pp. 158–160, Jan 1991.

[63] M. Tahir and L. L. Presti, "Performance analysis of pre-correlation differential acquisition scheme," in *2012 6th ESA Workshop on Satellite Navigation Technologies (Navitec 2012) European Workshop on GNSS Signals and Signal Processing*, Dec 2012, pp. 1–8.

[64] D. Akopian, "Fast fft based gps satellite acquisition methods," *IEE Proceedings on Radar,Sonar & Navigation*, vol. 152, no. 4, pp. 277–286, 2005.

[65] H. Li, X. Cui, M. Lu, and Z. Feng, "Dual-folding based rapid search method for long pn-code acquisition," *IEEE Transactions on Wireless Communications*, vol. 7, no. 12, pp. 5286–5296, December 2008.

[66] S. Kong, "A deterministic compressed gnss acquisition technique," *IEEE Transactions on Vehicular Technology*, vol. 62, no. 2, pp. 511–521, Feb 2013.

[67] A. Dion, E. Boutillon, V. Calmettes, and E. Liegon, "A flexible implementation of a global navigation satellite system (gnss) receiver for on-board satellite navigation," 10 2010, pp. 48–53.

[68] P. Gaggero and D. Borio, "Ultra-stable oscillators: Limits of gnss coherent integration," 01 2008.

[69] A. Hauschild, M. Markgraf, and O. Montenbruck, "Gps receiver performance on board a leo satellite," *Inside GNSS*, pp. 48–57, 2014.

[70] P. Esteves, "Techniques d'acquisition á haute sensibilité des signaux gnss," Ph.D. dissertation, Institut Supérieur de l'Aéronautique et de l'Espace (ISAE), May 2014.

[71] B. Zolesi and L. R. Cander, *Ionospheric Prediction and Forecasting.* Berlin: Springer Geophysics, Springer-Verlag, 2014.

[72] P. Esteves and M. Boucheret, "Sensitivity characterization of differential detectors for acquisition of weak signals," *IEEE Transactions on Aerospace and Electronic Systems*, vol. 12, no. 1, pp. 20–37, 2016.

[73] V. Capuano, C. Botteron, J. Leclère, J. Tian, Y. Wang, and P.-A. Farine, "Feasibility study of gnss as navigation system to reach the moon," *Acta Astronautica*, vol. 116, pp. 186 – 201, 2015. [Online]. Available: http://www.sciencedirect.com/science/article/pii/S0094576515002520

[74] A. Birklykke, "High dynamic gps signal acquisition," Master's thesis, Department of Electronic Systems,Aalborg University, 2010.

[75] D. Borio, C. Gernot, and G. Macchi, F.and Lachapelle, "The output snr and its role in quantifying gnss signal performance," in *Proceedings of ENC, Toulouse,France*, 2008.

[76] R. D. Hippenstiel, *Detection Theory: Applications and Digital Signal Processing.* CRC Press LLC, 2002.

[77] P. Tang, S. Wang, X. Li, and Z. Jiang, "A low-complexity algorithm for fast acquisition of weak dsss signal in high dynamic environment," *GPS Solutions*, vol. 21, 04 2017.

[78] D. Borio, C. O'Driscoll, and G. Lachapelle, "Coherent, noncoherent, and differentially coherent combining techniques for acquisition of new composite gnss signals," *IEEE Transactions on Aerospace and Electronic Systems*, vol. 45, no. 3, pp. 1227–1240, July 2009.

[79] D. A. Shnidman, "The calculation of the probability of detection and the generalized marcum q-function," *IEEE Transactions on Information Theory*, vol. 35, no. 2, pp. 389–400, March 1989.

[80] M. L. Psiaki, "Block acquisition of weak gps signals in a software receiver," in *Proceedings of the 14th International Technical Meeting of the Satellite Division of The Institute of Navigation (ION GNSS 2001)*, Sep 2001, pp. 2838–2870.

[81] C. Strassle, D. Megnet, H. Mathis, and C. Burgi, "The squaring-loss paradox," in *In Proceedings of the 20th International Technical Meeting of the Satellite Division of The Institute of Navigation (ION GNSS 2007)*, Sept 2007, pp. 2715–2722.

[82] M. L Psiaki, "Fft-based acquisition of gps l2 civilian cm and cl signals," in *Proceedings of the 17th International Technical Meeting of the Satellite Division of The Institute of Navigation (ION GNSS 2004)*, Sep 2004, pp. 646–653.

[83] M. Baracchi-Frei, "Real-time gnss software receiver optimized for genera purpose microprocessors," Ph.D. dissertation, Institute of Microtechnology (IMT) University of Neuchatel, July 2010.

[84] D. Akopian, "A fast satellite acquisition method," in *Proceedings of the 14th International Technical Meeting of the Satellite Division of the Institute of Navigation ION GPS 2001*, Sep 2001, pp. 2871–2881.

[85] N. F. Krasner, "Gps receiver and method for processing gps signals," Patent, 7 1998, patent No. 5,781,156.

[86] USRP, "Usrp dataheet," https://www.ettus.com/content/files/X300_X310_Spec_Sheet.pdf, Last accessed on 2019-4-1.

[87] A. Hennigar, "Analysis of record and playback errors of gps signals caused by the usrp," Master's thesis, Auburn University, December 2014.

[88] D. Borio, F. Dovis, H. Kuusniemi, and L. L. Presti, "Impact and detection of gnss jammers on consumer grade satellite navigation receivers," *Proceedings of the IEEE*, vol. 104, no. 6, pp. 1233–1245, June 2016.

[89] G. Lachapelle and A. Broumandan, "Benefits of gnss if data recording," 05 2016, pp. 1–6.

[90] S. U. Qaisar, N. Cs, and A. Dempster, "Exploiting the spectrum envelope for gps l2c signal acquisition," *GPS World*, March 2008.

[91] S. Turunen, "Weak signal acquisition in satellite positioning," Ph.D. dissertation, Tampere University of Technology, 2010.

[92] F. Macchi, "Development and testing of an l1 combined gps-galileo software receiver," Ph.D. dissertation, University of Calgary, 2010.

[93] D. Borio and D. Akos, "Noncoherent integrations for gnss detection: Analysis and comparisons," *IEEE Transactions on Aerospace and Electronic Systems*, vol. 45, no. 1, pp. 360–375, 2009.

[94] J. Holmes and C. Chen, "Acquisition time performance of pn spread spectrum systems," *IEEE Transactions on Communications*, vol. 25, no. 8, pp. 778–784, 1977.

[95] S. K. Shanmugam, R. Watson, J. Nielsen, and G. Lachapelle, "Differential signal processing schemes for enhanced gps acquisition," in *Proceedings of the 18th International Technical Meeting of the Satellite Division of The Institute of Navigation (ION GNSS 2005)*, Sep 2005, pp. 212–222.

[96] S. K. Shanmugam, "Improving gps l1 c/a code correlation properties using a novel multi-correlator differential detector technique," in *Proceedings of the 19th International Technical Meeting of the Satellite Division of The Institute of Navigation (ION GNSS 2006)*, Sep 2005, pp. 2453–2464.

[97] H. Hui, Y. Yuan, H. W., and G. Minghua, "Gps receiver c/a code rapid acquisition technology," *Research Dan Zou School of Information Engineering,East China Jiaotong University*, pp. 477–484, 2013.

[98] D.-S. Shim and J.-S. Jeon, "An unambiguous delay-and-multiply acquisition scheme for gps l1c signals," *Sensors*, vol. 18, p. 1739, 05 2018.

[99] D. V. Sarwate and M. B. Pursley, "Crosscorrelation properties of pseudorandom and related sequences," *Proceedings of the IEEE*, vol. 68, no. 12, pp. 593–619, 1980.

[100] R. Gold, "Optimal binary sequences for spread spectrum multiplexing," *IEEE Transactions on Information Theory*, vol. 13, no. 4, pp. 619–621, 1967.

[101] C. C. Fan and T. Z., "A differentially coherent delay-locked loop for spread-spectrum tracking receivers," *IEEE Communications Letters*, vol. 3, no. 10, pp. 282–284, 1999.

[102] K. Borre and e. a. Akos, D. M., *A Software-Defined GPS and Galileo Receiver: A Single-Frequency Approach*. Basel, Switzerland: Ed Birkhauser, 2007.

[103] D. Zhongliang, X. Yue, J. Jichao, and Lu, "Unambigous acquisition for galileo e1 os signal based on delay and multiply," *TELKOMNIKA*, vol. 12, no. 4, pp. 950–962, 2014.

[104] C. C. Craig, "On the frequency function of xy," *Annals of Mathematical Society*, vol. 4, pp. 46–47, 1936.

[105] Weisstein, Eric W., "Erfc," http://mathworld.wolfram.com/Erfc.html, Last accessed on 2019-22-4.

[106] J. Proakis and D. G. Manolakis, *Digital Signal Processing: Principles, Algorithms, and Applications*. Prentice Hall, 1996.